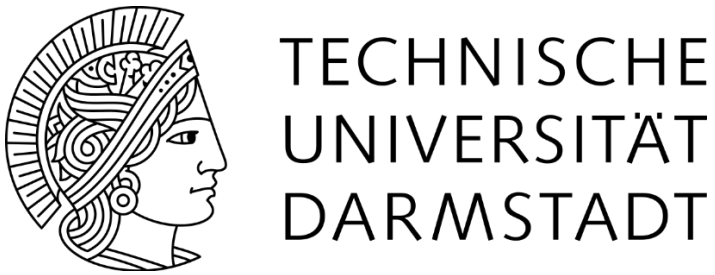

Politecnico di Torino

Corso di Laurea Magistrale in Ingegneria Aerospaziale, percorso Aerostrutture
A.a. 2020-2021
Sessione di Laurea Luglio 2021

Modeling and simulation of lightweight lattice structures for impact energy absorption

Relatore:
Prof. Giorgio De Pasquale

Candidato:
Antonio Coluccia

Tutor presso TU Darmstadt:
Prof. Christian Mittelstedt

Co-tutor presso TU Darmstadt:
Research Assistant Guillaume Meyer

I miei ringraziamenti vanno
a mio padre Marcello, mia madre Raffaella e mia nonna Lucia
a Claudia
e a tutti i miei amici
per avermi dato forza e aiutato, da lontano e da vicino,
in questo buio periodo di pandemia.

It has to be acknowledged that research activities necessary for the writing of this thesis have been conducted at Konstruktiver Leichtbau und Bauweisen Institute, Technische Universität Darmstadt.

Abstract

Metal lattice structures possess a wide range of applications in the mechanical field, mainly because of their high functionality and their lightweight. Additive Manufacturing (AM) offers an incredible design freedom for topologically complex components, that before the advent of this technology were manufactured with many difficulties and expenses: world of lattices made a huge step forward thanks to AM, and still today research in this subfield of mechanics is extremely active. Different engineering disciplines employ lattices for designing components, using latest technologies. One of the most important application nowadays for these materials, especially when it comes to aerospace, biomedical and automotive sectors, is as energy absorbers: this thesis wants to be a contribution in this direction. In particular, the main aim is to establish design guidelines for truss-based lattice, when contributions of load directed reinforcements and cells combination are present; multi-morphology design will be considered as well.

A specific set of lattice cells, selected among the most promising ones for energy absorption, has been tested using FEA (Ansys). As a starting point for investigations, static simulations have been performed using a bilinear model for the material used (that is AlSi10Mg, one of the most used both for its lightweight and for the fact that is easily processable using AM). Bilinear model is ideal in this case because it allows with very good approximation the study of the plastic domain of the material. Most of the energy absorption characteristics of lattices lies in fact in their plastic filed and it ends with densification; simulations are performed taking account of this. Results from static simulations are therefore used for a confrontation with results from high speed impact simulations, whose model is basically inspired by classical crashworthiness and impact tests. These simulations, performed using the Ansys explicit solver, offer answers about densification and its effects (impossible to catch with static simulations) and energy parameters needed to rank and to analyze the selected lattices. One of the main objectives of these analyses, beside just mentioned results, is to check if static analyses are able to predict dynamic response.

When it comes to analyses of large samples or components, modeling methods contemplating generation of the whole lattice geometry can present extremely long solving process times. For sake of time but also for sake of the nature of the simulations themselves (that should allow time and money saving), a homogenization process has been used in order to make multi-morphology analyses more affordable: one single cell can be in fact modeled as one, or more, element. The developed method allows the creation of a medium material that brings with him information about the lattice elastoplastic behavior, because, as said, the plastic domain makes the difference in this situation. Moreover, errors and deviations from the original models have been evaluated, in order to be aware of the method limits. Therefore, samples presenting configurations inspired by classical Reuss, Voigt and lamination theories are generated and tested under high speed crashing conditions using explicit solver. These simulations offer results about how mixing lattices with specific rules can improve energy absorption.

All of the results obtained are therefore used to establish construction guidelines and a methodology for lattice simulations that can be valid for energy absorption analysis.

Contents

1 Introduction

"When modern man builds large load-bearing structures he uses dense solids: steel, concrete, glass. When nature does the same, she generally uses cellular materials: wood, bone, coral. There must be good reasons for it".

M.F Ashby, The Mechanical Properties of Cellular Solids

The history of cellular solids looks back into the origins of structures: natural materials have always been used for structural aims; first, wood still is among the most employed materials and of course it can be seen both as a cellular solid and a natural composite material. At least 5000 years old wooden artefacts have been discovered in pyramids of Ancient Egypt (citing [1]); also, cork was used to seal wine bottles in Roman times (Horace, 27 BC). Further section of this chapter will deal with natural cellular solids and materials inspired by them as well, according to modern literature. Later, a deepening on the world of lattices, that are the main argument of this investigation as well (as a cellular solid class) will be provided.

1.1 Cellular solids

Basis of the cellular solids theory can be found in the works of M.F. Ashby and L.J. Gibson, [1] and [2] have been extremely useful in order to understand the most general characteristics of these materials, as well for the definition of the analysis methodology. This subchapter also presents a series of research and projects inspired by natural cellular solids: in this direction, [3] has been the most interesting review among contemporary literature.

The name itself, cellular solid, is already quite explanatory: 'cell' comes from the Latin *cella* that stands for a room defined by specified limits; when it comes to arrangements of cells, the topic is about *cellarium* or, in the modern language, cellular solids. These materials, as said, already exist in nature, but man-made cellular solids have been generated as well. Nowadays the definition has changed, in facts they are defined as "a made up of an interconnected network of solid struts or plates which form the edges and faces of cells" (from [1]), and they can be divided by four classes: honeycombs, open-cell foams, closed-cell foams and lattice structures. Being this investigation more interested in lattices, this particular class will be deepened later. Figure 1 shows typical cellular solids structures.

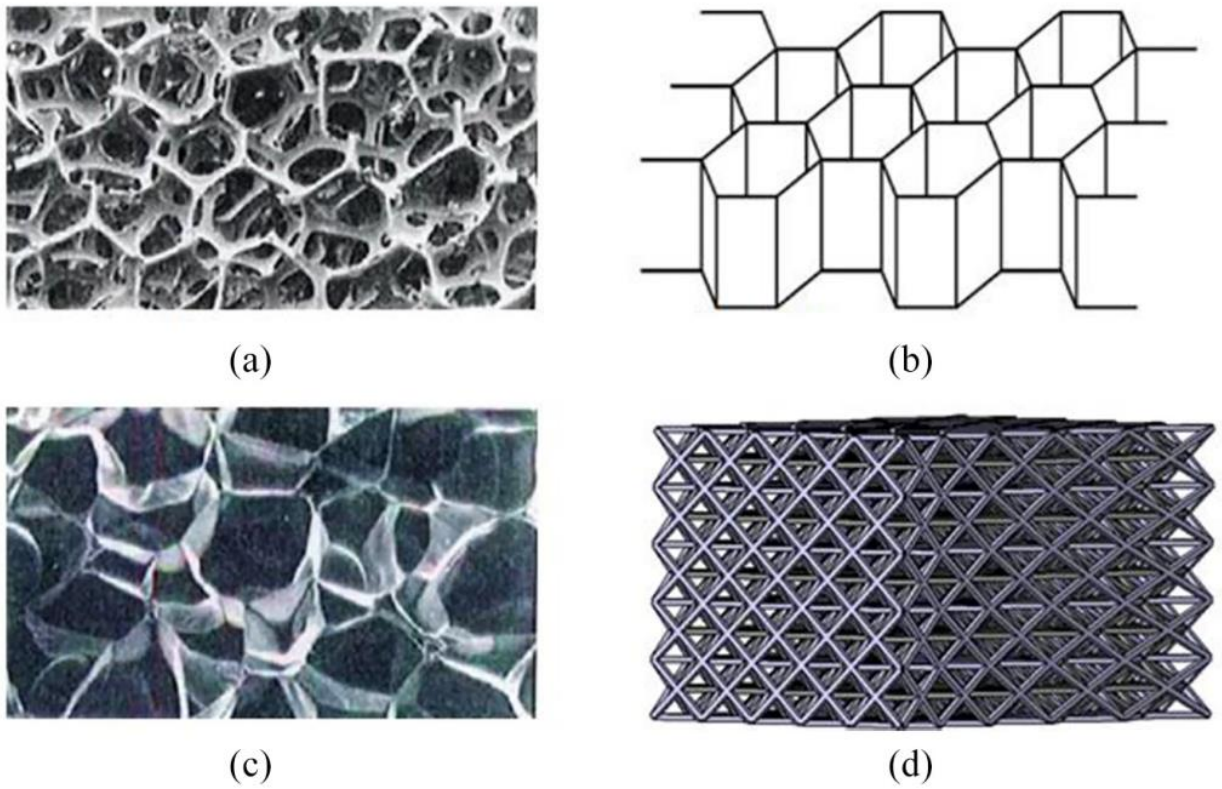

Figure 1: cellular solids classes examples including (a) open-cell foam, (b) honeycomb, (c) closed-cell foam and (d) lattice (from [4], actually adapted from [1]).

1.1.1 Bio-inspired topologies

While relative density is important because the control of this property is related with the control of porosity and therefore strictly linked with mechanical properties such as strength and stiffness, another important feature of cellular solids is topology of the cell: most topologies have been inspired by nature and showed excellent results. As a demonstration and enforcement of the quote that opens this chapter, a series of bio-inspired cellular structures that show good properties (energy absorption) is presented next.

First, a general classification is shown in figure 2, showing the large number of possibilities available. The concept of honeycombs can be extended to different shapes, besides the conventional one: new geometries resembling natural structures have been studied. In [5], horseshoe mesostructures have been applied to conventional honeycomb patterns, showing excellent results from the point of view of specific energy absorption and plateau stress rising (the importance of these properties will be later explained in chapter 4). Figure 3 shows the process used for the transformation of conventional honeycombs into horseshoe ones.

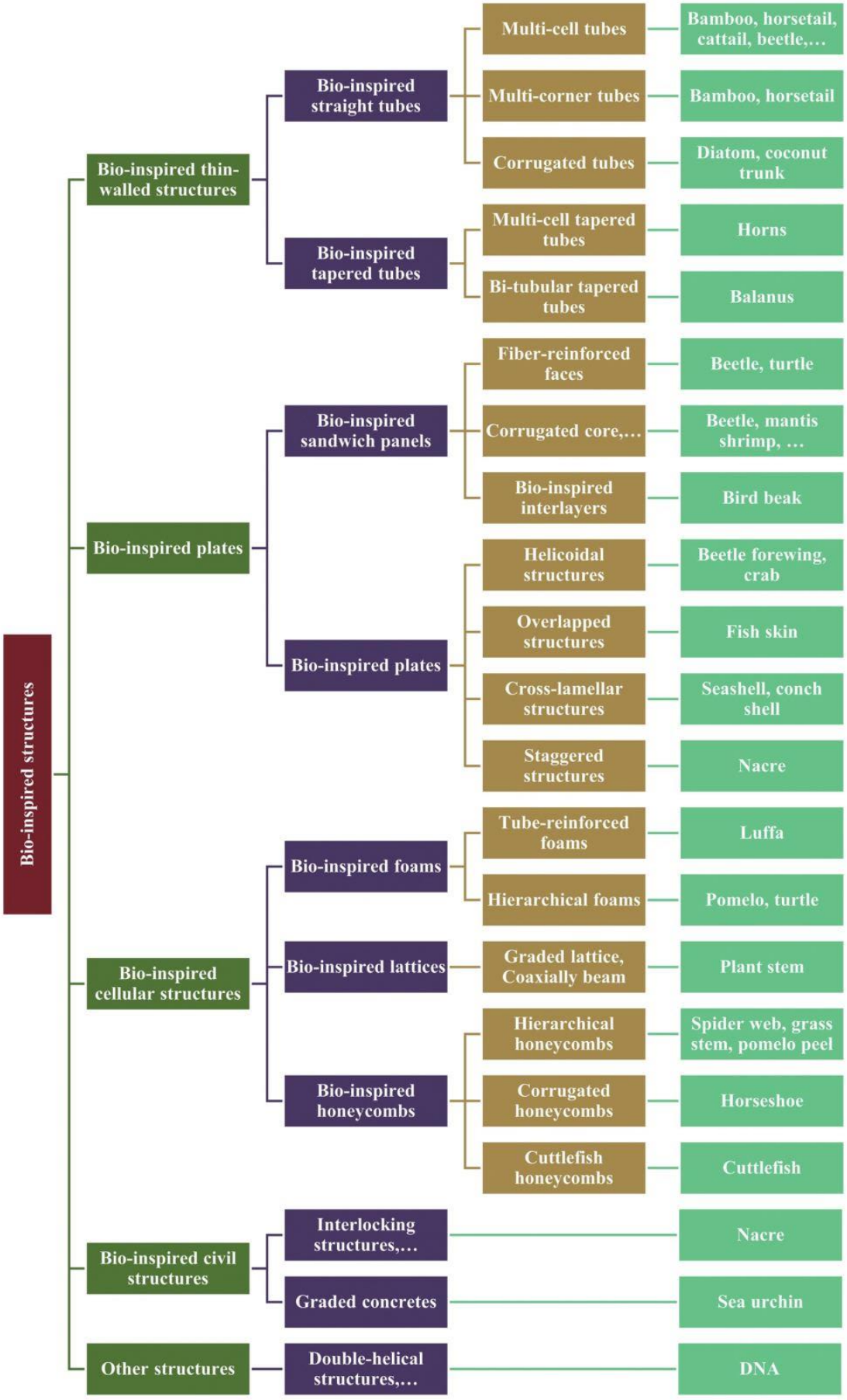

Figure 2: general classification of bio-inspired structures according to [3].

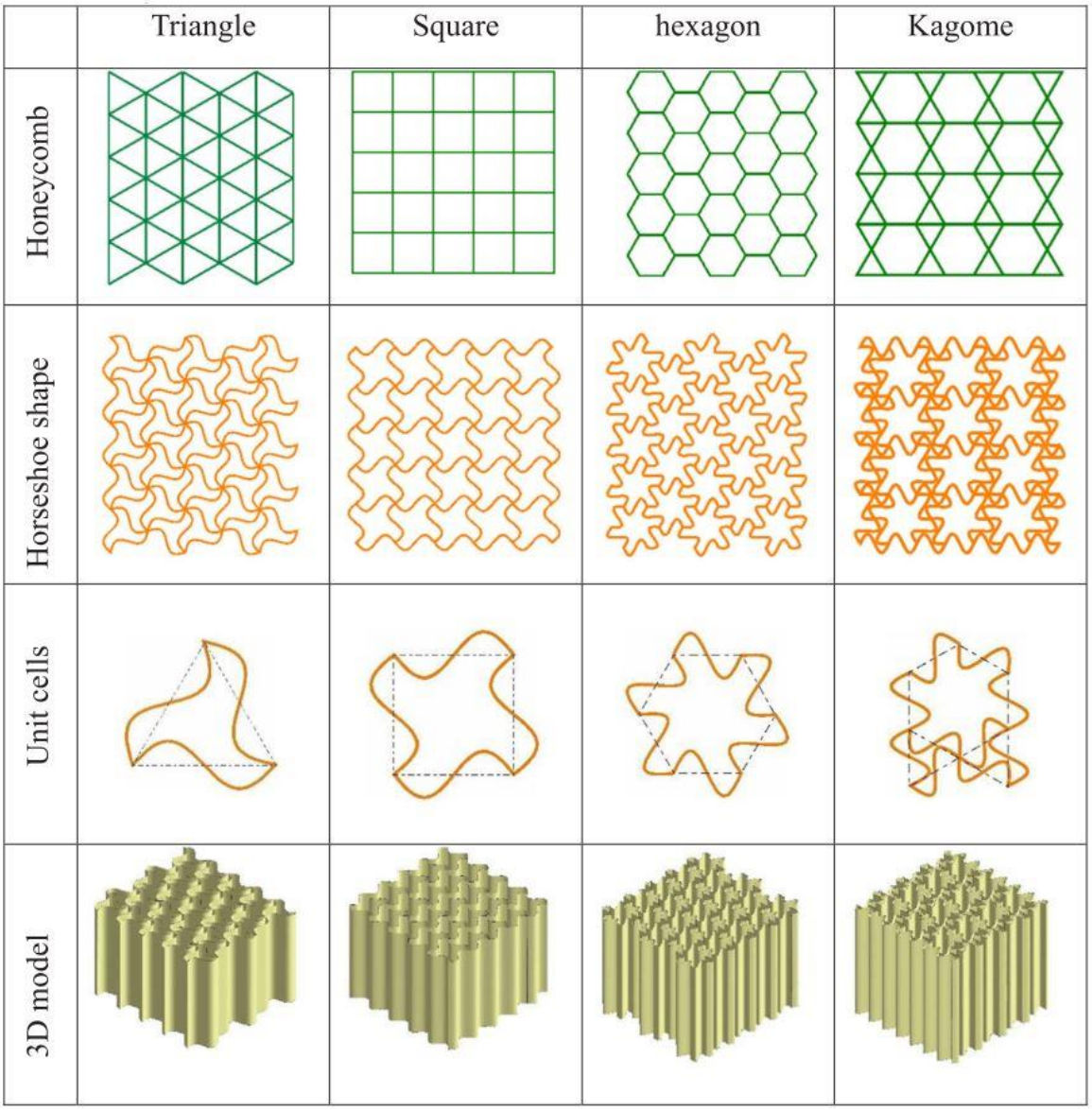

Figure 3: horseshoe honeycombs with original patterns from which they have been generated (from [5]).

Another interesting design can be found in [6], where a hierarchical honeycomb design mimicking grass stems is proposed (figure 4). Second level of hierarchy has been reached in the reference proposed, but further levels have been reached in other studies. Results are once more surprisingly good: first order hierarchy presents 81,3% improvement on specific energy absorption, while second order achieved 185,7% improvement on the same property. An alternative interesting project is presented in [7], where again hierarchical honeycombs are studied, but this time the structure is related to spider-webs (figure 5): results achieved show a rise in SEA with respect to conventional honeycombs.

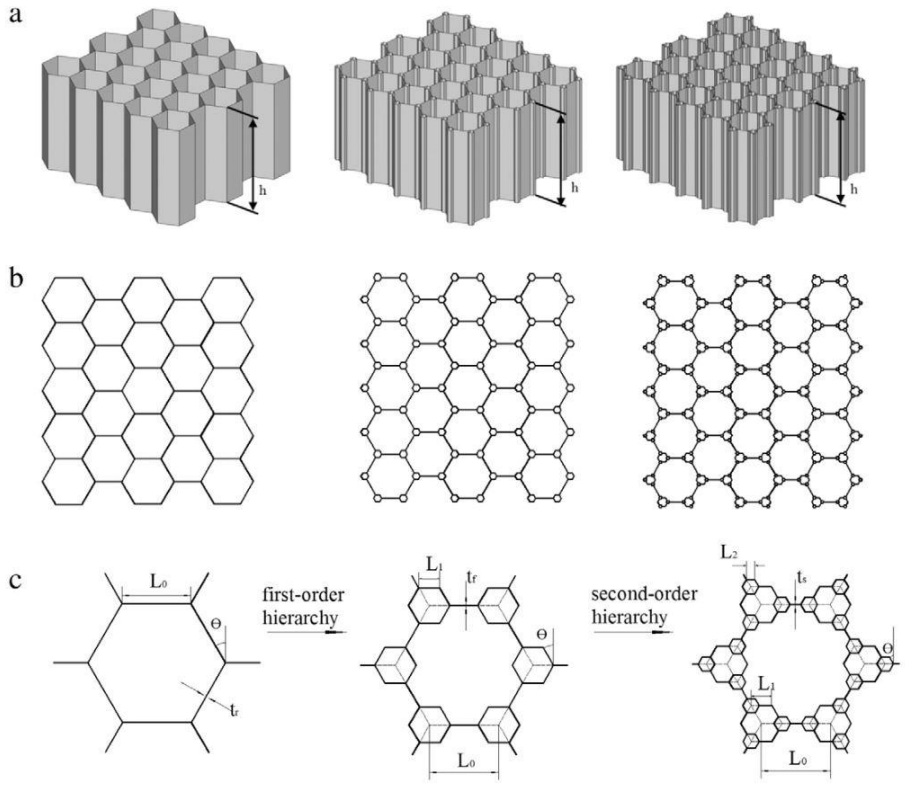

Figure 4: conventional, first order and second order hierarchy grass stem inspired honeycombs in (a) 3D view, (b) top view and (c) single unit cell (from [6]).

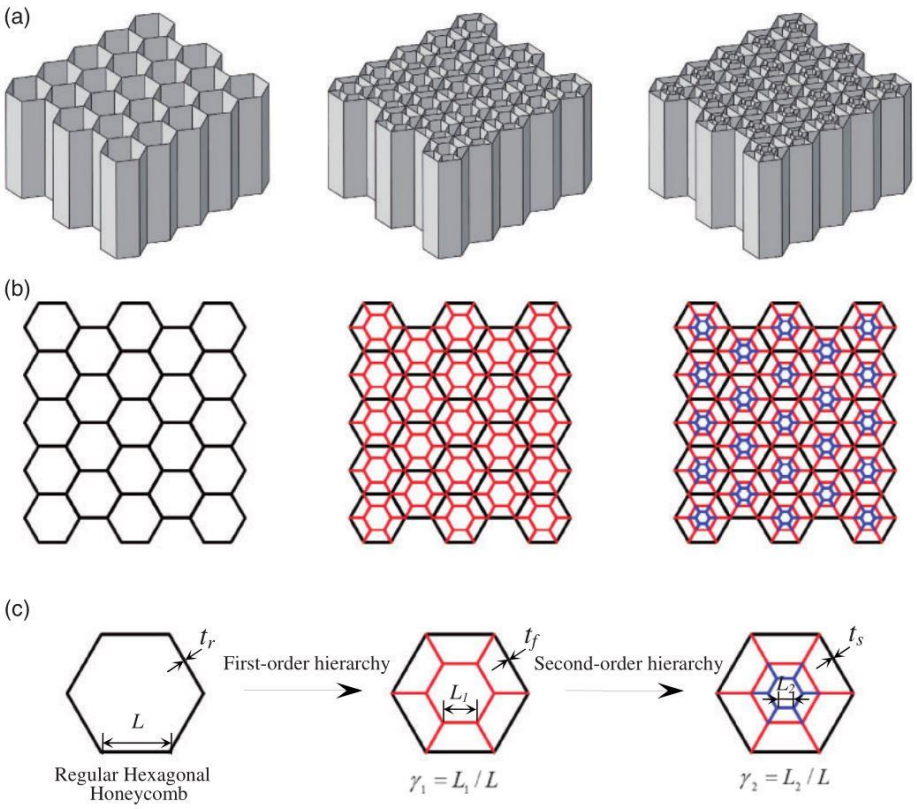

Figure 5: conventional, first order and second order hierarchy spider-web inspired honeycombs in (a) 3D view, (b) top view and (c) single unit cell (from [7]).

One last design about honeycombs is shown in [8], where a hierarchical structure based on pomelo fruit peel is generated (figure 6). Once again excellent results from the point of view of specific energy absorption are obtained, surpassing the ones achieved from classical honeycomb.

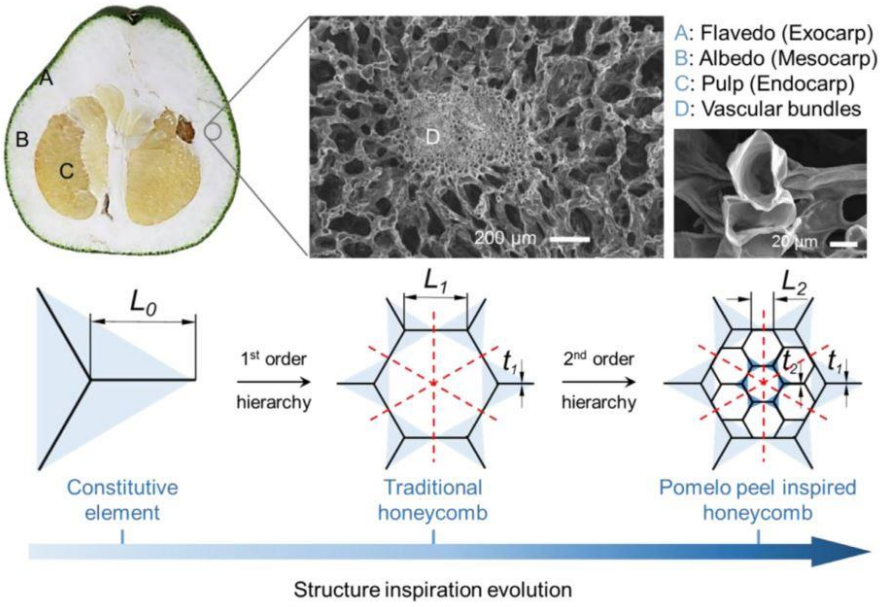

Figure 6: SEM photographs showing microstructures of pomelo peel, together with configurations of pomelo peel inspired hierarchical honeycomb.

Apart from honeycombs, another cellular solid class which is influenced from bio-inspired structures is the one of the foams. [9] presents a design for a hierarchical aluminum foam inspired by luffa sponge structure that can be seen in figure 7.

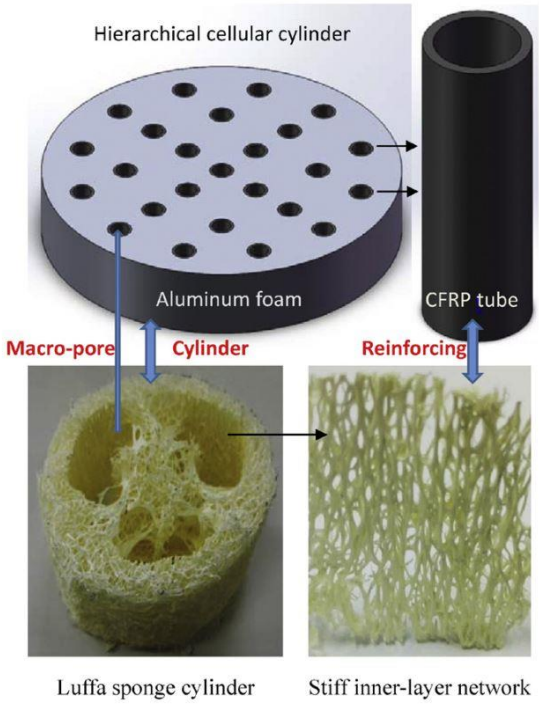

Figure 7: hierarchical luffa-sponge-like aluminum foam (from [9]).

Core and shell of the sponge are linked with the aluminum foam, while the macro-pores and the reinforced layer around them are modeled with CFRP tubes. Effects of stiff inner layers network, interaction of composites with foam and hierarchy shows an efficient improvement from the point of view of specific energy absorption with regards to classical aluminum foams. Another interesting project can be found in [10], where lotus root inspired ingots have been tested to crashing in the perpendicular-to-section direction, showing interesting results (see figure 8).

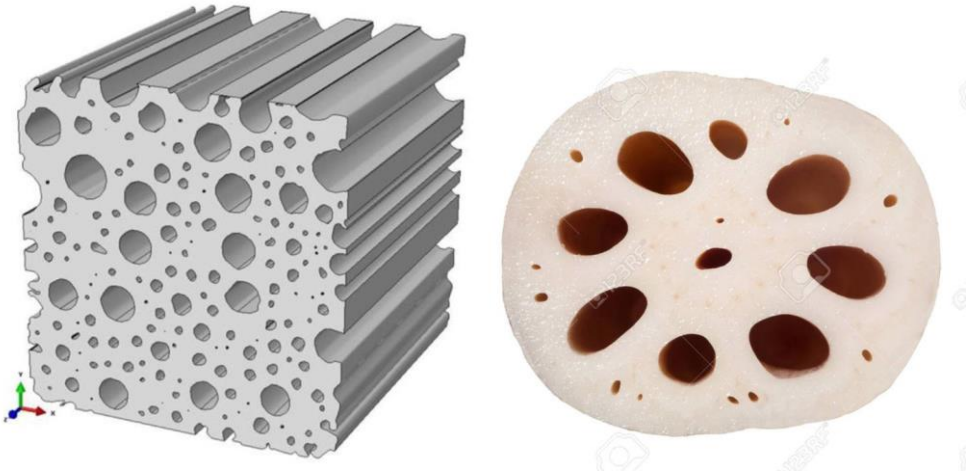

Figure 8: lotus-type ingot (from [10]) and lotus root section.

These are only few examples of the many ways nature can influence foams structures. Also, lattices are extremely propense toward mimicking natural structures. One example can be found in [11], where three nature-inspired lattices have been generated: cellulose lattice is inspired by plant cells arrangements (figure 9), while tetrahedron and pyramid unit cells are related with the stochastic pattern of trabeculae, that is the part of the bone associated with strength and energy absorption (figure 10). Grading effects are as well part of this investigation.

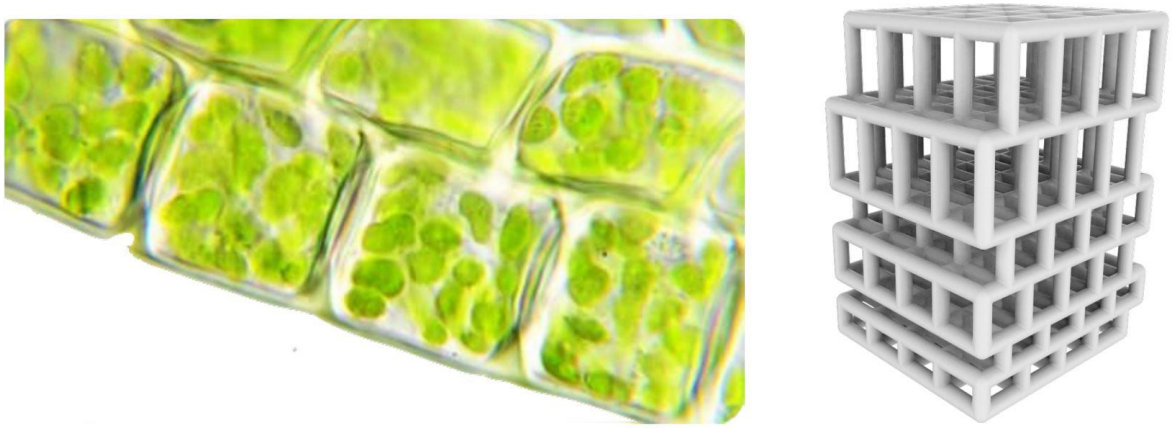

Figure 9: plant cells arrangements (left) and graded cellulose lattice structure (right) (from [11]).

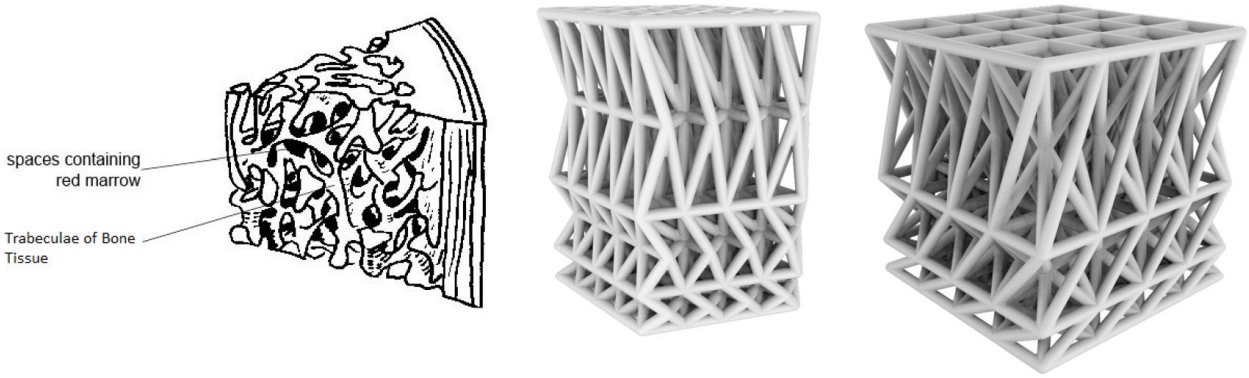

Figure 10: trabeculae (left), graded tetrahedron lattice structure (middle) and graded pyramid lattice structure (right) (from [11]).

Another exemplar design is presented in [12], where a structure inspired by the armor of the glyptodont (*Glyptotherium Arizonae*), that is an extinct mammal related to the armadillo family that lived during the Late Pleistocene period, has been developed and it is shown in figure 11. Body armor of this extinct mammal was structured as an interlocking network of osteoderms, on which the model presented, that is formed by a plate shell and a lattice core, is based. Results obtained highlight the good energy absorption capacity and high strength of such structures.

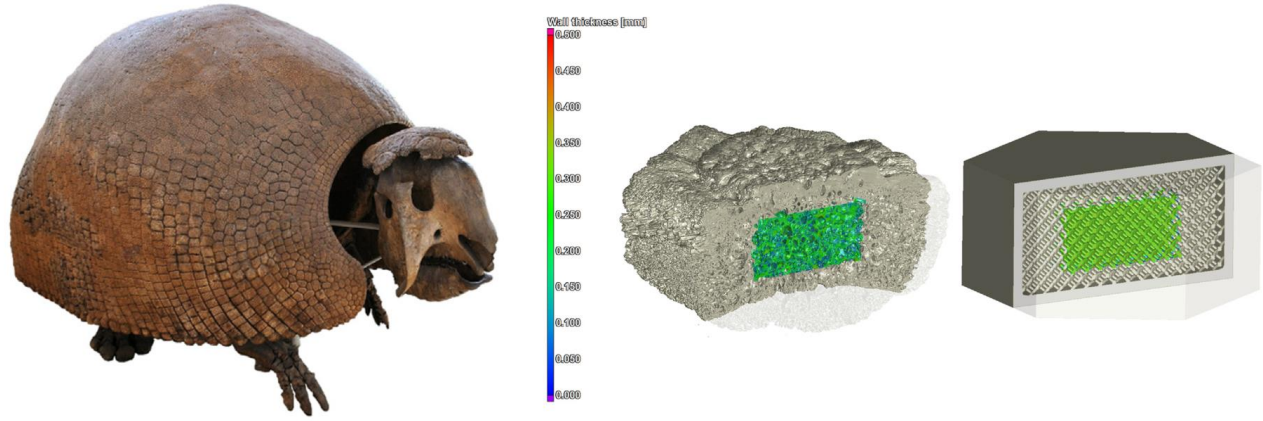

Figure 11: Reconstruction of a glyptodont fossil where it is possible to notice the body armor consisting of interlocking osteoderms (left) and a single osteoderm next to the model inspired by it (right) (from [12]).

Between being a lattice and a reticulated shell, [13] shows an interesting design inspired by the diving bell of the water spider, that can be seen in figure 12. This investigation uses the strut diameter as a parameter for studying its effects on energy absorption. One last example shown here is present in [14], where auxetic lattices generated following the crystal structures of α-cristobalite and $LaNiO_3/SrTiO_3$ have been tested for energy absorption purposes: materials were manufactured via a wire-woven structure and then filled with another solid, creating a sort of hybrid truss-shell lattice. Excellent results have been achieved from the point of view of energy absorption, ultrahigh strength and ductility. Such lattices are shown in figure 13.

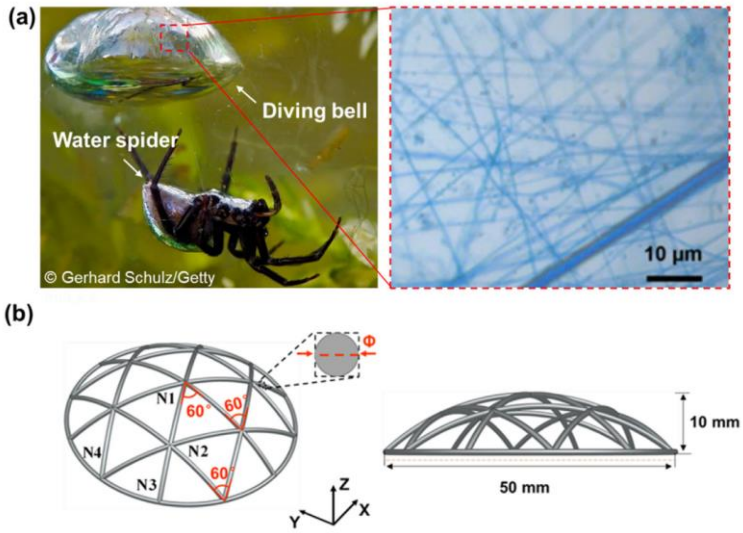

Figure 12: (a) water spider and its diving bell and (b) model of the reticulated shell investigated in [13].

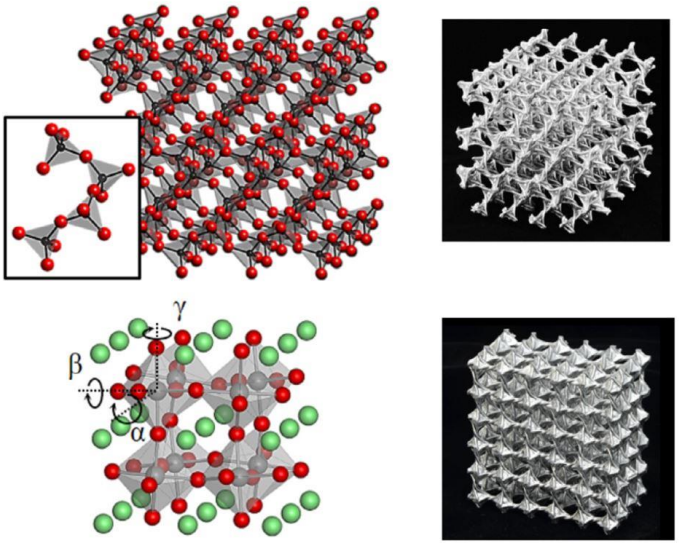

Figure 13: α-cristobalite (up) and $LaNiO_3/SrTiO_3$ (down) crystal structures (left) and inspired-by lattices (right) (from [14]).

Examples of bio-inspired cellular solids are just few of the ones that can be explored and that have actually been explored through literature of the last years. All of them performed good results, especially from the point of view of specific energy absorption, and most of them even surpassed conventional materials. Moreover, cases shown here are strictly related to cellular solids, but nature inspired structures can be found in many other fields such as thin-walled structures, plates and civil engineering structures.

1.1.2 General mechanical properties

Now that the importance of topology (especially the ones inspired by nature) is clear, it is possible to discuss the mechanical properties of cellular solids; in this case [2] is the main reference.

First, one of the most important characteristics of cellular solids is relative density: this property mostly defines mechanical properties of the material itself. Relative density $\bar{\rho}$ is evaluated as the density of the cellular material divided by the one of the material struts/faces are made. Of course, relative density can be evaluated by simple geometrical considerations. Models for the evaluation of this property depending on strut diameter and cell size are often available. Ultra-low-density foams can reach the minimum of $\bar{\rho} = 0{,}001$, classical polymeric foams present instead a relative density between 0,05 and 0,2, softwoods can go from 0,15 to 0,4. Lattices and honeycombs present a vast range, being the generation process more controllable. Relative density in the end is directly linked with geometry of the cell, therefore mechanical properties of cellular solids can be expressed in terms of these parameters. One of the most important documents about it is [2], that can be seen as the milestone of the analysis methodology for cellular solids (and later on for lattices, since in 1983 the concept of lattice structure was not actually developed): Ashby idealized the structure of foams (open-cell and closed-cell), without forgetting the most important physical characteristics, that are strut/shell thickness and cell size (figure 14).

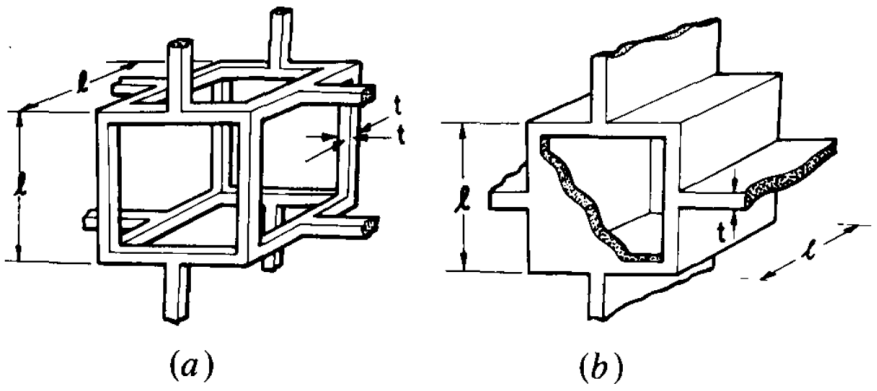

Figure 14: 3D idealized structures for open-cell (a) and closed-cell (b) from [2].

The two idealizations clearly resemble cellulose lattice structures, though, as said, the concept of lattice did not exist. Relative density of the cells can be expressed as it follows:

$$\bar{\rho} \propto \left(\frac{t}{l}\right)^2 \qquad \textit{for open-cell}$$

$$\bar{\rho} \propto \frac{t}{l} \qquad \textit{for closed-cell}$$

When a cellular solid is compressed, its stress-strain curve shows three regions (figure 15). A starting linear elastic section, followed by a plateau at almost constant stress and finally a densification region, coinciding with the cell walls crushing together. Of course, each one of these regions depends on the characteristics of the material.

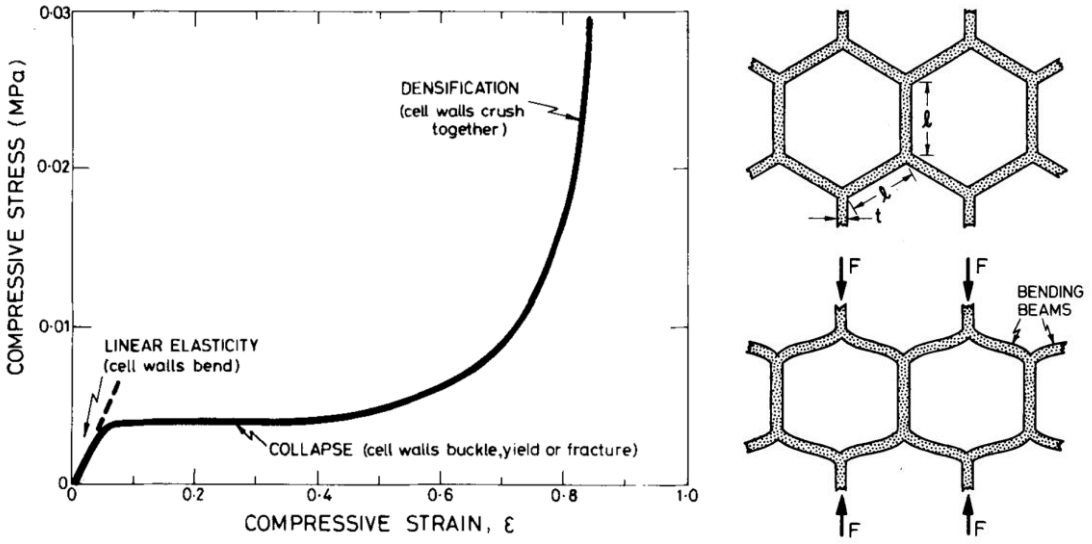

Figure 15 and 16: typical compression stress-strain diagram for a cellular solid (left) and linear elastic deformation of a foam under compression force F (right).

First of all, it is possible to study the linear elastic properties: bending of the struts/walls is the main phenomenon, as it shows figure 16. A defined compression force *F* applied on the material results into a deflection δ, defined from the beam theory as:

$$\delta = \frac{C_1 F l^3}{12 E_s I}$$

Where C_1 is a resolution factor depending on the cell geometry, while E_s is the Young's modulus of the bulk material. Considering the stress proportional to F/l^2, the strain proportional to δ/l and that for open-cell structure the second moment of area I is proportional to t^4, it is possible to obtain:

$$E \propto E_s \frac{t^4}{l^4}$$

Using the proportionality between relative density and t/l, the result is:

$$\frac{E}{E_s} = C_2 \bar{\rho}^2$$

With C_2 that is a constant. Shear modulus behaves the same way.

In a very similar way, plastic yielding can be predicted (when plastic materials are employed, that is in most of the cases). Plastic failure occurs when the moment applied by the force *F* exceeds the fully plastic moment, generating plastic hinges. This fully plastic moment, for a square section beam, can be expressed as it follows:

$$M_P = {}^1\!/_4 \, \sigma_Y t^3$$

The bending moment is proportional to *Fl,* therefore the stress coinciding with the plastic collapse can follows this proportional relationship:

$$\sigma_{pl}^{*} \propto \frac{M_P}{l^3}$$

Using the proportionality between relative density and *t/l*, the result is:

$$\frac{\sigma_{pl}^{*}}{\sigma_Y} = C_3 \bar{\rho}^{3}/_{2}$$

One last example, here reported, about how relative density is linked with mechanical properties, is about crushing strength. Ceramics and some rigid polymers are not affected by plastic collapse, but they are from brittle fracture. Failure occurs when the moment applied exceeds the following one:

$$M_F = {}^{1}/_{6}\, \sigma_F t^3$$

Where σ_F is the ultimate of the bulk material. Again, considering the moment applied proportional to *Fl* and the stress proportional to F/l^2 the collapse of the cellular solids will occur at:

$$\sigma_F^{*} \propto \frac{M}{l^3} \propto \sigma_F \left(\frac{t}{l}\right)^3$$

Using the proportionality between relative density and *t/l*, the result is:

$$\frac{\sigma_F^{*}}{\sigma_F} = C_4 \bar{\rho}^{3}/_{2}$$

The models reported here are just few of the ones that can be found in [2]; many other predictive models about elastic buckling, plastic indentation, creep and tensile fracture toughness have been developed and verified. Of course, when talking about these different properties, distinction between rigid and plastic material need to be done. From a quantitative point of view, this investigation will of course be more explanatory about mechanical properties of cellular solids and lattices.

1.2 Lattice structures

In one of the first cellular solids classification made by Ashby in [1], lattices were not present. In [2] though, the idealization of open-cell foams clearly recalls the concept of lattice structure. In [15], for example, they are classified as open-cell cellular solids, that is a right definition as well, since the impossibility (or extreme difficulty) of creating closed-cell lattices. This is due to the fact that the

most important manufacturing method for lattices is additive manufacturing (AM), therefore the expulsion of powder from closed spaces is impossible. Also, because of the employment of AM, many studies about the topic investigate the microstructure of bulk material forming struts or shells. Examples can be found in [15] and [16]. Mechanical characterization is also a strong topic in lattice literature: since the existence of an enormous amount of topologies and a lot of design parameters, including the AM ones, experimental characterization is essential in this way. Notable mentions in this case are [17], [18] and [19], where is can be seen that methods for the characterization of conventional materials are valid for lattices as well. From mechanical characterization, it is clear that lattices tend to keep the same behavior described in [2] for general cellular solids, where three regions of the stress-strain diagram are highlighted: linear elastic region, plateau region and densification. A further differentiation for this class is possible though: there usually are two different behaviors for lattices, as it can be seen in figure 17.

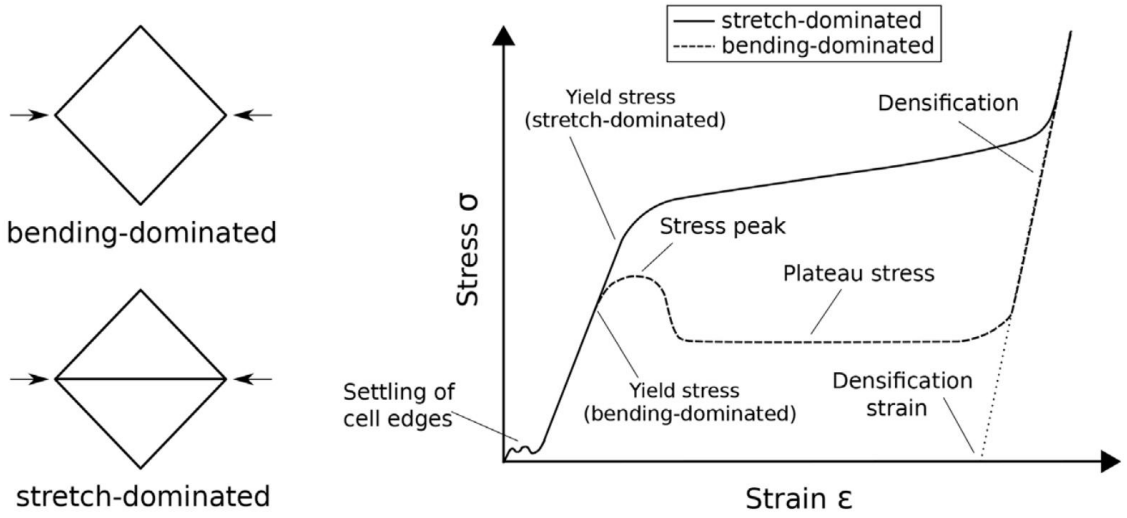

Figure 17: differences between bending and stretching dominated behaviors (from [15]).

In order to establish the behavior, the Maxwell criterion is used: this is associated with the Maxwell number M, that takes into consideration the connectivity of the cell.

$$M = a - 3b + 6$$

Where a is the number of struts and b is the number of nodes. If $M < 0$, the system is bending dominated, while if $M \geq 0$ the system is stretching dominated. The limit between the two behaviors is not so clear and defined though, and the Maxwell number is just a general indicator. Mechanical properties of lattices will become clearer in the next chapters, because of the main topic of this investigation. A deeper look at manufacturing methods and applications is given in the next sections.

1.2.1 Additive manufacturing for lattices

Of course, among all of the manufacturing processes existing, additive manufacturing is the most suitable and employed for lattice structures. Most of the huge number of topologies that lattices can present are manufacturable using AM: that allows a huge design freedom. AM is defined as the process of forming a 3D product by adding material in a series of layers, rather than subtracting it, and here lies the mentioned design freedom, especially for topologically complex structures such as lattices. Though Stereolithography (SLA) has been used in early stages of AM, especially for non-metal structures, it has been employed for polymeric lattices as well. The most used AM process used for lattices are the one employing metal powders: Selective Laster Sintering (SLS), Selective Laser Melting (SLM) and Electron Beam Melting (EBM) are for sure the most used methods nowadays. Especially SLM is by now the best option, since it is the methods resulting into less microstructure imperfections; in fact, EMB can generate severe defects due to the excessive power employed in the process.

According to [15], when it comes to lattices (especially truss-like ones), there are two manufacturing strategies that can be considered (see figure 18): point-exposure (PE) and contour-hatch (CH).

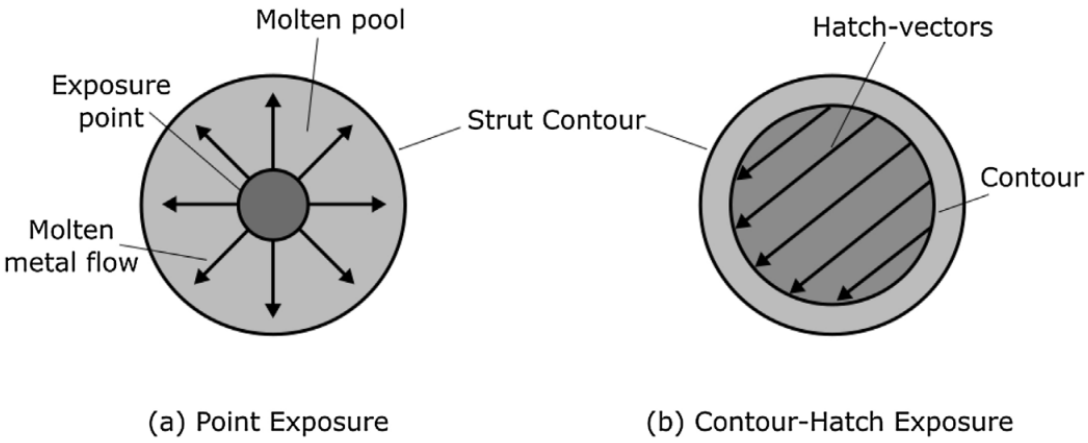

Figure 18: point exposure and contour-hatch diagrams (from [15]).

Point-exposure strategy consists of keeping the laser beam on the same exposure point (part of a cloud of points defining a single layer) for a certain amount of time until the heat flow generates a molten pool around the point itself. Of course, PE is unconventional for AM, and requires a particular slicing code and generates rougher strut surfaces, on the other hand this strategy is faster than conventional ones and it allows the manufacturability of thinner struts. Contour-hatch strategy is a standard one: geometry contour is melted first; the internal area is melted using hatched vectors in a second time. Being the conventional strategy, classical slicing codes are employed and surfaces present better quality. It is by the way slower, therefore more expensive, than PE. Advantages and disadvantages of

these two strategies need to be weighted depending on the topology of the lattice and its geometric parameters.

While it is true that AM is among the best options for lattices, also limits are present as well (see [4]). First of all, support structures are needed in case of overhanging part of the printed item: these avoid the powder present under overhanging struts to collapse under the weight above. Also supports are needed for heath dissipation and prevention of distortions. Other limits of AM are of course about the material: not every existent material is manufacturable. In fact, the most used materials for lattice manufacturing are steel, aluminum and titanium alloys suitable for AM (AlSi10Mg and Ti6Al4V above all). Also, sizes could be a problem: struts are in most of the cases larger than the CAD model; this is due to the expansion of the melting pool. Hollow struts and closed cells are a problem as well: for the first ones it might be difficult to evacuate powder from the inside, for the seconds it is basically impossible.

1.2.2 Applications

Lattices present different application fields, covering sectors such as aerospace, automotive and biomedical ones. A few examples of lattices employment can be found in the following paragraphs.

In [20], Kagome, Hexagonal (that can also be called *bcc*) and cross pyramidal cell types have been tested in order to gather information about their elastic properties: that is because this is a benchmark study for the development of the internal structure of a UAV wing, that needs flexibility of movement. The proposed model for the wing design can be seen in figure 19.

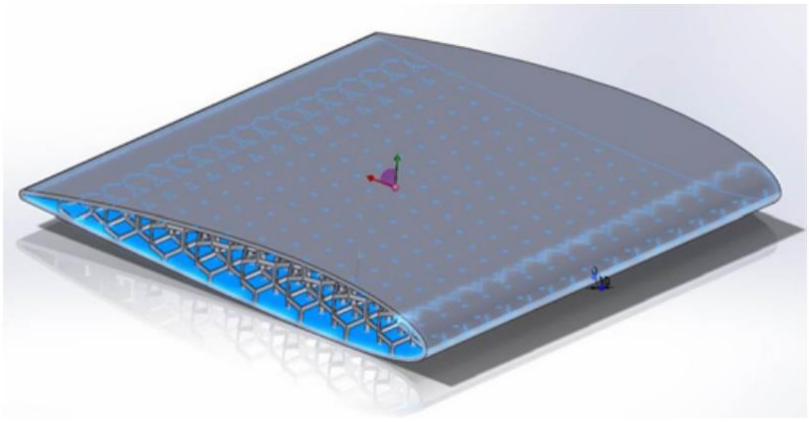

Figure 19: model for the wing design proposed in [20].

Another example concerning the aerospace field can be found in [21], where *bcc* and *bccz* lattices have been studied and characterized in order to use them for the design of an anti-icing system for the leading edge of an aircraft wing (figure 20): here the impact energy absorption (since leading

edges are often subject to bird-strike and accidental loads) and heat regulation capacities of lattices are both exploited.

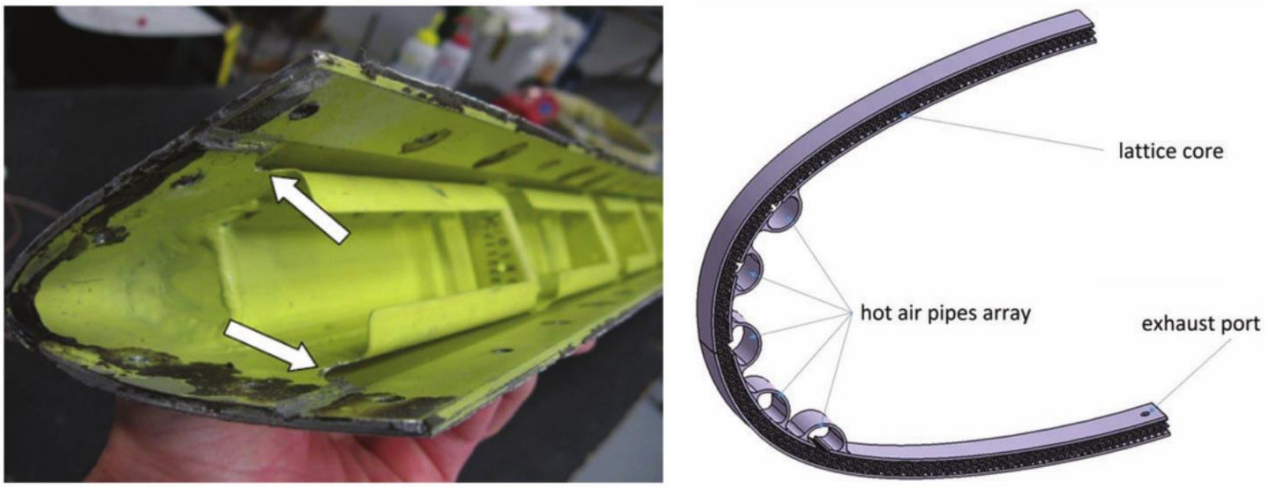

Figure 20: traditional thermal anti-icing system (left) and the one making use of lattice core (right) proposed in [21].

Lattices, thanks to their good mechanical properties and lightweight, perform excellent results in the aerospace field. They are as well employed in the automotive sector: [22] is an investigation about the possibility of using a lattice core for the sandwich panels forming the engine hood of a vehicle. Schematic pyramid cell type is used for the generation of a lattice core, that can be seen in figure 21. Also, this investigation makes use of a homogenization method for the modeling of the lattice, making the model lighter from a computational point of view.

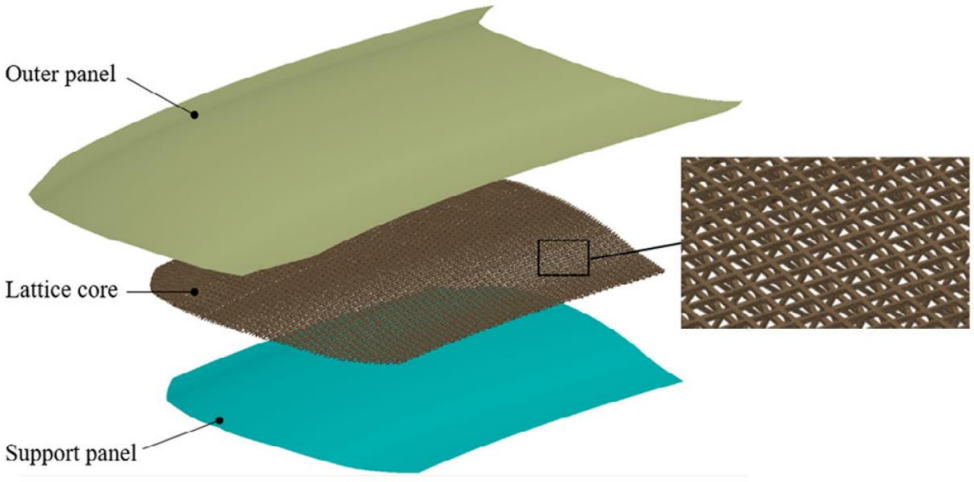

Figure 21: exploded view of the engine hood sandwich structure (from [22])

Another study making use of these structures for the automotive field, F1 actually, is [23]: here a roll-over component for F1 vehicles has been developed employing a hybrid design. Lattice optimization

has been performed on a defined part of the roll-over (figure 22); in this case also homogenization has been useful in making the model lighter.

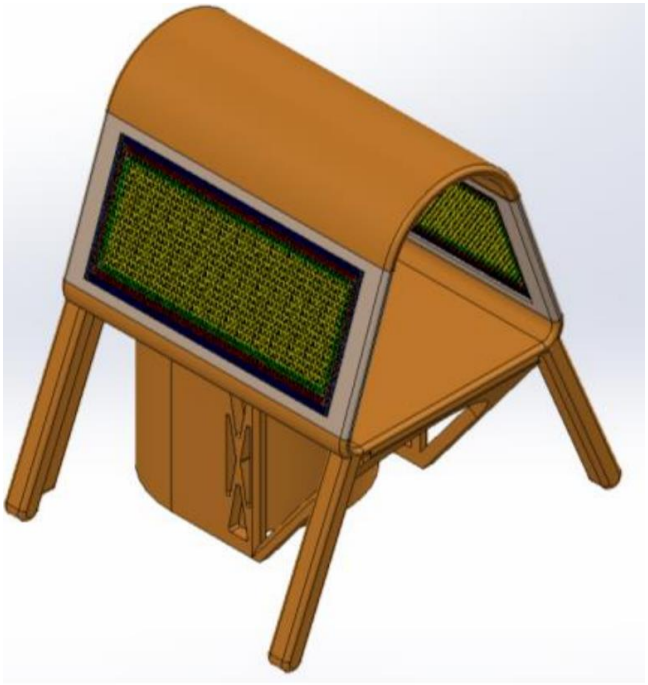

Figure 22: hybrid design proposed for the F1 roll-over in [23].

Often, lattices are used in heat exchangers as well, that is a similar employment as the one found in [21]. Heat management, due to their parametrizable porosity (besides the material used as bulk), is essential in this case. Another example can be found in [24].

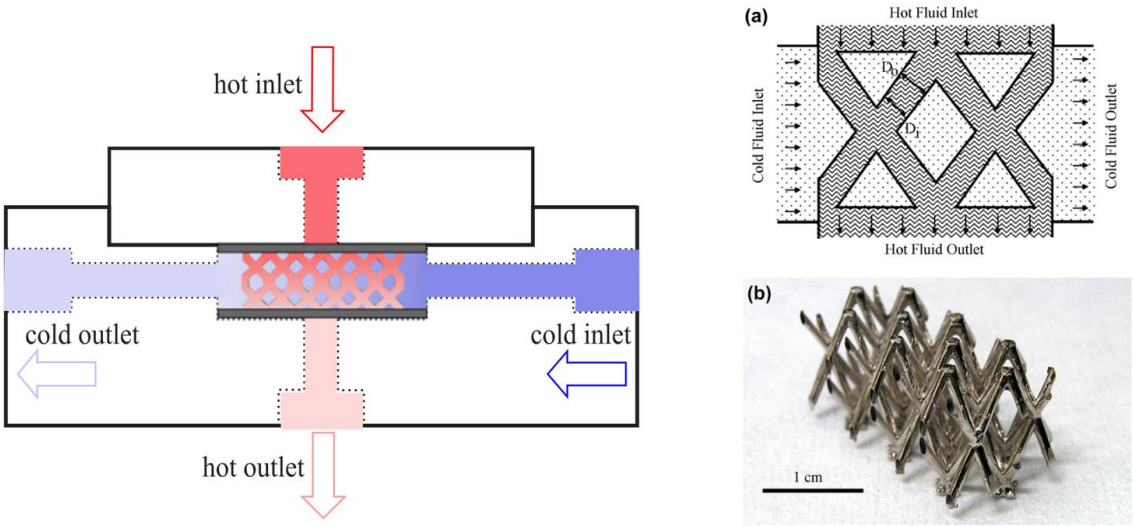

Figure 23: design of the heat exchanger (left), details of the lattice section (a) and lattice picture (b) (right) proposed in [24].

Figure 23 shows the design of this heat exchanger that is meant to be as multifunctional: lattices, in fact, besides the heat flow regulation also works as structural support reducing the system-level parasitic weight. Last example, that can be found in [25], comes from the biomedical sector: here a

femoral prothesis for a hip implant has been designed using lattices in a defined design zone, as it can be seen in figure 24.

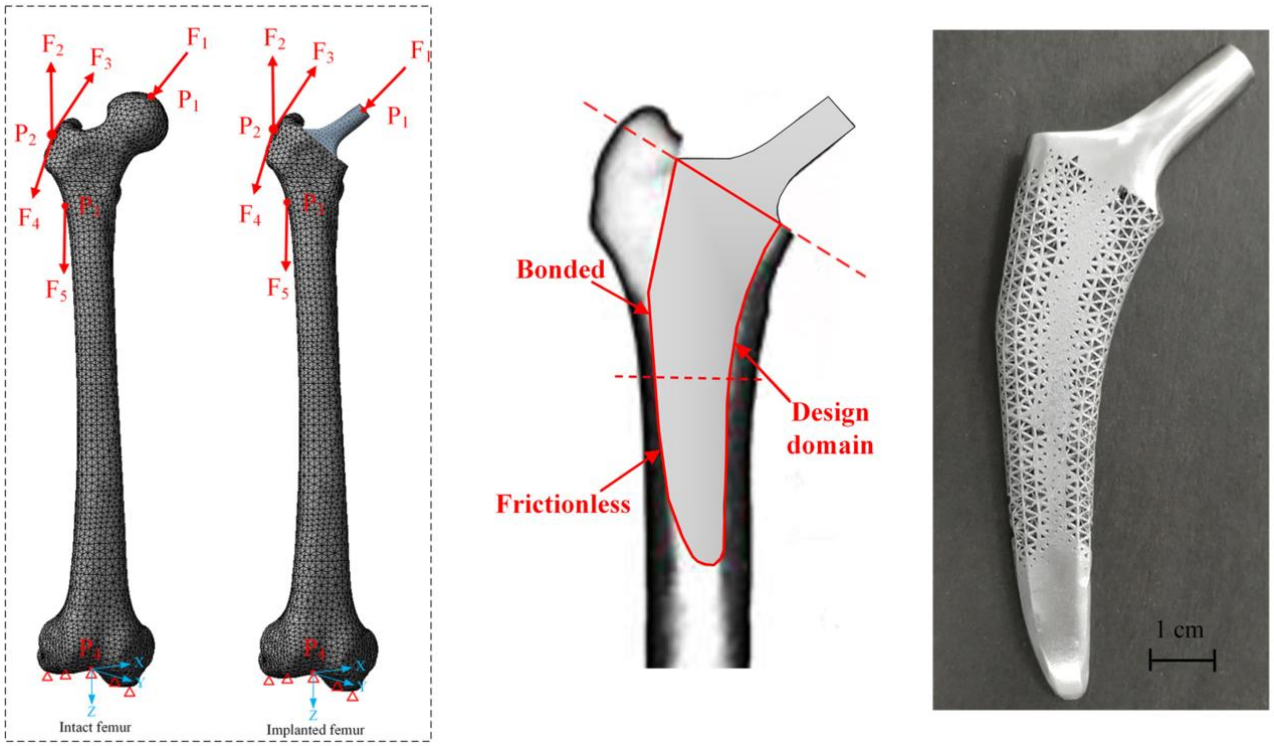

Figure 24: FE model with relevant physiological loadings and boundary conditions obtained from in vivo measurements on an instrumented hip (left), design domain (middle), and printed prothesis (right) (from [25]).

This design makes use of a titanium-based alloy, as for most of the biomedical applications using lattices. Apart from the good mechanical properties that lattices can provide, because of their porous structure, they are extremely good for the osseointegration property as well.

This investigation, as said, will be based on lattices rather than cellular solids in general. Next chapter will analyze modern literature about the most employed cells for energy absorption applications: once these will be established and selected, their mechanical characteristics will be deepened and confrontations between different topologies (based on truss lattices, where the motivation for this choice will be justified later) will allow the definition of guidelines that can lead the engineer into an energy absorption design based on the cells that have been selected for the project. Also, this study wants to offer a methodology for the approach to lattices analysis, in particular for the energy absorption field.

2 Cell selection and general model

After a general overlook at the world of cellular solids and lattice structures from the point of view of general characteristics and applications, it is time to give a deeper look at the mechanical properties with a special attention to energy absorption. It is difficult to perfectly rank all kind of existing cells because there are too many variables to be aware of: material, strut dimension, orientation angles, grading, quality of the printing process (or in general, of the manufacturing process). It is possible by the way to understand which the direction to follow is once the most general behavior is defined, based on the topology of the cell considered. Many suggestions can be found in literature: with the help of [4], a very interesting review about mechanical properties of a big part of the lattice world, the lattices to considered for this investigation has been selected.

After the selection of the cell will be concluded, the most general model which will be used for the future simulations will be discussed, going from geometry creation to the boundary conditions.

2.1 Cell selection

What is evident here is that the most used cells for energy absorption are classical ones such as *bcc* and *fcc* (and their reinforced versions), auxetic cells and rhombic dodecahedron: in this chapter, these cells will be reviewed as candidates for this investigation.

2.1.1 *bcc*, *fcc*, reinforcements and combinations

As a starting point, [26] can be very helpful: even though the material considered is Inconel 625 (while here the definition of the material for this study has not been clarified yet), the main parameter is the cell topology.

Cell type	Body Centred Cubic	Body Centred Cubic (Z Struts)	Face Centred Cubic	Face Centred Cubic (Z Struts)
	BCC	BCCZ	FCC	FCCZ
	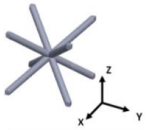			
Struts, *s*	8	12	16	20
Joints, *n*	9	9	12	12
Strut inclination angles, α	35.3°	90°,	45°	90°,45°
Maxwell number, *M*	−13	−9	−14	−10
Strut aligned to load direction	NO	YES	NO	YES

Table 1: cell topology, Maxwell number and load-aligned struts for candidate unit cell lattice structures (from [26]).

Compression test were conducted over manufactured samples according to ASTM standard with topologies displayed in Table 1, varying cell size, cell number and strut dimension. From these tests, typical behaviors were evident from stress-strain diagrams:

- *fcc* cell is stiffer and present a higher strength than *bcc* cells.
- Z struts increase the strength.
- Both *bcc* and *fcc* are bending dominated, but the addition of Z struts makes the behavior tending toward stretching dominated (even though *bccz* and *fccz* are nominally bending dominated still); this is due to the different collapse mode of vertical struts.
- Increasing cell size typically results into decreased strength and moduli.

Regarding energy absorption, it rises with the addition of Z struts: pure energy absorption is by the way not the only property to take care of in the field of crashworthiness and impact. Future investigation will be useful to find out if Z struts are also good for the efficiency of the impact as well (that depends on peak and plateau stress and will be investigated in the next chapters). Specific energy absorption (evaluated using mass) reaches its maximum for *fccz* and *bccz*, though *bccz* performs at the same level as *fccz* only for higher strains (see figure 25).

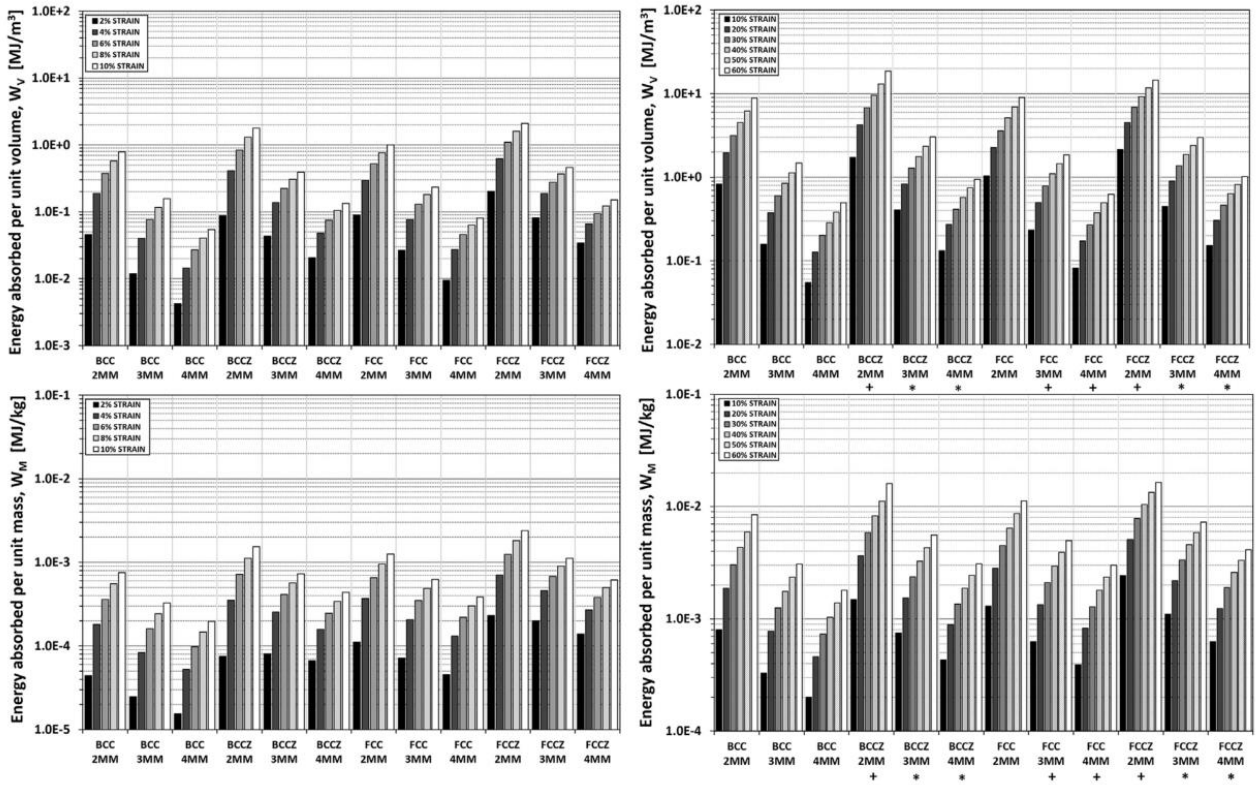

Figure 25: Energy absorption per unit volume (W_V)(upper) and per unit mass (W_M)(lower) of tested lattice specimens for lows strain(left) and high strain (right) scenarios. Values presented up to specified strain integration limit. Legend: asterisk (*) identifies scenarios that display distinct plastic collapse, cross (+) identifies less pronounced plastic collapse (from [26]).

Something more can be said about the transition point: *bcc* and *fcc* tend to present a stress-strain diagram with a linear plateau, and that is typical for bending dominated cells. When Z struts are applied, the transition from bending to stretching dominated is evident: *bccz* and *fccz* present in fact oscillations in the plateau that represent nothing else than the progressive failures of Z struts in different rows.

Another interesting investigation can be found in [27]: the material, that is stainless steel, is different from the previous case but once again the interest is focused on topologies. Compression tests are performed on *bcc* and *bccz* cells in three different ways: actual compression tests over manufactured samples, a FEM beam model and a FEM 3D one. The way the beam model has been created is quite interesting: beams do not present a constant section along the beam axis, but the extreme sections have a larger diameter in order to take account of the excess material in the nodal regions, that is typical in the additive manufacturing processes (fig. 26); it has to be said that this assumption for modeling has not been considered for this investigation.

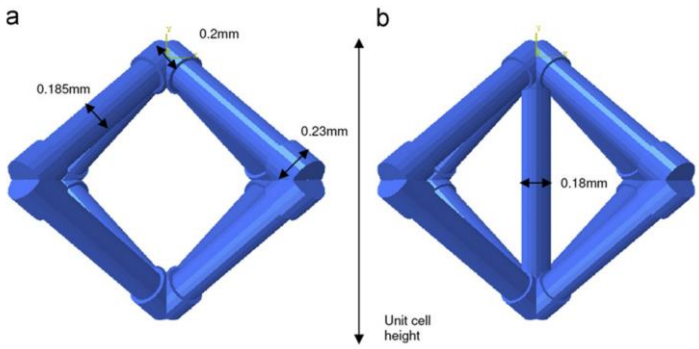

Figure 26: dimensions of the beam element model for (a) the *bcc* unit cell and (b) the *bccz* unit cell (from [27]).

In the following tables (2-4), where differences between tested samples are shown, the previously described behavior is evident: *bcc* cells tend to absorb less energy than *bccz* ones, which by the way reach higher peaks in stress (and consequentially higher is the force applied, since stress and force are liked through the section area of the sample).

Lattice ID	Unit cell type	Relative density, ρ^* (%)	Young's modulus, E (MPa)	Initial peak stress, σ_{pl} (MPa)	0.2% yield stress, $\sigma_{0.2\%}$ (MPa)	Plateau stress (at 25% strain) (MPa)	Energy absorbed up to 50% strain (J)
A	BCC	13.9	207.5	–	2.56	4.58	17.90
B	BCC	9.7	105	–	0.83	1.62	6.30
C	BCC	5.4	19.8	–	0.27	0.49	1.90
D	BCC	3.5	10.6	–	0.16	0.28	1.10
E	BCC-Z	15.9	2273.2	10.31	7.02	7.81	34.30
F	BCC-Z	11.1	1506.2	4.85	3.33	4.29	17.00
G	BCC-Z	6.2	804.9	2.00	1.84	1.54	6.00
H	BCC-Z	4.0	84.6*	1.06	1.04	0.72	2.90

* Initial stiffness was not measured from the unloading curve

Table 2: summary of the experimental compressive properties of the 20 mm^3 lattice structures (from [27]).

Lattice ID	Unit cell type	Relative density, ρ^* (%)	Young's modulus, E (MPa)	Initial peak stress, σ_{pl} (MPa)	0.2% yield stress, $\sigma_{0.2\%}$ (MPa)	Plateau stress (at 25% strain) (MPa)	Energy absorbed up to 50% strain (mJ)	Normalised energy absorbed up to 50% strain (kJ kg^{-1})	Energy absorbed for 20 mm^3 lattice (J)
A	BCC	11.4	236.9	–	2.13	3.45	3.26	1.88	13.35
B	BCC	8.1	105.9	–	1.09	1.76	2.87	1.34	6.31
C	BCC	4.7	31.8	–	0.37	0.61	2.34	0.80	2.34
D	BCC	3.1	12.3	–	0.17	0.28	2.06	0.55	1.06
E	BCC-Z	16.7	2261.1	10.02	4.51	9.13	8.65	3.41	35.44
F	BCC-Z	11.3	1532.3	4.71	2.80	3.58	7.33	2.46	16.10
G	BCC-Z	6.2	811.2	1.86	1.40	1.26	5.30	1.38	5.30
H	BCC-Z	3.9	547.2	0.97	0.85	0.58	4.79	1.00	2.45

Table 3: unit cell and lattice properties for the beam element models (from [27]).

Lattice ID	Unit cell type	Relative density, ρ^* (%)	Young's modulus, E (MPa)	Initial peak stress, σ_{pl} (MPa)	0.2% yield stress, $\sigma_{0.2\%}$ (MPa)	Plateau stress (at 25% strain) (MPa)	Energy absorbed up to 50% strain (mJ)	Normalised energy absorbed up to 50% strain (kJ kg^{-1})	Energy absorbed for 20 mm^3 lattice (J)
A	BCC	11.36	227.8	–	1.83	3.44	3.23	1.87	13.20
B	BCC	8.13	112.6	–	0.94	1.74	2.82	1.32	6.20
C	BCC	4.71	35.6	–	0.34	0.61	2.34	0.80	2.30
D	BCC	3.08	13	–	0.17	0.28	2.09	0.56	1.10
E	BCC-Z	12.7	2817	11.00	4.62	10.5	9.8	5.10	40.30
F	BCC-Z	9.12	2123	4.77	2.90	4.57	7.77	3.24	17.10
G	BCC-Z	5.32	1053	1.93	1.51	1.36	5.76	1.73	5.80
H	BCC-Z	3.5	621	1.00	0.91	0.58	4.85	1.14	2.50

Table 4: unit cell and lattice properties ofr the 3D brick element models (from [27]).

Also, it is evident how relative density plays another important role in the definition of the mechanical properties: that marks the difficulty of properly ranking properties for lattices, where there are so many variables.

From the point of view of dynamic crashing and impact load test, [28] offers a good perspective on how things change when it comes to this type of loading actions: dropping weight is used for dynamic loading while ballistic pendulum for blast load impact; stainless steel 316L is the used material. Besides classical properties such as stiffness and strength, the response to strain rate can also be investigated as we can see in figure 27.

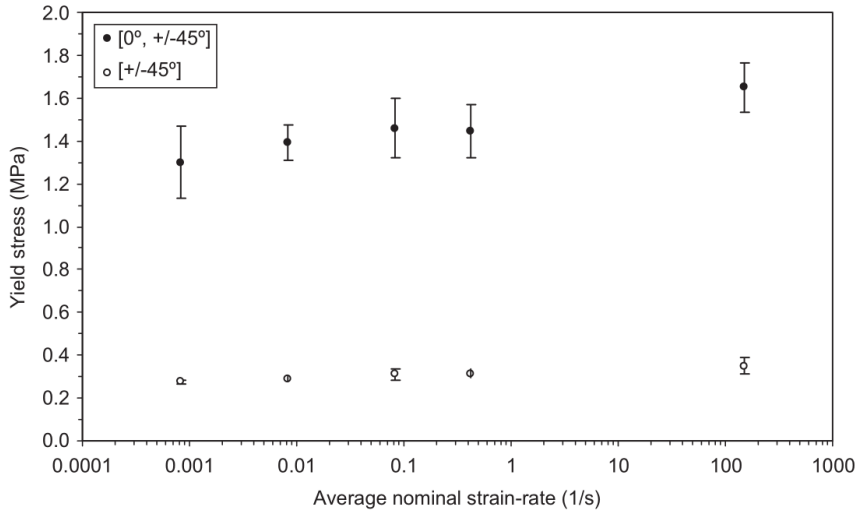

Figure 27: the variation of yield stress with crosshead displacement rate for the *bccz* (that in the article is named as [0°, ± 45°] pillar octahedral lattice) and *bcc* (named as [± 45°] octahedral lattice) (from [28]).

Though differences are not so evident going from quasi-static load case to dynamic one, especially for *bcc*, *bccz* presents a rise in the yield stress when it comes to higher strain rates: from this diagram it can be concluded that the addition of Z struts makes the lattice more responsive to the strain rate; that is reasonable, since vertical struts are the most exposed ones to the loading action and therefore to the type of loading action.

Another interesting part of this investigation is about being able to predict dynamic properties by performing quasi static tests. About that, figure 28 shows the relationship between specific energy absorption in the quasi-static condition and the impulse to achieve 50% crashing under blast load condition.

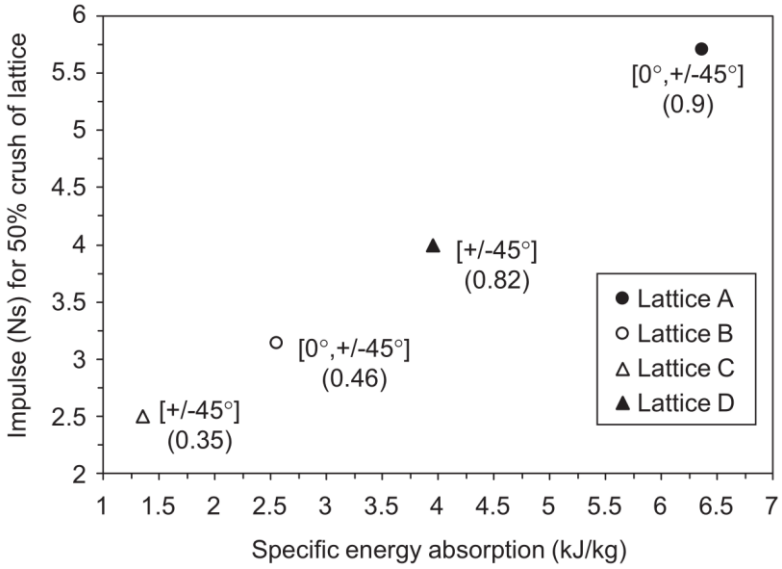

Figure 28: Relationship between SEA under quasi-static conditions and the measured impulse from the blast load to crush lattices by 50% (nomenclature is the same as figure 3, while number in brackets represent density) (from [28]).

The linear relationship between these two properties belonging to different ways of loading application suggest that it is actually possible to predict dynamic properties from quasi-static tests because a similarity is present. In the next chapters further investigations about this possibility will be deepened.

Another interesting study is [29], and it revolves around different kind of cells: Kagome, *bcc*, *f2cc*, and *f2bcc*; the material used is Ti6Al4V. Figure 29 shows a confrontation from the point of view of specific energy absorption and specific strength, for both compression and shear tests keeping constant the strut diameter: Kagome cells perform the highest SEA and specific strength, though they are not studied that much with regards to EA (probably because of their peaks in stresses, in fact Kagome cells presents in most cases an orientation angle higher than 45°, that is typical for *fcc*).

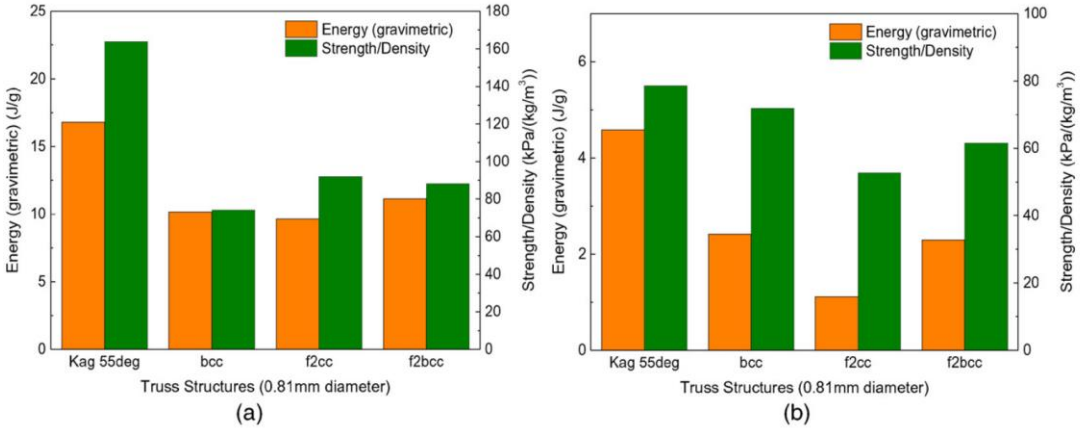

Figure 29: Comparison of analyzed unit cell structures for (a) compressive gravimetric energy and specific compressive strength and (b) gravimetric shear energy and specific shear strength (from [29]).

The combination of *bcc* and *f2cc*, that is *f2bcc*, perform higher SEA than the two single original cells and a slightly lower specific strength than the simple *f2cc* for both compression and shear: this shows that with combination of cells better performances can be achieved and this consideration will be used for the selection of the candidate for this study.

One last investigation about classic cells is [30], where the focus is on *f2cc* and the material considered is Al12Si aluminum alloy. Grading with thickening going toward the fixed plate is also considered in this article, showing good performances as we can see from Table 5.

Energy absorption	F2BCC lattice	
	Uniform	Graded
$Wv\ (MJ/m^3)$	2.6 ± 0.2	3.2 ± 0.1

Table 5: energy absorption properties of uniformly and gradually dense lattice structures (from [30]).

When it comes to grading, also volumetric energy absorption is very important: as it is possible to see from figure 30, graded structures can achieve higher volumetric energy absorption for medium-to-high strains below which unform lattices seems to work better.

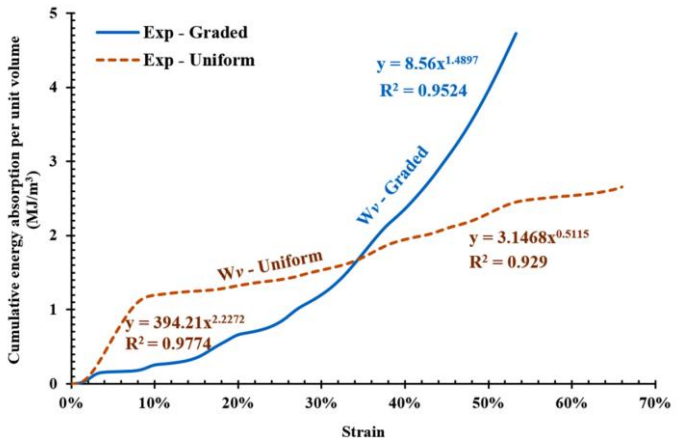

Figure 30: volumetric energy absorption over compressive strain for uniform and graded structures (from [30]).

2.1.2 Auxetic structures

Auxetic structures and auxetic lattices are good options as well when it comes to energy absorption properties. [31] shows it: quasi-static and dynamic test were performed over three sample types (fig. 31), material used is 316L-0407 austenitic stainless steel alloy. Dynamic tests have been performed using Split Hopkinson Pressure Bar (SHPB) that is an evolution of the simple Hopkinson Pressure Bar (HPB): this apparatus is and has been widely used for the study of energy absorption at high strain rates for a huge range of materials, going from bulk metals to cellular solids.

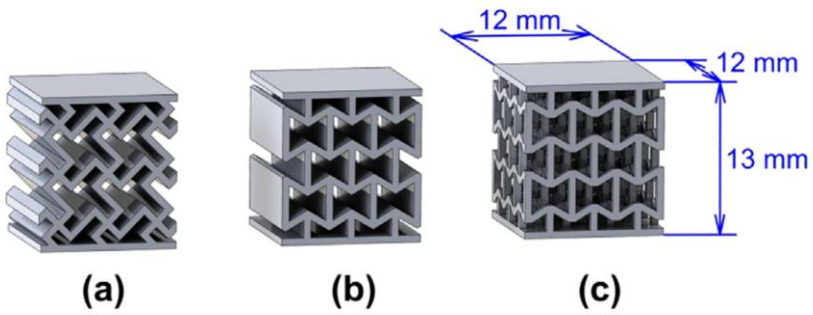

Figure 31: auxetic structures considered where (a) is the 2D missing rib, (b) is the 2D re-entrant and (c) is the 3D re-entrant (from [31]).

Fillers are also considered in this investigation: low expansion polyurethane, ordnance gelatin and no filling at all have been used. Stress-strain diagrams obtained are displayed in the following figures.

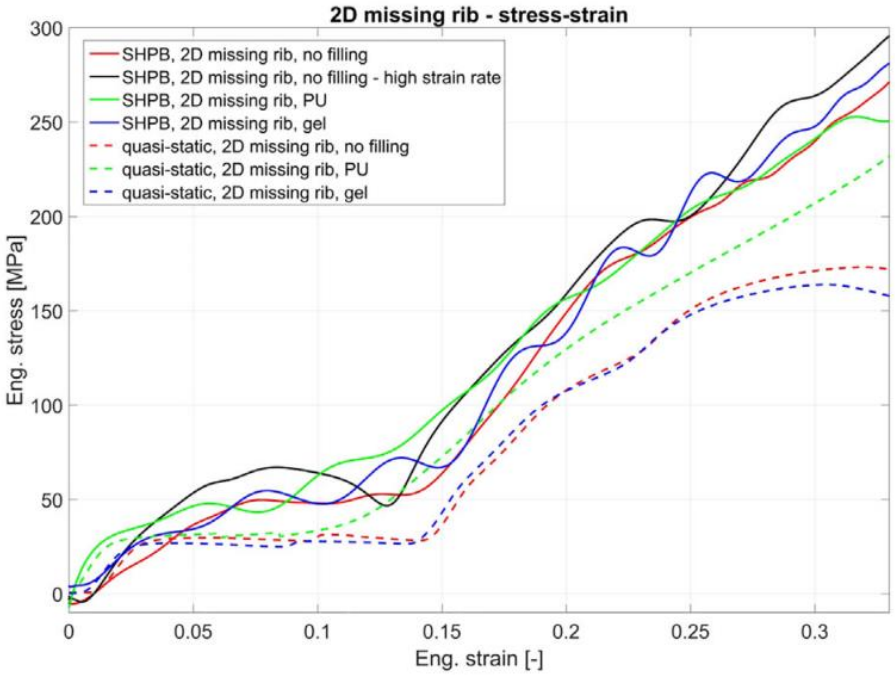

Figure 32: stress-strain curve for the 2D missing rib (from [31]).

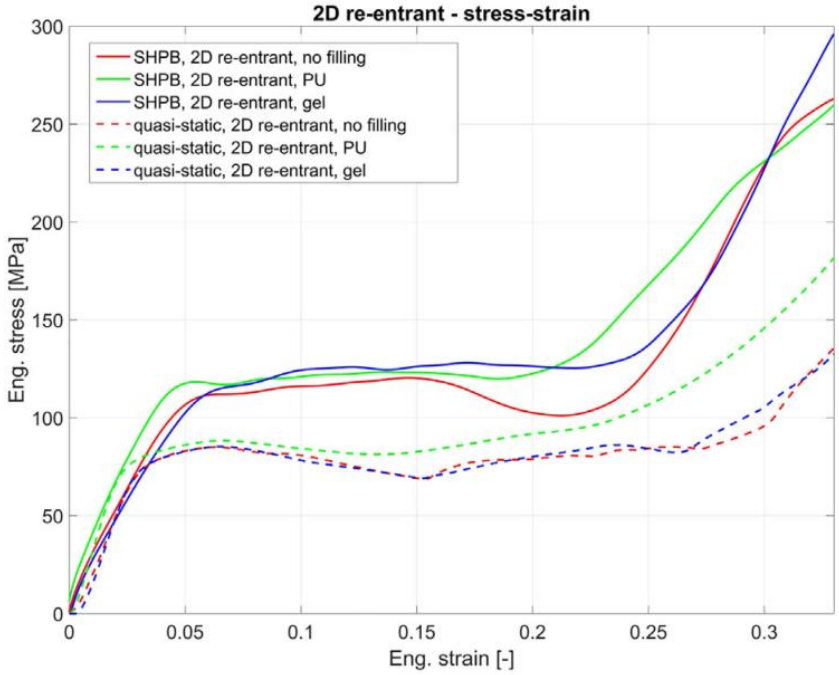

Figure 33: stress-strain curve for the 2D re-entrant (from [31]).

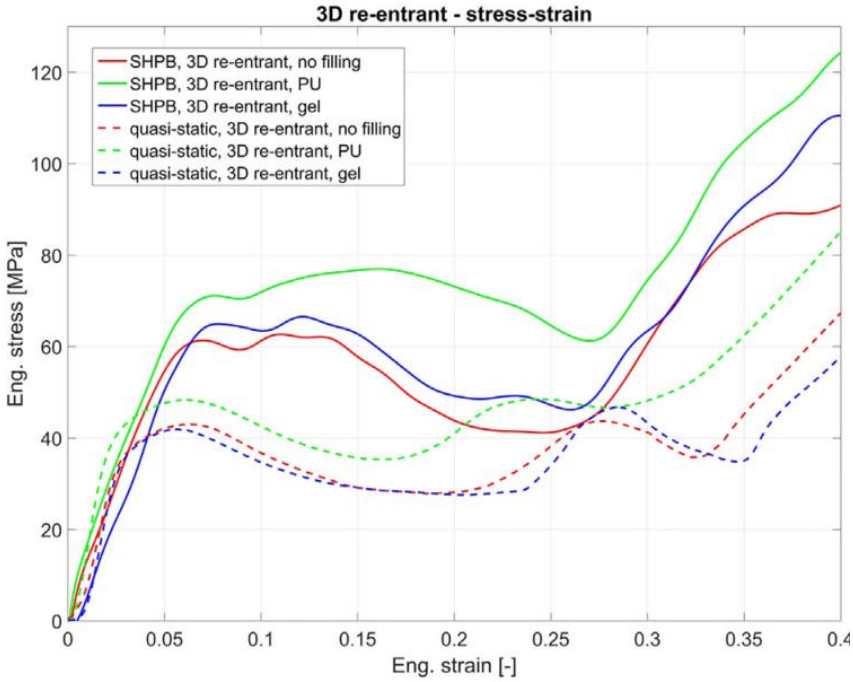

Figure 34: stress-strain curve for the 2D re-entrant (from [31]).

There is no huge difference between diagrams for filled lattices and diagrams with simple ones: that is actually a good indicator, in fact the filling is inserted in order to make a small but effective difference in the properties the study is investigating; if instead, the addition of the filler makes the diagrams extremely sensitive to the addition itself, that means the mechanical properties of the lattice are irrelevant to the ones of the filler. In other words, the filler needs to be “lighter” from the point of view of mechanical properties.

Energy absorption analysis has been carried out with a particular attention to the plateau region, that is extremely important in such cases. Results are showed in Table 6.

	Average plateau stress			Specific energy absorption ratio	Filling/No filling plateau energy ratio	
	Static	Dynamic	Ratio	Dynamic/Static	Static	Dynamic
			2D re-entrant			
No filling	80 MPa	113 MPa	1.41	1.43	–	–
PU	85 MPa	121 MPa	1.42	1.42	1.09	1.06
Gelatine	79 MPa	123 MPa	1.53	1.58	1.00	1.11
			3D re-entrant			
No filling	33 MPa	51 MPa	1.56	1.55	–	–
PU	40 MPa	72 MPa	1.73	1.71	1.27	1.39
Gelatine	31 MPa	56 MPa	1.70	1.78	0.96	1.09
			2D missing rib			
No filling	30 MPa	49 MPa	1.66	1.66	–	–
PU	34 MPa	57 MPa	1.69	1.70	1.15	1.18
Gelatine	28 MPa	52 MPa	1.76	1.95	0.90	1.06

Table 6: energy absorption results (from [31]).

Both specific energy absorption and plateau stress tend to increase going from the static to the dynamic case as it is possible to see from the ratios. Fillers, especially polyurethane, acts in a positive way in most cases.

Many articles can be found in literature about auxetic materials from the point of view of dynamic/impact loading. Also, comparisons between quasi-static and dynamic cases are offered, especially in the field of the auxetic re-entrant structures as we can see in [32], where one out of two lattices investigated is the re-entrant cube and once again the apparatus used for testing in the dynamic case is the HPB (here also modeled for a FEA). [33] offers instead a good perspective on the world of auxetic lattices both from the point of view of impact properties and energy absorption, but the only material used is ABS.

2.1.3 Rhombic dodecahedron

According to [4], another cell shape that presents a very good energy absorption level is the rhombic dodecahedron.

In [34] it is possible to see that good levels of SEA are reached from both experimental tests and FEA simulations. Of course, SEA rises together with relative density, but another parameter that defines this property is what has been introduced as shape parameter α. This parameter basically influences the topology of the cell, acting on the struts: going from 0 to 1, when $\alpha = 0$, the modified lattice structure degrades into the original one (see figure 35). This study revolves around the effects of varying the section of the struts. Best SEA, yield stress and compressive moduli are obtained with $\alpha \simeq 0{,}4$ (figure 36).

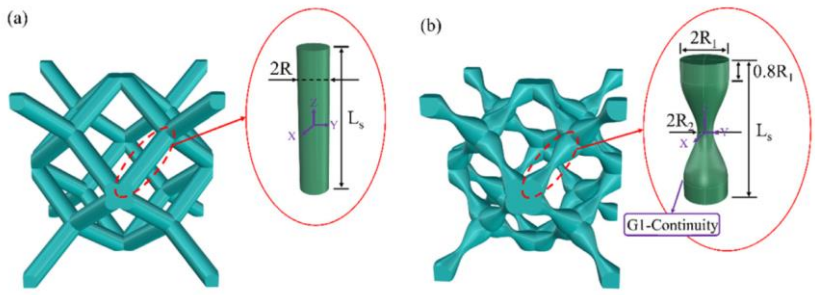

Figure 35: the original (a) and the modified (b) RD unit cell (from [34]).

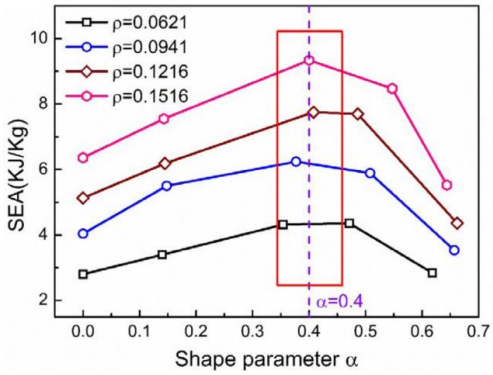

Figure 36: SEA for different shape parameters and relative densities (from [34]).

The material used in this investigation is stainless steel, while in [35] the used one is Ti6Al4V: here the investigation is about the effects of temperature, going from 200°C to 600°C, on mechanical properties. It is demonstrated that a temperature of 200-400°C tend to increase energy absorption but it also has to be considered that this improvement depends a lot on the material we are using.

One last interesting study is [36], that is the continuation of [34]: here the rhombic dodecahedron is investigated form the point of view of impact load. The apparatus used is once again the SHPB. Different impact speed has been used for the generation of stress-strain diagrams, used to obtain SEA. Also, shape parameter is considered again.

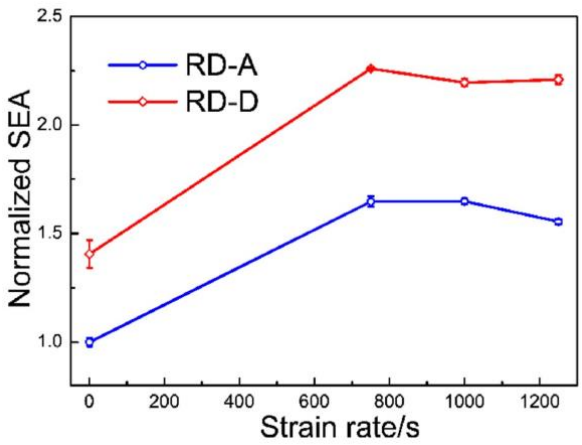

Figure 37: Normalized SEA over Strain rate for RD-A (α = 0) and RD-D (α = 0,3) (from [36]).

It is possible to appreciate how a shape parameter different than zero tend to increase the SEA, as well as a higher strain rate than the quasi-static one.

2.1.4 Discussion

As said, thanks to [4], it has been possible to consider a wide range of lattices where structural function is the main aim, with a special attention to energy absorption. Once achieved all of the important points in the last years literature, the requirement is now the generation of a workspace for this very investigation. Energy absorption properties are extremely important in the lattice world, since one of their main application consists of being a crashing/impact absorber. Many other lattices, like octet-truss and shell lattices do not offer good possibilities in the EA field because their main applications are linked with their high stiffness. The family of *bcc* and *fcc* simple truss lattices seems to be a good starting point for an investigation about impact energy absorption: many studies have been developed about these structures, but none of them analyze the evolution of their behavior going from simple cells towards combination or reinforcement in the field of high strain rates (in other words, impact and crashworthiness). Also, besides the fact that truss lattices are preferred to be manufactured with powder bed based AM technologies (that have been mentioned in the previous chapter), their mechanical behavior is much easily predictable and simpler to study with respect to shell lattices. It would be useful to go from statics to dynamics also trying to understand if there is a tendency to keep good energy absorption properties in this passage or even if there is the possibility to predict dynamic properties by looking at static ones, as in [28]. The family of auxetic lattices offers excellent possibilities as well, but the functionality of these structures made the investigations in the last years much deeper than for other lattices. The research in this specific field is far more complete than for other families, also from the point of view of the material used for the manufacture; also new auxetic structures are developed constantly, and the huge number of parameters they present makes difficult to develop a general investigation about energy absorption. While for the rhombic dodecahedron the issue is about the complexity of the cell itself that also does not offer many possibilities for modifications and combinations.

Pondering all the considerations made up to now, the final choice for the lattices that are going to compose the workspace for this investigation has fallen upon the *bcc* and *fcc* families: not only these two lattices are going to be considered but also their reinforcements and combination, so *bcc*, *bccz*, *fcc*, *fccz*, *fbcc* and *fbccz* (figure 38). Besides energy absorption properties for *bcc* and *fcc* themselves, in this way there is also the possibility to compare results for reinforcements and combinations considering advantages and disadvantages. Moreover, *bcc* presents a 35°26’ orientation angle, while

fcc presents a 45° orientation angle: a confrontation in this sense is possible as well. In the next sub-chapter sizes and modeling will be discussed in order to completely define the topologies selected.

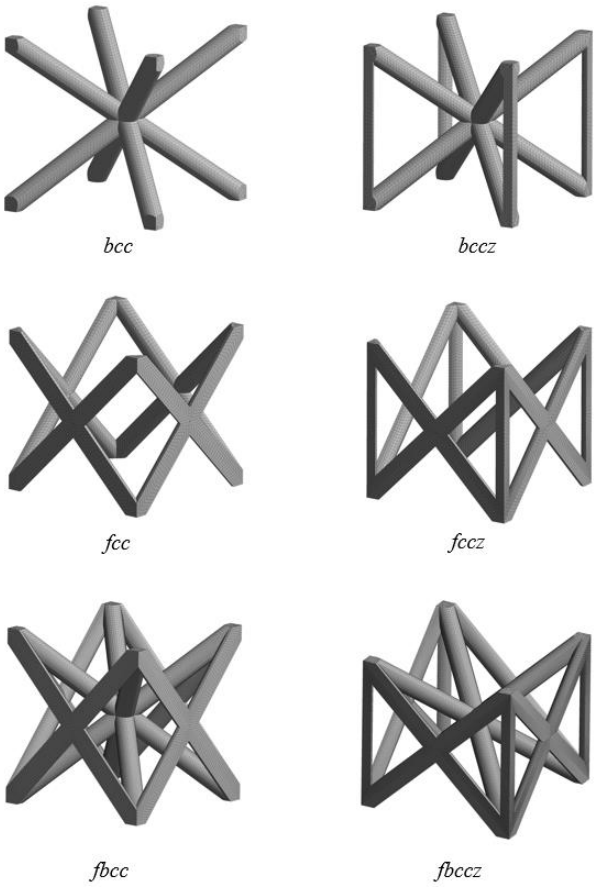

Figure 38: cell set considered for this investigation.

2.2 General model

In this investigation, simulations have been performed in different ways when it comes to statics and dynamics. A general base is by the way always present and valid especially for materials definition and geometry generation.

2.2.1 Material

The point of the material to use for the simulations really depends on the way lattices are manufactured, that is in most of the cases additive manufacturing. Biographical references up to now consider a wide range of materials: stainless steel, Ti6Al4V (or in general titanium alloys that are additively manufacturable) and aluminum alloys. In the end, the choice has fallen upon AlSi10Mg for different reasons. First, this alloy is one of the most used among other aluminum alloys in the field of lightweight structures. Other aluminum alloys are employed for lattices as well, such as

Al12Si and aluminum 7075: AlSi10Mg has been selected because it is the most used material at *Konstruktiver Leichtbau und Bauweisen* (KLuB, TU Darmstadt) for the manufacturing of lattices. Though this thesis is only considering numerical simulations, future project on the way of this one, might one day be considering experimental tests; in this way, there is the possibility for data to be compared.

Moreover, literature is rich with sources for AlSi10Mg properties, necessary for FEA. The next table lists the material properties (and the relative references) that have been used for the simulations.

Loading	Direction	Young's modulus [GPa]	Yield Strength [MPa]	Ultimate strength [MPa]	Elongation at break [%]	Ref.
Tensile	/	77±5	268±2	333±15	1,4±0,3	[37]
Compressive		/	317±2	714±1 (25% strain)	/	
Tensile	Z	74,38	270,01	446,28	8,09	[38]
Tensile	Z	69,4	209	315	7,3	[39]
Tensile	Z	77,6	204	358	7,2	[40]
Tensile	XY/Z	68±3	around 200	391±6/ 396±8	5,55±0,4/ 3,47±0,6	[41]
Tensile	Z	76±4	322±10	460±7	6.94±0.85	[42]

Table 7: material properties selected for the definition of AlSi10Mg for simulations.

Also, properties from [43] are considered. Taking account of the data showed, the modulus and the Poisson Ratio (and G as a result) used for the linear model are:

- E = 75 GPa;
- ν = 0,33 (from [44]);
- G = 28,195 GPa;

While for the bilinear model following values will be used:

- $\sigma_U = 400\ MPa$;
- $\sigma_Y = 250 MPa$;
- $\varepsilon_U = 0{,}07$;
- $\varepsilon_Y = \sigma_Y / E = 0{,}00333$;
- $E_T = \frac{\sigma_U - \sigma_Y}{\varepsilon_U - \varepsilon_Y} = 2250\ MPa$;

Where E_T is evaluated as the tangent modulus, and ε_Y is estimated via yield stress and linear modulus; it has not been imposed as 0,002 since this value is not considering the springback. Density considered is equal to 0,00268 g/mm^3. Figure 39 shows the stress-strain diagram obtained for the bilinear model.

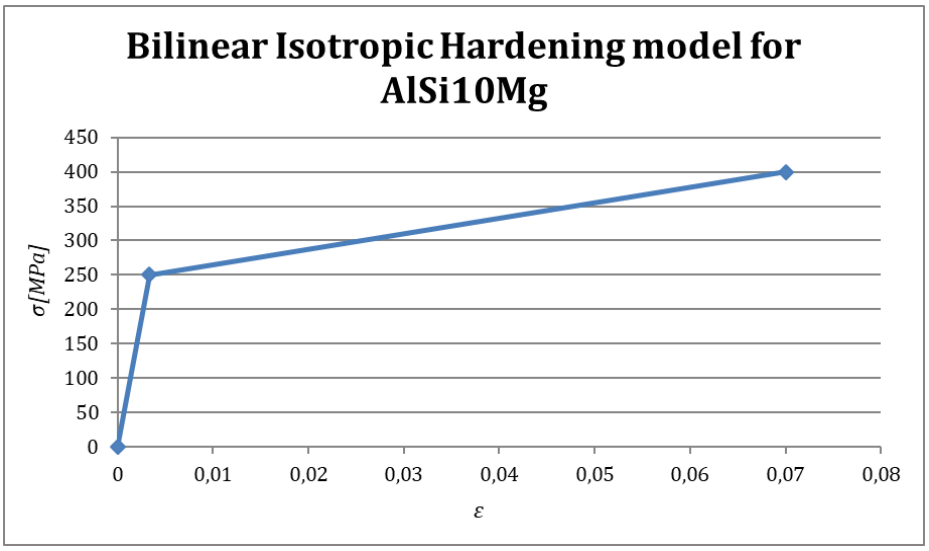

Figure 39: stress-strain diagram for the bilinear model.

2.2.2 Geometry

Lattice topologies are basically made of nodes and struts. Most of the simulations are made over a single RVE (linear, bilinear and homogenization tests), while only explicit dynamics simulations are made on a multi-cell sample. In this chapter, the general way of creating the cell geometry for a single RVE is going to be described: once the single RVE is generated, it is easy to create a sample.

Since the FEM software employed is *Ansys Workbench*, *Design Modeler* is the tool used for geometries. Every cell considered in this investigation presents more than three symmetry planes, and that makes the geometry generation process way easier: only 1/8 of the cell is created and then mirrored on three orthogonal planes, or rotated around the three orthogonal axes, to generate the whole RVE. Single struts are extruded and excess material is than deleted via slicing.

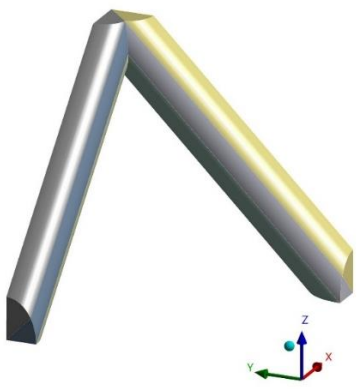

Figure 40: 1/8 of the *fcc* cell.

It is actually possible to start from 1/16 of the cell. Every strut has to be sliced in the strut axis direction into a number of slices that depends on the fact that every slice must present two extreme surfaces (not necessarily parallel): that has to be done for the sake of the mesh (see next subchapter). Figure 41 shows what has been obtained up to now for the *fcc* cell (as an example).

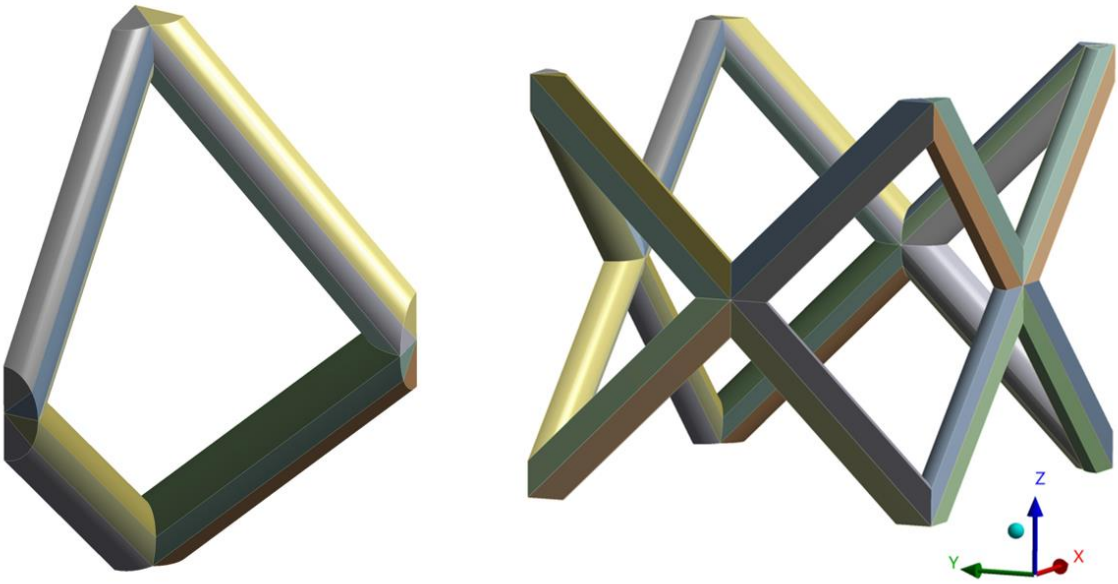

Figure 41: ¼ of the cell and the final cell, respectively after the second and third mirroring action (*fcc*).

Finally, after the last two mirroring (or rotations), the final cell is generated. In order to achieve automatic mesh equivalence, all generated solids must be gathered into a single "Part". The pictures just show results for the *fcc* cell, but the process is identical for every cell.

Since this investigation tends to focus on topology differences rather than RVE size, aspect ratio or material, RVE edge length and strut diameter are set respectively to 3 mm and 370 μm (that are most recommended sizes at *KLuB*)

2.2.3 Boundary conditions

When operating with RVE, boundary conditions are extremely important. Sensitivity analyses and part of linear analyses have been performed over ¼ of the RVE, while for bilinear analyses the whole RVE has been modelled to ensure good results: in both cases symmetry conditions have been applied.

Symmetry conditions in Ansys Workbench consist of blocking the displacement in the normal direction of the surface where the condition has been applied together with rotations around the axes laying on the plane. For ¼ of the model these conditions are applied on the outer sides surfaces on the RVE side and on the ones laying on the middle plane of the RVE so that the presence of the rest

of the RVE is simulated. Figures 42 and 43 show the cited condition. When it comes to the full RVE modelled, symmetry conditions are applied on the outer sides surfaces as well, and that is sufficient for test where the displacement applied to simulate the loading is small, like linear and bilinear. The problem is present when big displacements are applied, that is the case of homogenization tests: in those situations, displacements normal to the surfaces laying on the middle planes of the RVE, that are XZ and YZ, needs to be locked, otherwise deformations linked to torsional buckling incur, offsetting results. Figures 44 and 45 show such conditions.

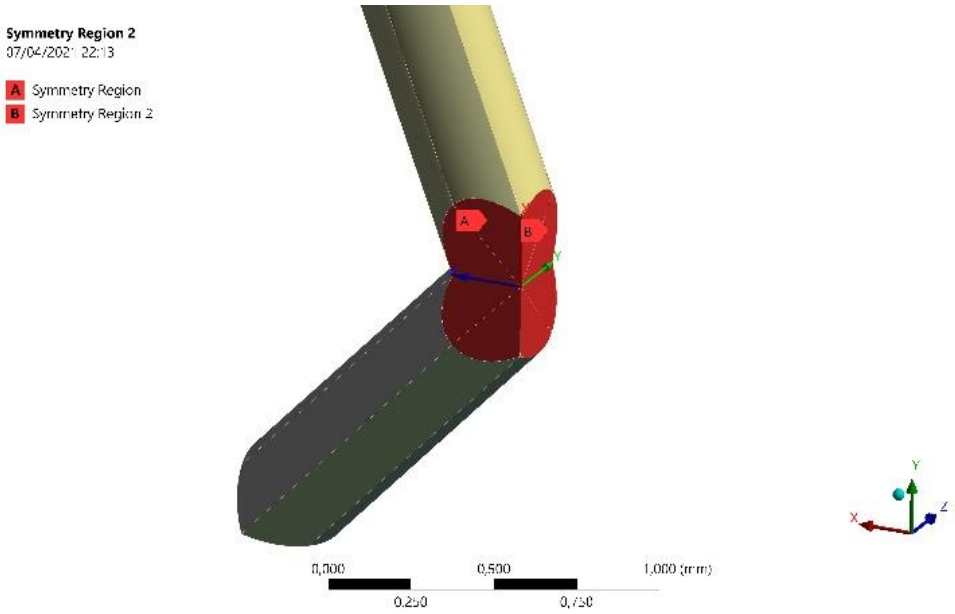

Figure 42: symmetry conditions applied on the surfaces laying on the middle planes of the RVE for ¼ RVE model (*bcc*).

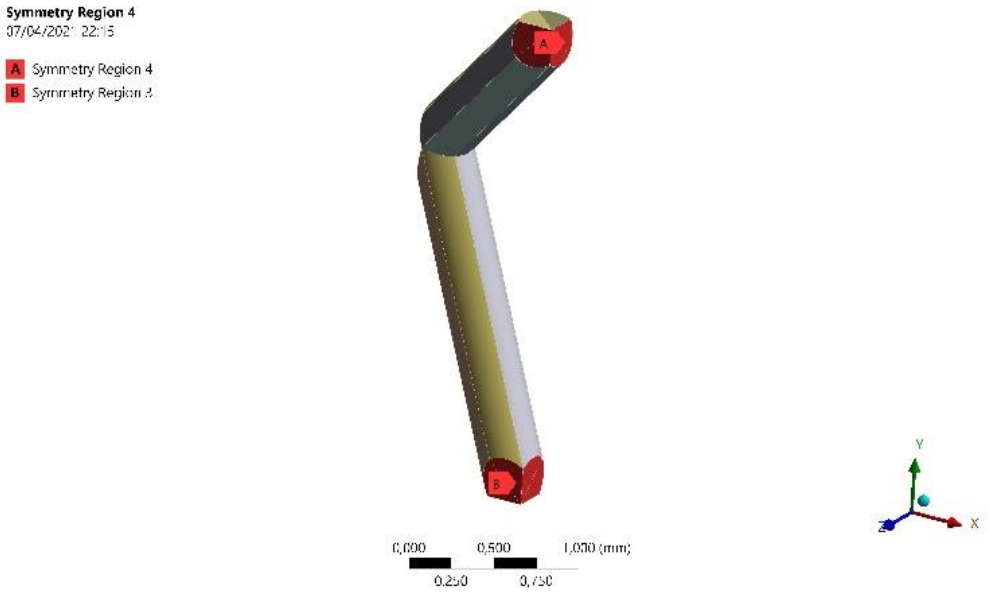

Figure 43: symmetry conditions applied on the outer sides surfaces for ¼ RVE model (*bcc*).

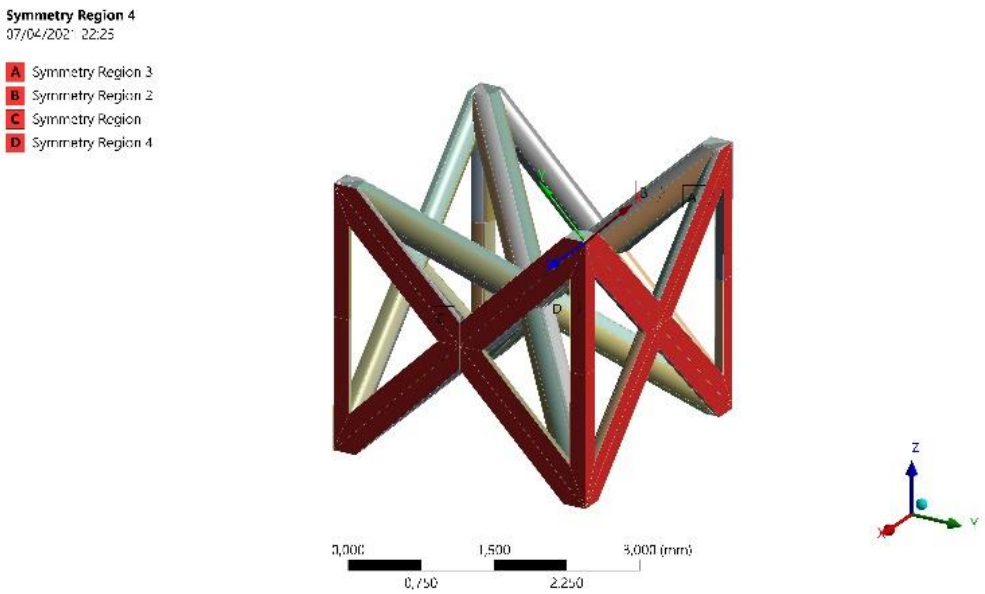

Figure 44: symmetry conditions applied on the outer sides surfaces for the full cell model (*fbccz*).

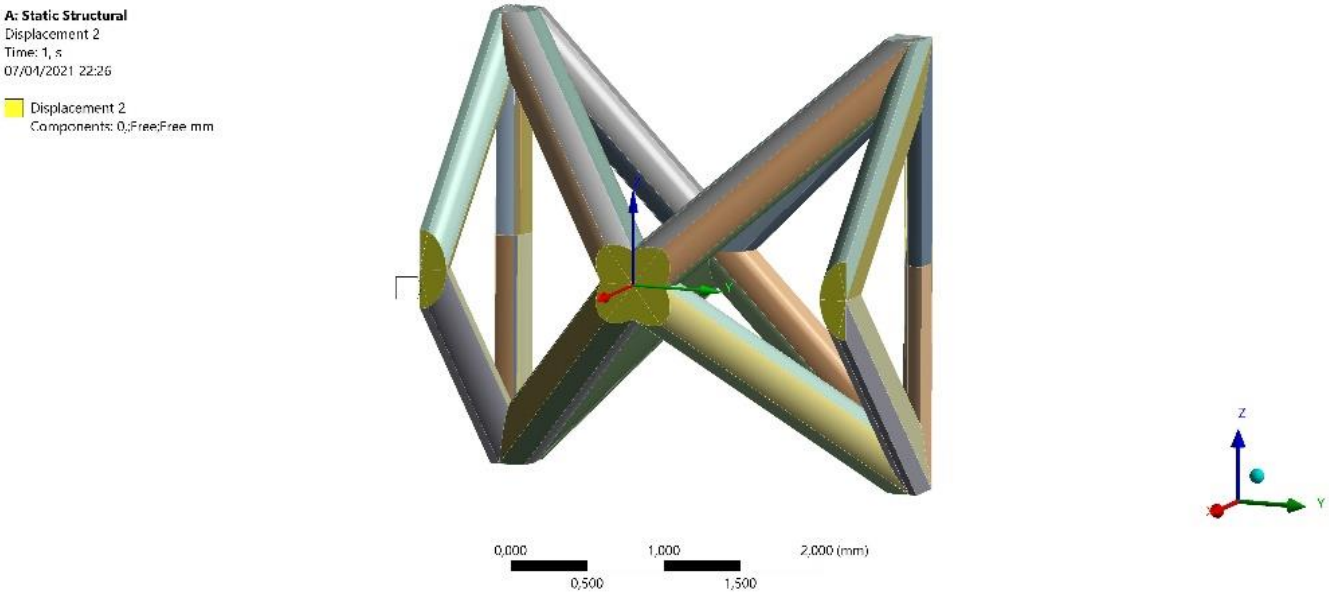

Figure 45: normal displacement locked on the showed surfaces to avoid torsional buckling (*fbccz*).

When boundary conditions differ from the one described in this chapter, it will be specified. These reported here are the most general and used ones.

2.2.4 Mesh

As previously said, the section of the single strut has been sliced into a certain number of sectors: in this way a better mesh is possible, especially with the Ansys Workbench meshing tool. The chosen method for the meshing process is called “Multizone” and it basically consists of a sweeping mesh for more complex solids, quite efficient for slices with the section of a circular sector, but no parallel extreme faces. Hexa and prism (where needed) elements have always been used, tria elements were

abandoned in order to achieve a good quality, especially for the explicit dynamics simulations. Starting simulations were made on ¼ of RVE with addition of symmetry condition and in order to achieve symmetric mesh, the Match Control tool has been used as a guarantee. Though there was no actual need for that since the mesh (with a certain consequentiality in the solids to select for meshing) is always symmetrical.

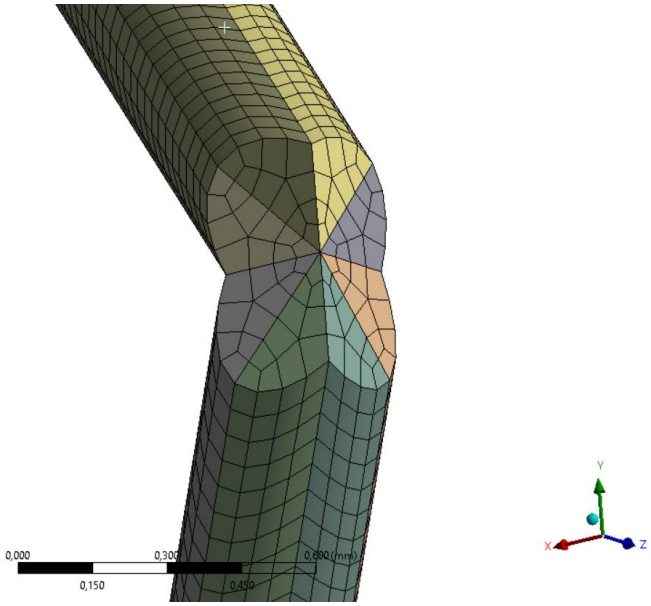

Figure 46: mesh example on ¼ *bcc* cell.

Once the meshing algorithm that offers the best quality has been established, two sensitivity analysis have been performed since the second one tried to correct some problems of the first one.

The first sensitivity analysis takes place on a geometry resulting from the creation of bodies using rotation tools, that is ¼ of the *bcc* cell plus symmetry boundary conditions. It can be said that the meshing algorithm considers how the final geometry is created: there are in fact small differences between the mesh for bodies coming from rotation and the one for bodies coming from mirroring, as it will be shown. The simulation consists of the lower surface of the RVE fixed, while a -0,01mm displacement is imposed on the upper surface in the normal direction; bilinear material model is used here and with the displacement imposed, the yielding point is not surpassed.

Stresses are registered on three main points in the model: the first point is in the exact middle of the cell, the second is on the top of the middle side of the upper strut and the third is at the middle point of intersection edge of upper and lower strut (see figure 47). Also mesh quality factors such as minimum corner nodes Jacobian Ratio, maximum skewness and maximum aspect ratio are checked, since, because of the complex geometry, many elements risk high distortion that might result into bad

results. These parameters are registered and tabled for different mesh sizes going from 0,2 mm to 0,02 mm with a 0,01 mm range. Results can be found in table 8.

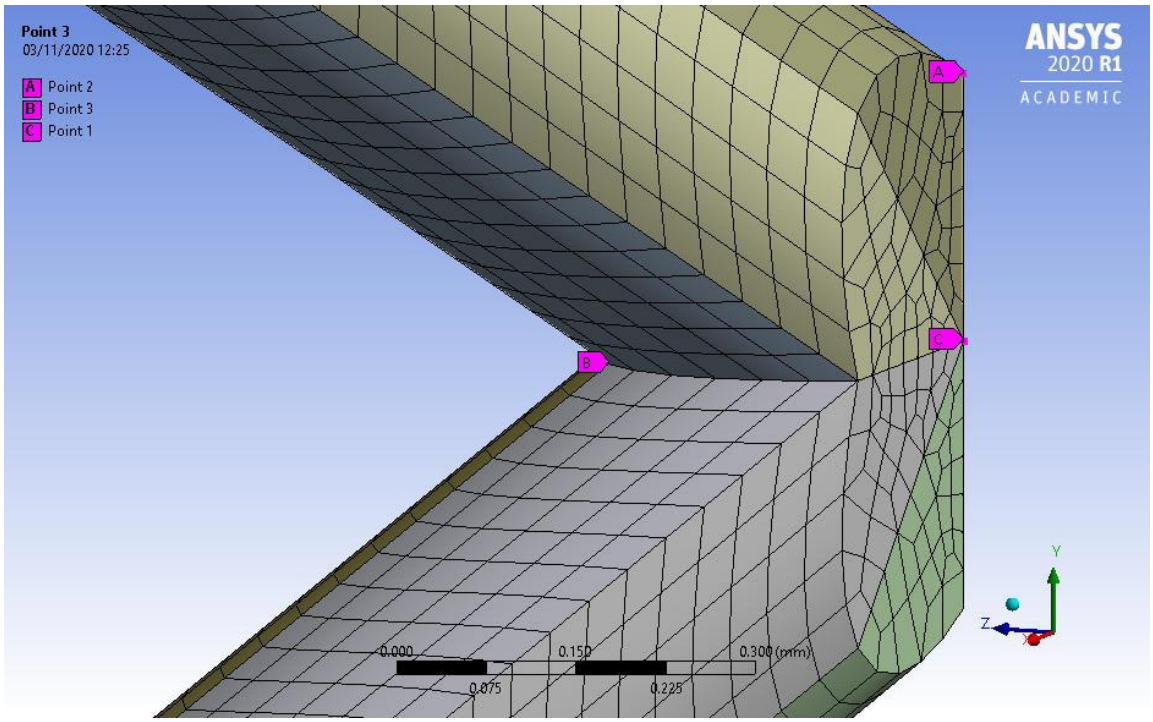

Figure 47: points used for the stress registration in the sensitivity analysis.

Element size [mm]	Stress pt.1 [MPa]	Stress pt.2 [Mpa]	Stress pt.3 [MPa]	Min Jacobian (corner nodes)	Max Skewness	Max Aspect
0,2	51,907	33,784	147,01	0,35658	0,6178	5,1547
0,19	52,702	32,85	148,06	0,35651	0,6178	4,7872
0,18	53,304	31,928	149,03	0,35644	0,61784	4,4685
0,17	53,749	31,013	149,91	0,35638	0,61784	4,1897
0,16	54,072	30,105	150,7	0,35631	0,61784	3,9435
0,15	54,299	29,204	151,43	0,35625	0,61784	3,7247
0,14	54,45	28,31	152,08	0,35619	0,61784	3,5289
0,13	54,543	27,424	152,67	0,35613	0,61784	3,3526
0,12	54,472	66,299	140,78	0,23373	0,75132	5,7719
0,11	54,628	65,533	141,48	0,23368	0,75132	5,2909
0,1	54,554	28,621	162,53	0,29997	0,72613	4,2278
0,09	54,615	27,581	164,01	0,29987	0,72613	3,7906
0,08	54,893	28,186	167,7	0,23681	0,76418	4,1475
0,07	61,984	51,834	163,17	0,32662	0,76457	3,5151
0,06	57,185	48,188	169,16	0,21809	0,79731	4,5174
0,05	65,041	60,295	177,41	0,31141	0,79447	3,7685
0,04	83,872	61,722	201,07	0,26814	0,78161	3,2837
0,03	94,061	11,551	202,23	0,28169	0,7628	3,6753
0,02	/	/	/	0,27305	0,76501	3,5655

Table 8: data from first sensitivity analysis (“/” means the analysis could not be performed because of the limited number of nodes available).

For a better understanding of the results, data are also graphed; see figures 48 and 49.

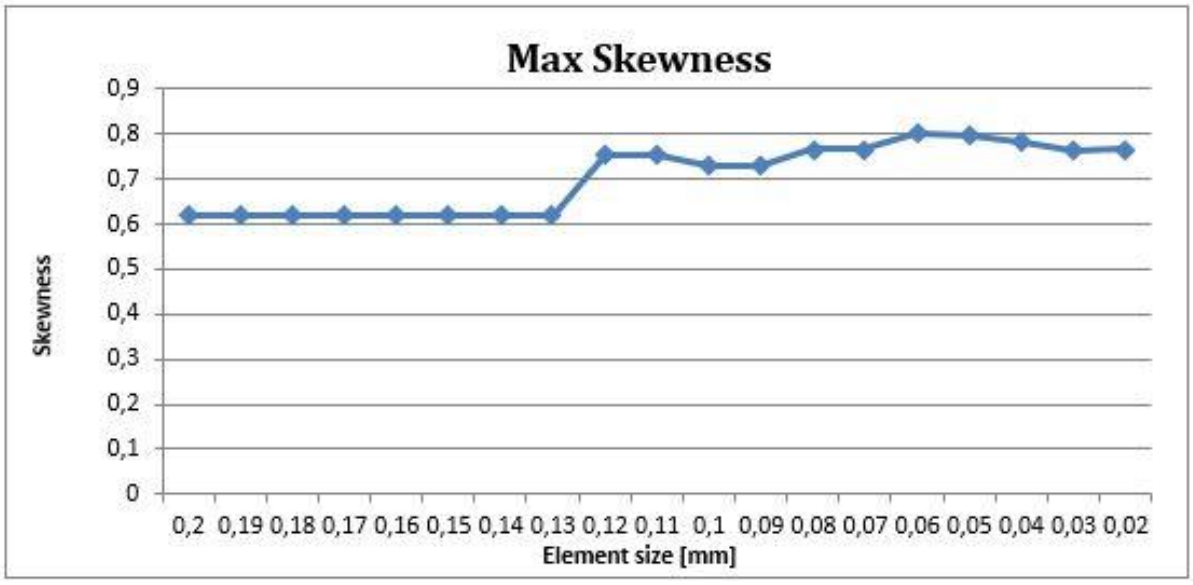

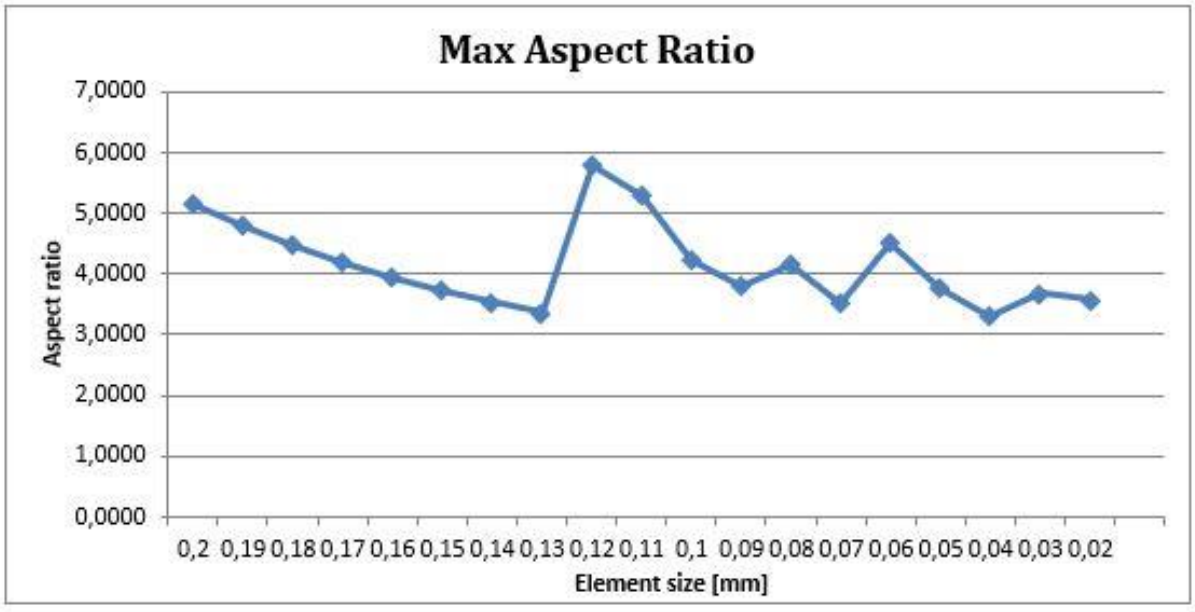

Figure 48: minimum corner nodes Jacobian ratio, maximum skewness and maximum aspect ratio over element size for the first sensitivity analysis.

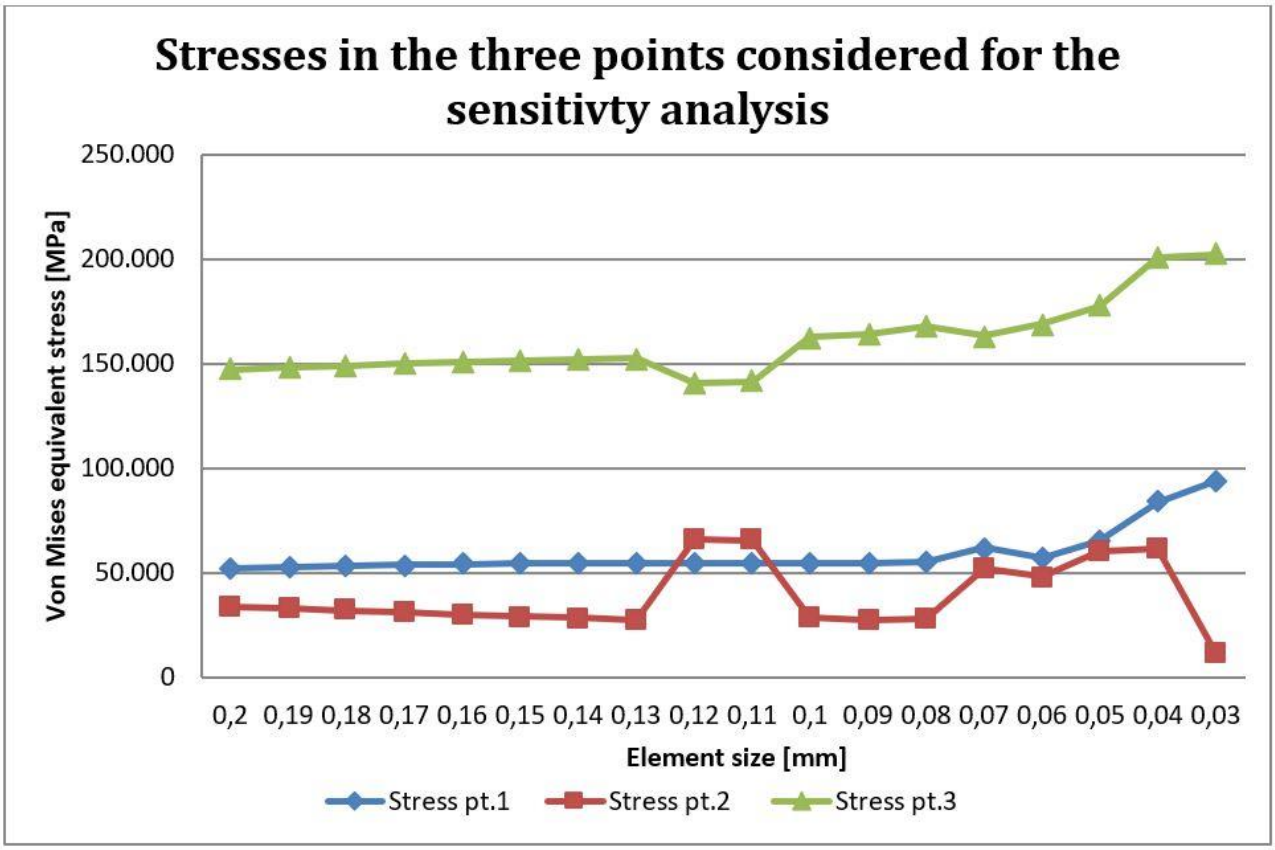

Figure 49: Von Mises equivalent stress for the three points over element size for the first sensitivity analysis.

Looking at the results, especially in the stress field, we can see that from a particular point (element size equal to 0,12 mm) there are peaks that suggest the solution is not converging: this is due to the change in the mapped mesh of the faces of the struts. This is unfortunately not under control; in fact, not even sizing edges was useful at all. Also, the quality mesh parameters from that point on start oscillating, but they are still all acceptable (the most important one, the Jacobian Ratio, still is always positive). A good size might be the one right before the second oscillation in the stress of the first point, that is element size equal to 0,08 mm: the mesh at this point is quite similar to the one in figure 47 (where the element size is 0,1 mm), but it is finer in the direction of the struts.

By the way, thinking the problem might be hiding in the topology and the geometry of the model, a second sensitivity analysis has been performed: this time the struts are all shaped using the mirror tool and not the rotational one; also, the single sector of a strut is totally shaped before the "assembly" of a whole strut. In this way, the final geometry consists of the symmetrical repetition of a single body. Imposition of symmetry regions and match control was not a problem at all, while in the first attempt many problems showed up because of the imprecision on the topology (due to the rotation of the geometry and not the mirroring). Stresses are measured in the same positions as before; they are just a little bit higher in general since in the previous analysis the results were given just a moment

before the time of the deformation equal to 0,01 mm. Results are once again tabled and graphed (figures 50, 51 and table 9).

Element size [mm]	Stress pt.1 [MPa]	Stress pt.2 [Mpa]	Stress pt.3 [MPa]	Min Jacobian (corner nodes)	Max Skewness	Max Aspect
0,2	55,616	36,053	157,51	0,35658	0,61784	5,1547
0,19	56,468	35,055	158,64	0,35651	0,61784	4,7872
0,18	57,112	34,068	159,67	0,35644	0,61784	4,4685
0,17	57,59	33,09	160,62	0,35638	0,61784	4,1897
0,16	57,936	32,118	161,47	0,35631	0,61784	3,9435
0,15	58,179	31,153	161,25	0,35625	0,61784	3,7247
0,14	58,341	30,196	162,95	0,35619	0,61784	3,5289
0,13	58,441	29,247	163,58	0,35613	0,61784	3,3526
0,12	58,534	36,816	151,13	0,30455	0,72397	5,7719
0,11	58,44	36,018	151,88	0,30459	0,72397	5,2908
0,1	58,453	30,667	174,17	0,29997	0,72525	4,2278
0,09	58,519	29,553	175,75	0,29987	0,72525	3,7906
0,08	58,816	30,2	179,68	0,23681	0,76375	4,1474
0,07	60,189	55,526	174,59	0,32662	0,76457	3,5158
0,06	59,645	51,806	181,15	0,21807	0,79931	4,5157
0,05	59,626	58,243	189,84	0,31314	0,79447	3,7685
0,04	59,898	67,387	215,56	0,26854	0,78161	3,2811
0,03	59,672	80,804	216,58	0,28169	0,7628	3,6753
0,02	/	/	/	0,27305	0,76501	3,5631

Table 9: data from second sensitivity analysis ("/" means the analysis could not be performed because of the limited number of nodes available).

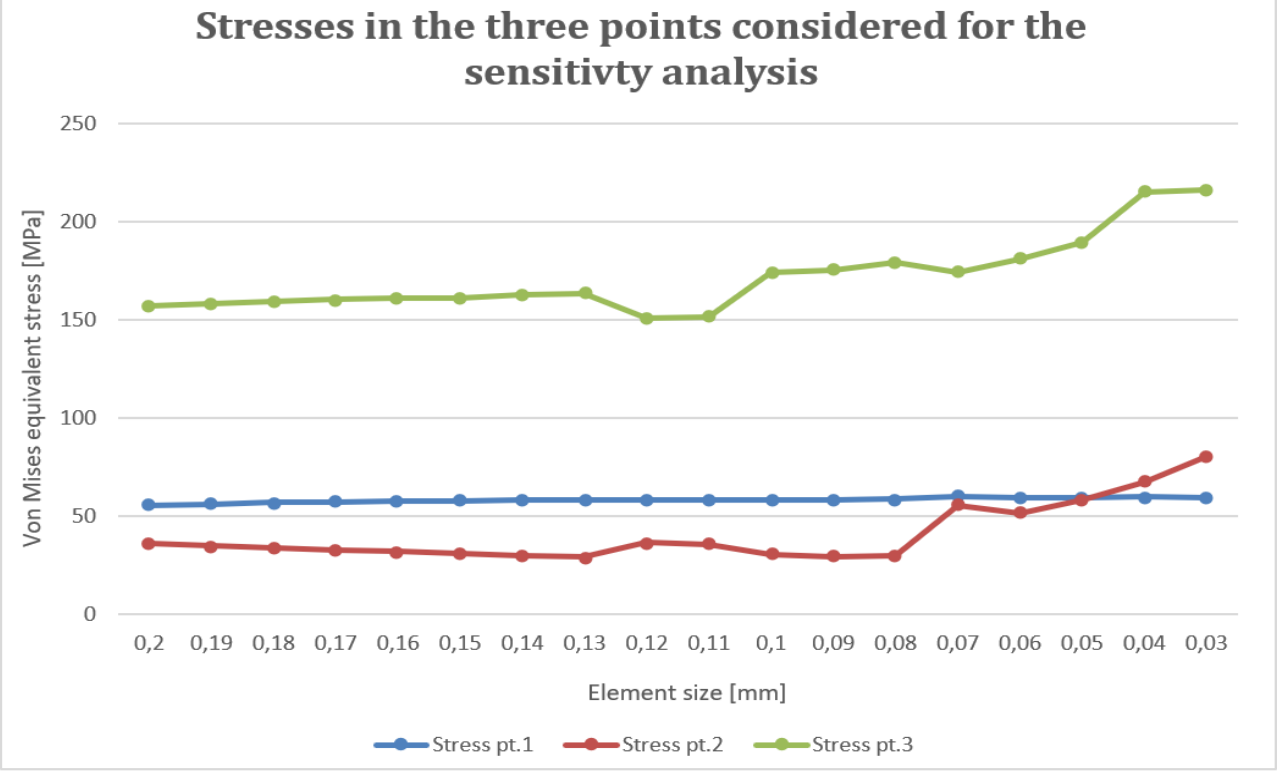

Figure 50: von mises equivalent stress for the three points over element size for the second sensitivity analysis.

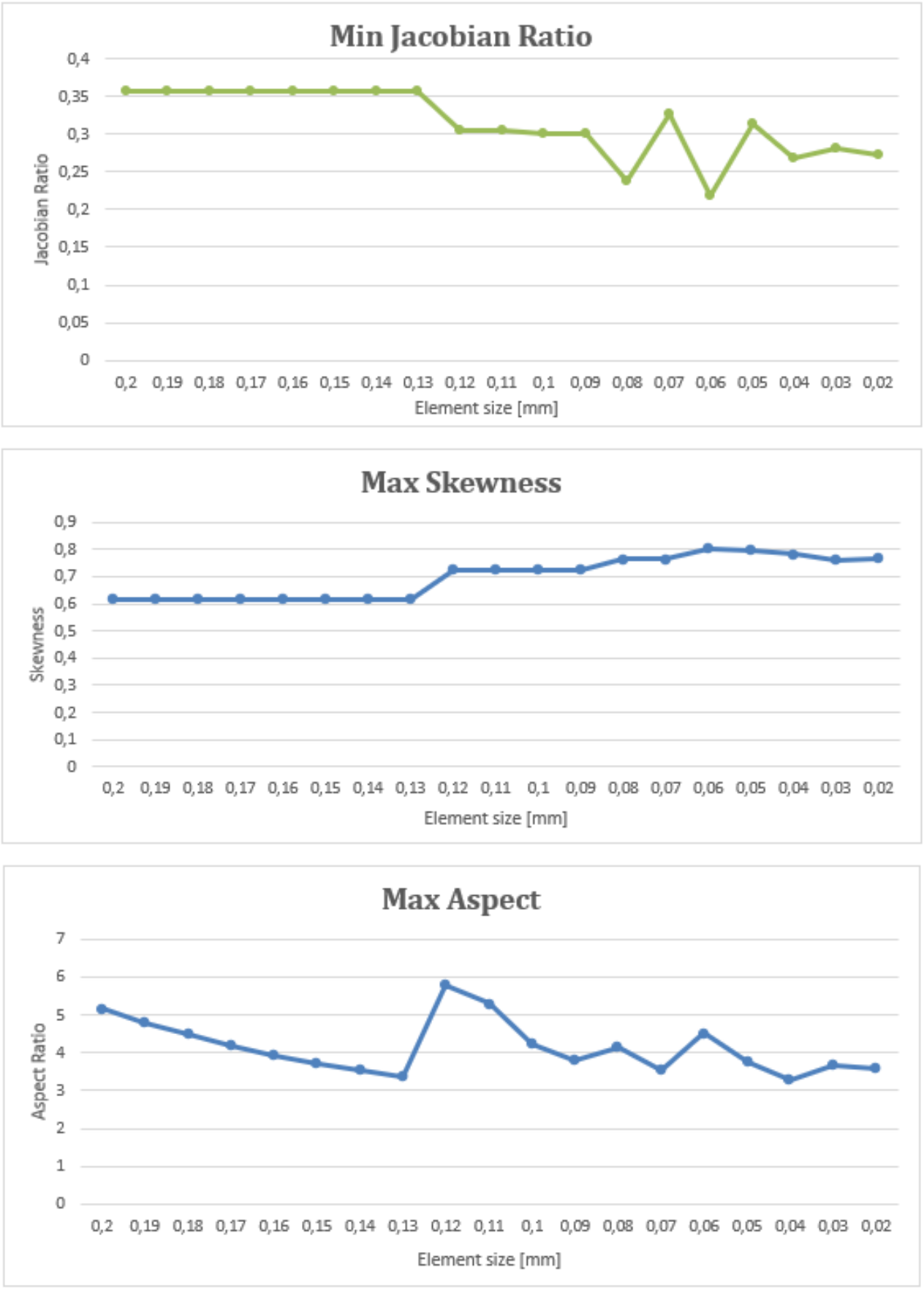

Figure 51: minimum corner nodes Jacobian ratio, maximum skewness and maximum aspect ratio over element size for the second sensitivity analysis.

Trends among the quality mesh factor are almost the same as the previous analysis, exception made for some slightly better values among the aspect ratio. What is important is the decreasing of the oscillations in the stresses, though they are still present. Stress in point number two shows a strong inversion after element size equal to 0,08 mm (not considering the first inversion, that is much more inhibited than the second one), while stress in point one and three seems to have their own trends respected almost everywhere. Because results are acceptable up to size 0,08 mm (also quality indices are far better up to that point) and because, after that size, oscillation in both stresses in point 2 and 3 start peaking or having high variations, element size 0,08 will be used as standard size.

By the way, being geometries very different from each other, little variations from 0,08 mm are possible especially for more complex cells (such as *fbccz*); in such cases, mesh quality is always checked before solving. Variations also depend on the maximum number of nodes available for the teaching license of Ansys, that is 256000 nodes. For explicit dynamics analysis, where a sample will be modeled, elements size will need a slight increase. With the experience of the second sensitivity analysis, mirroring solids is used as the standard process for geometry generation.

3 Linear and bilinear static simulations

Before starting with crashing simulations, that are an essential part of this investigation, the focus is now on Statics. As previously said, this study wants in fact to explore the possibility of anticipating dynamic properties with static ones. Moreover, linear and bilinear tests have been useful to appreciate the main differences between the selected cells.

3.1 Linear simulations

3.1.1 Model

First of all, the material model just makes use of E and ν for the definition of the properties. These tests are performed over ¼ cell, with symmetry conditions and mesh defined as in chapter 2. As a constrain, lower surface is fixed, while on upper surface a -0,01 mm displacement is imposed in the load direction. In static analyses the fixed surface is simulating a fixed plate, while the displacement is used as a crushing plate; contacts are not contemplated in static analyses. The displacement is defined trying not to exceed the local yield stress (250 MPa), beyond which a linear test would make no sense; also, here degrees of freedom of the upper surfaces in the horizontal direction are imposed to 0 mm, simulating a high enough friction force that would not allow the relative movements between upper plate and the sample. Figure 52 shows these boundary conditions.

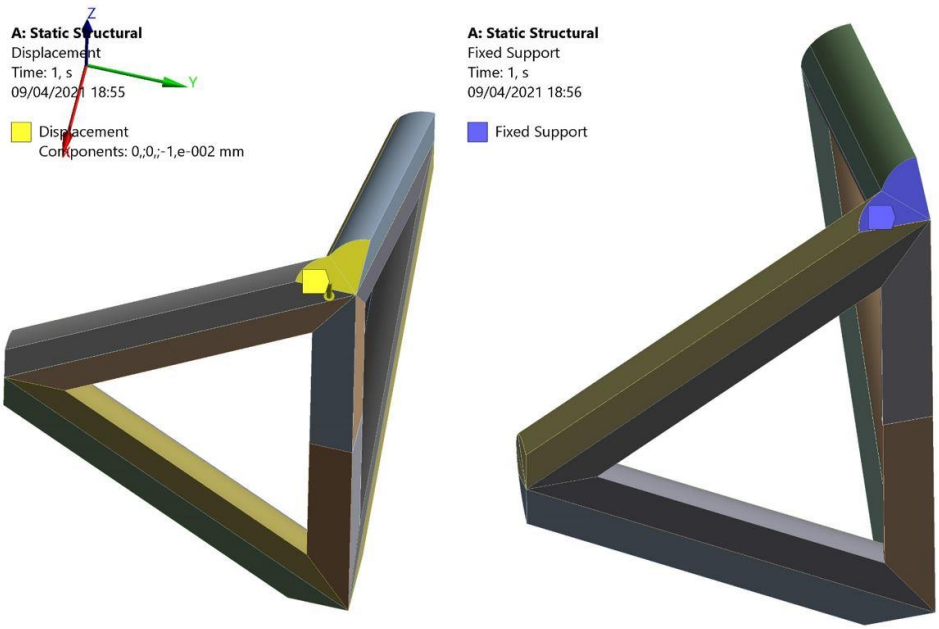

Figure 52: displacement imposed on upper surfaces (left) and fixed lower surfaces (right) (*fccz*).

The local yield stress limit is unfortunately not always respectable, but in order to achieve the same testing method performed over all the cells selected, the displacement imposed must be the same for all of them: that is essential for sake of comparison between cells performances. This will result into an overestimated evaluation of the energy absorption, but for starting tests it is not that relevant: simulations with bilinear material model will surely give back more accurate results.

3.1.2 Results

The main output requested to Ansys is force reaction F_Z, that is the one registered on displaced surfaced. Using F_Z it is possible to calculate specific energy absorption SEA and volumetric energy absorption VEA (that presents the same trend as EA, being the RVE volume the same for every cell). Using force and RVE section area (9 mm^2), as well as displacement and RVE edge length, it is possible to evaluate engineering stress and strain: these will be much more useful in the future though. Relative density is calculated via the effective volume the cell occupies, that is obtained directly from *Design Modeler*. Results are showed in Table 10.

		BCC	*BCCZ*	*FCC*	*FCCZ*	*FBCC*	*FBCCZ*
Effective Volume	mm^3	1,987	2,246	1,627	1,872	3,414	3,658
Relative Density $\bar{\rho}$	/	0,0736	0,0832	0,0602	0,0693	0,1264	0,1355
Mass	g	5,324E-03	6,019E-03	4,359E-03	5,017E-03	9,149E-03	9,803E-03
Force Reaction Z	N	25,09	55,26	43,50	70,70	70,38	98,44
Engineering Stress	Mpa	2,79	6,14	4,83	7,86	7,82	10,94
Engineering Strain	$\mu\varepsilon$	3333,333	3333,333	3333,333	3333,333	3333,333	3333,333
EA	mJ	0,251	0,553	0,435	0,707	0,704	0,984
SEA	mJ/g	47,12	91,81	99,79	140,93	76,93	100,42
VEA	mJ/mm^3	9,291E-03	2,047E-02	1,611E-02	2,619E-02	2,607E-02	3,646E-02
Density	g/mm^3	1,972E-04	2,229E-04	1,615E-04	1,858E-04	3,388E-04	3,631E-04

Table 10: results from linear static analyses.

For a better representation of the results, they are graphed as well using bar diagrams: those are shown in figures 53-57. Because the model for these analyses consists of ¼ of the cell, force reaction is multiplied by four, and consequentially EA parameters as well.

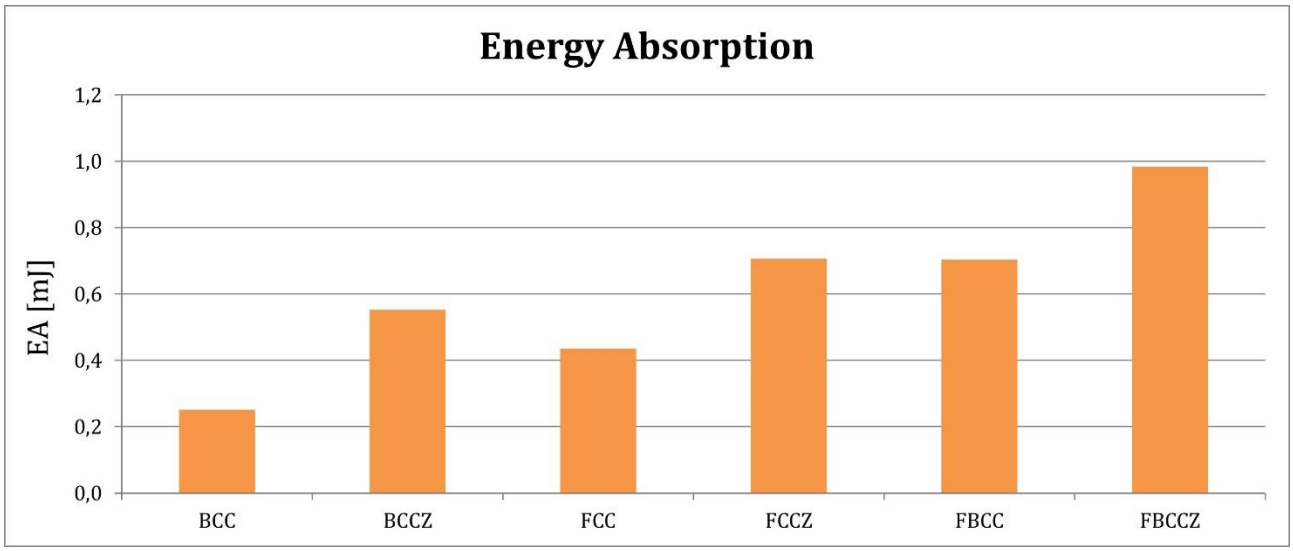

Figure 53: Energy Absorption levels for Linear Static simulations.

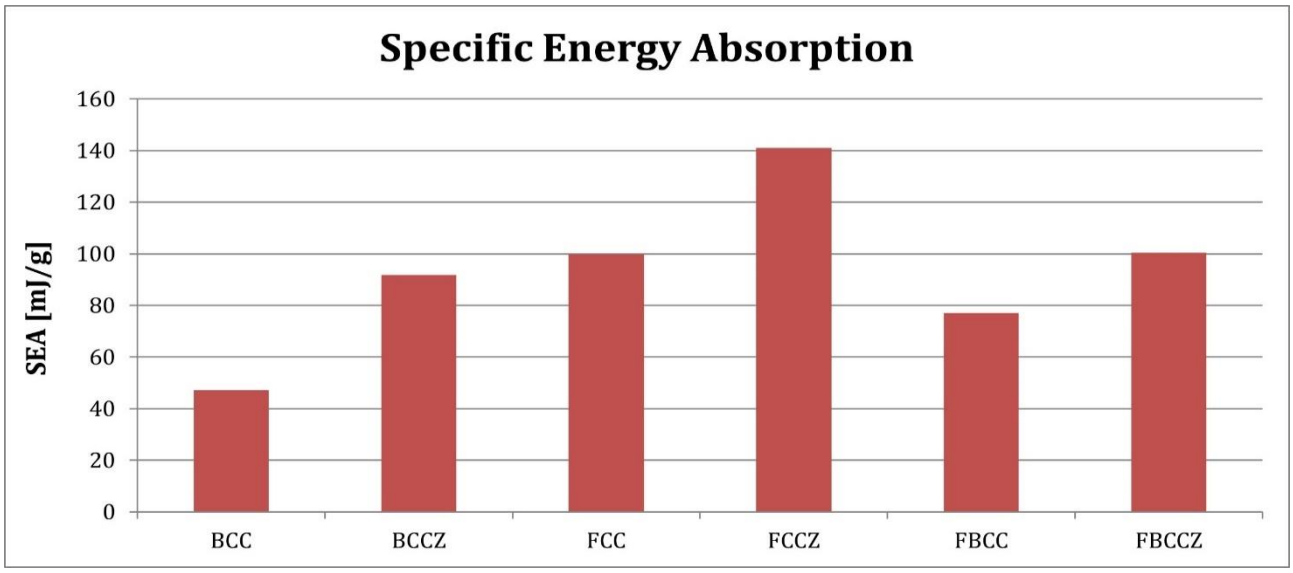

Figure 54: Specific Energy Absorption levels for Linear Static simulations.

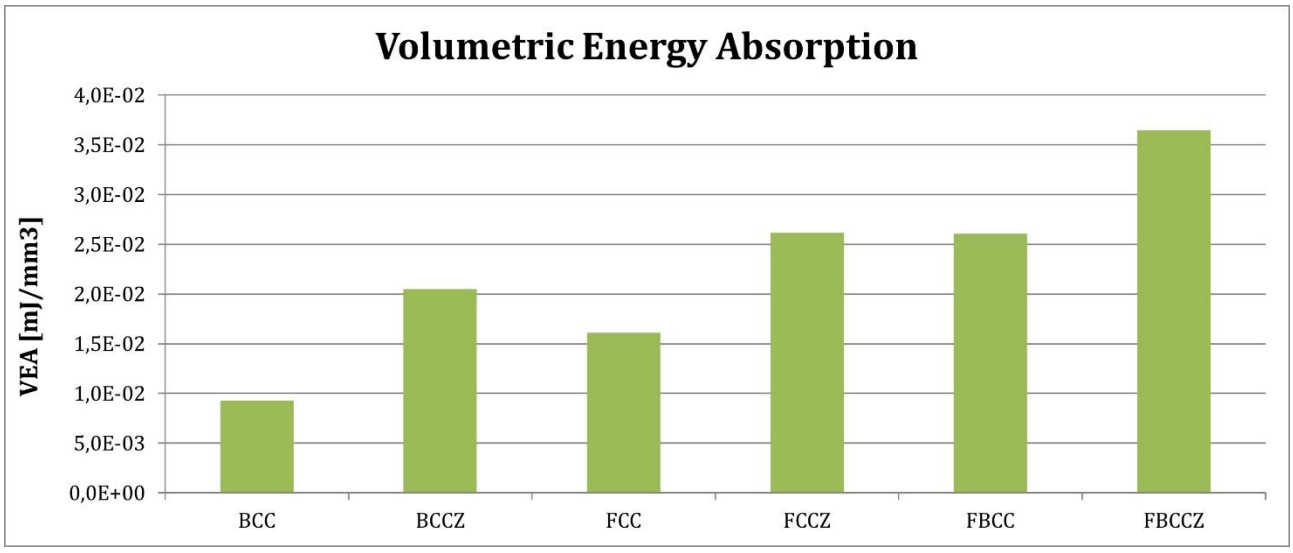

Figure 55: Volumetric Energy Absorption levels for Linear Static simulations.

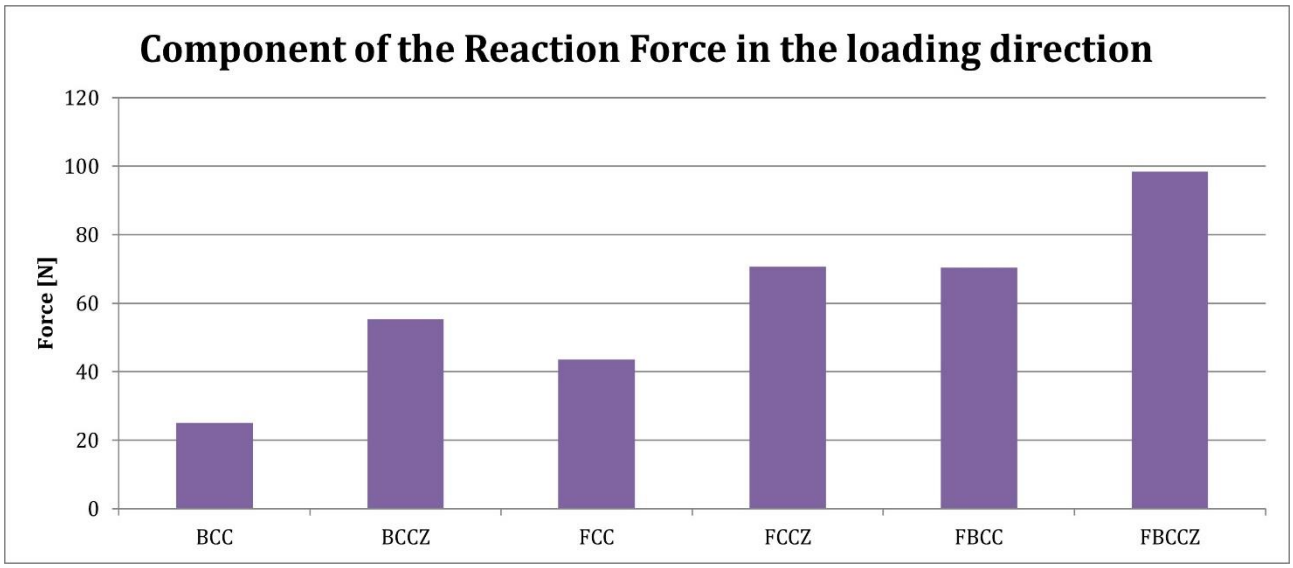

Figure 56: Component of the reaction force in the loading direction for Linear Static Simulations.

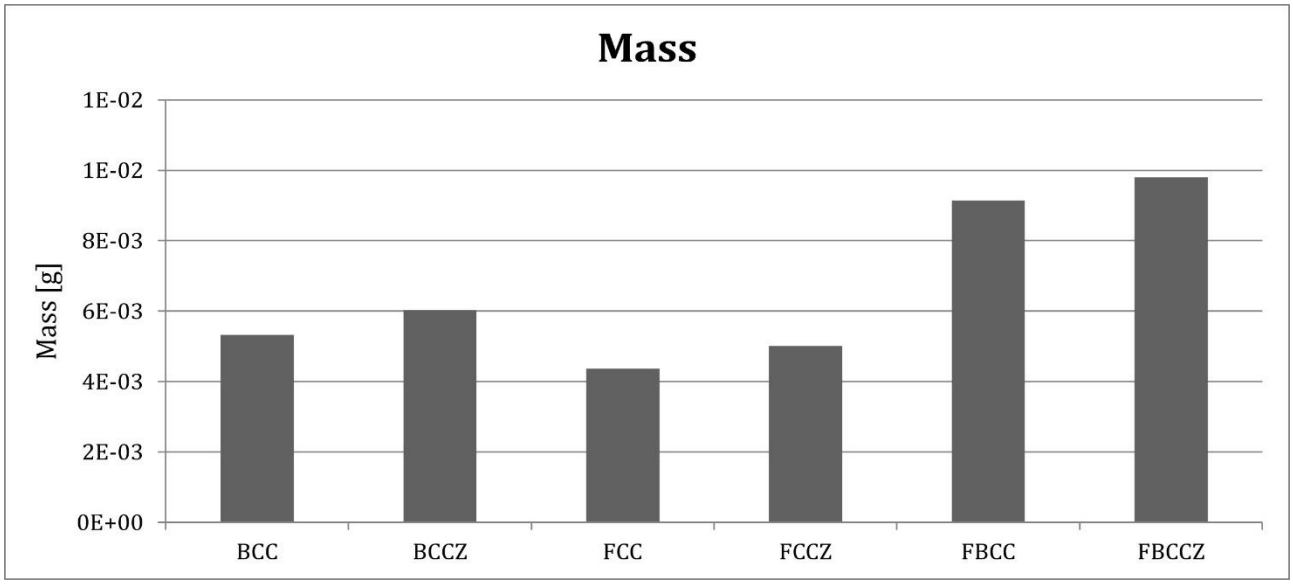

Figure 57: Mass of the cell considered for the analyses.

3.1.3 Discussion

Looking at relative densities $\bar{\rho}$ and masses for the different cell types, without considering that the addition of vertical struts obviously increases those properties of a similar amount every time, it is evident that the lightest among the analyzed ones is the *fcc*. At the same time, it stands in a middle position when it comes to energy absorption. Since the considered volume is the same one for every cell, VEA follows the exact same trend as EA, but the situation is quite different for the relationship between EA and mass or $\bar{\rho}$: the mass effect makes the *fcc* the best cell for SEA. Also, evaluating SEA with mass or relative density gives back the same results in terms of trend, since both are depending on the effective lattice volume.

Another important factor is the force reaction in the loading direction. It is expected that a higher force reaction in static simulations will results into a higher peak stress in dynamic ones, and that is usually no good for the efficiency of the crash; that is by the way something that need to be validated with future analyses, because force reaction will be of course linked with plateau stress as well. Force also follows the trend of the EA, being this value calculated with force and displacement.
The impact of vertical struts is quite clear from results: the increase of every measured and evaluated property is evident when Z struts are involved. The most important results in this sense are achieved in the jumps going from *fcc* to *fccz* and from *bcc* to *bccz*. Effects on *fbcc* are slightly less relevant: the justification to this behavior may be hidden in the fact that the addition of vertical struts to a cell with a high number of oriented struts is less influent than the same addition to a cell with minor number of struts. That would basically explain the similar EA level of *fccz* and *fbcc*.
For the moment, the one that can be considered as the "best cell" seems to be *fccz*, if we adopt the SEA parameter as the motor of this decision. Not so many comments can be made if analyses are limited to the linear static field though; also, for sure some overestimations have been done: bilinear static simulation will of course give us some more accurate answers.

3.2 Bilinear simulations

Model used for these simulations is basically the same as the previous one. There are only two differences: first, the displacement imposed for every cell is 0,02 mm instead of 0,01mm; second the model material is bilinear and not linear. The motivation for the first change is the fact that in order to appreciate results that are coherent with a bilinear model, stress field needs to go beyond the yield point at least in the critical point. Properties of the bilinear model material can be found in chapter 2.

3.2.1 Results

Results are presented in the same way as the previous subchapter. They can be found in Table 11.

		BCC	BCCZ	FCC	FCCZ	FBCC	FBCCZ
Effective volume	mm^3	1,987	2,246	1,627	1,872	3,414	3,658
Relative density	/	7,358E-02	8,318E-02	6,025E-02	6,933E-02	1,264E-01	1,355E-01
Mass	g	5,324E-03	6,019E-03	4,359E-03	5,017E-03	9,149E-03	9,803E-03
Force Reaction Z	N	49,20	77,40	74,06	99,53	122,67	148,25
Engineering stress	MPa	5,47	8,60	8,23	11,06	13,63	16,47
Engineering strain	$\mu\varepsilon$	6666,667	6666,667	6666,667	6666,667	6666,667	6666,667
EA	mJ	0,984	1,548	1,481	1,991	2,453	2,965
SEA	mJ/g	184,80	257,19	339,79	396,82	268,16	302,48
VEA	mJ/mm^3	3,644E-02	5,734E-02	5,486E-02	7,373E-02	9,087E-02	1,098E-01

Table 11: results from bilinear static analyses.

Graphs are also obtained from these data: they are showed in figures 58-61.

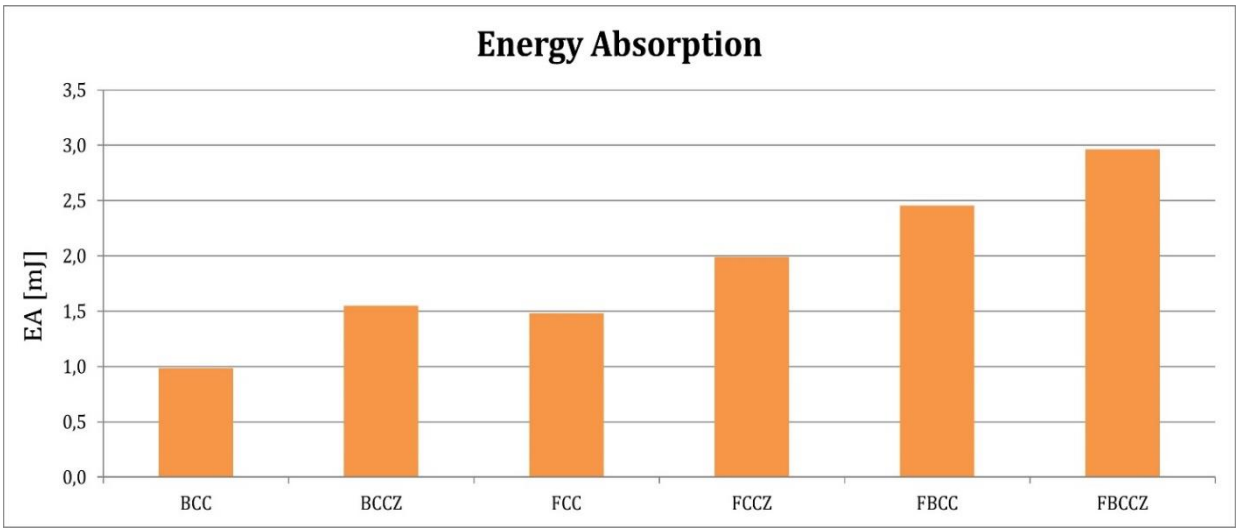

Figure 58: Energy Absorption levels for Bilinear Static simulations.

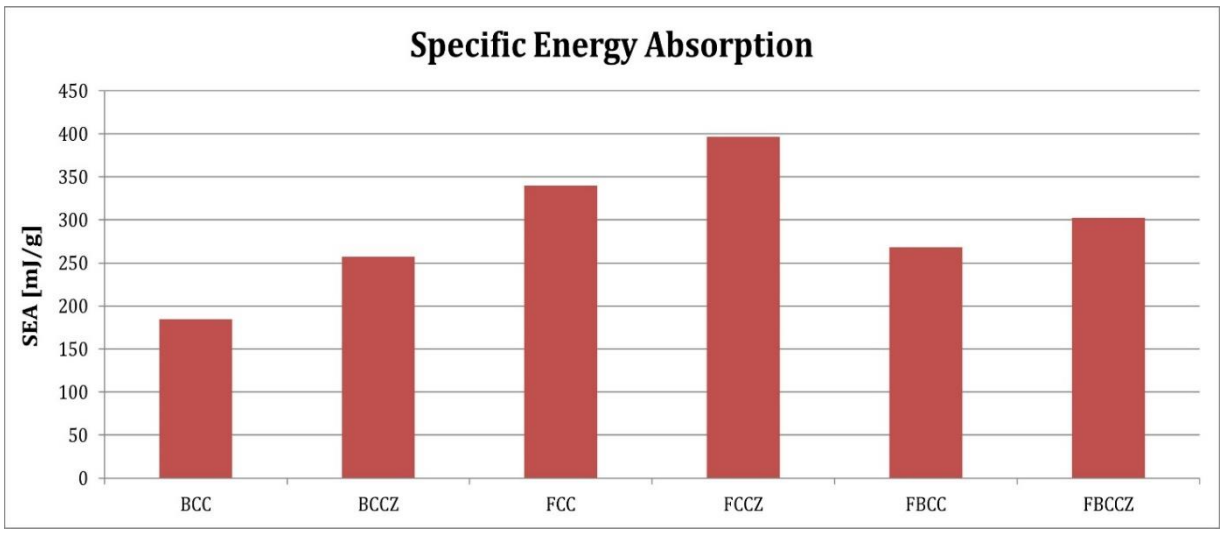

Figure 59: Specific Energy Absorption levels for Bilinear Static simulations.

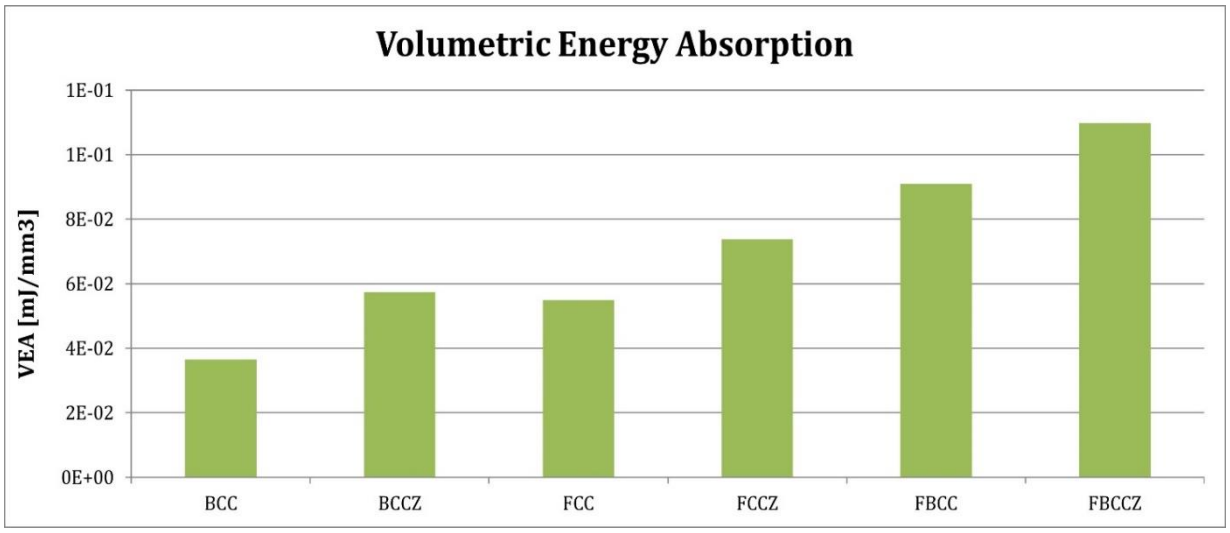

Figure 60: Volumetric Energy Absorption levels for Bilinear Static simulations.

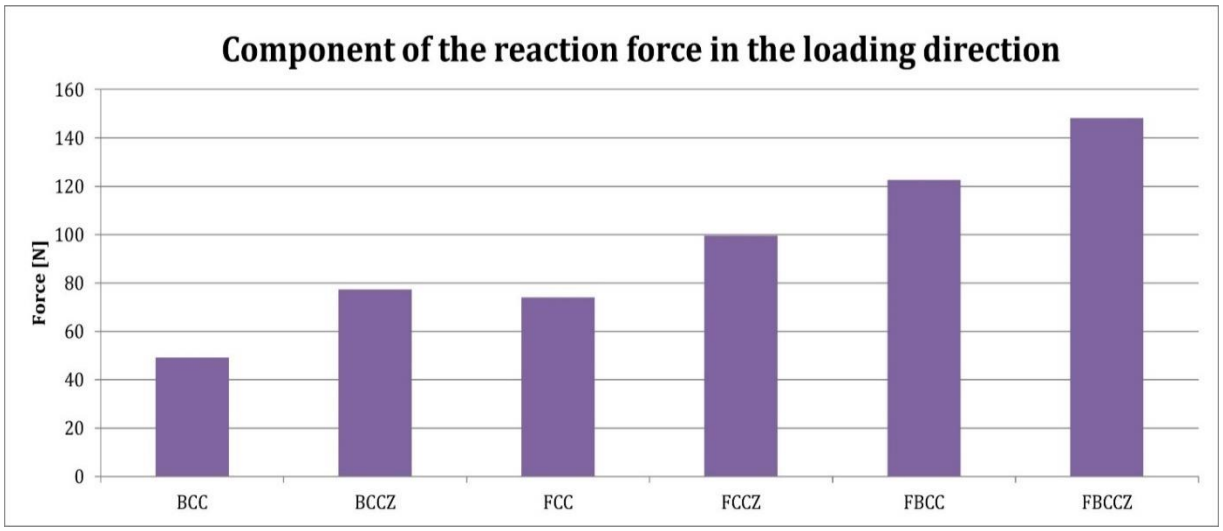

Figure 61: Component of the reaction force in the loading direction for Bilinear Static Simulations.

3.2.2 Discussion

There are few differences between the two models. The trend for EA and force reaction are very similar to the ones from the linear model: the main difference is in the *fbcc* surpassing the *fccz*. This shows the higher energy absorption capacity of the *fbcc* plastic field. A consideration can be done also in the sense of struts orientation: *fbcc* presents oriented struts instead of vertical ones, as in *fccz*, and their presence influences in a good way force reaction and therefore EA. Displacement imposed of course results into better results, but still is limited: homogenization process developed in chapter 5 will tell us more about plastic fields of the cells involved.

Moving to SEA: trend is basically the same as the previous model. The main dissimilarity lies in the differences between reinforced and non-reinforced cells, as well between *bcc*, *fcc* and *fbcc*. This might be a sign of the overestimations made in the linear model, but also when it comes to SEA, it is evident how *bcc* (and *bccz*) has been subject to an underestimation, at least with regards to other cells. *fccz* seems once again to be the most convenient choice when a compromise between energy absorption and weight has to be done. In general, considering pure EA and force reaction, the best candidate is *fbccz*. It is proven therefore that vertical struts are highly convenient for EA from statics point of view so far: explicit dynamics will give more information about that.

Explicit dynamics tests moreover will indirectly consider buckling effect for vertical struts: in fact, that is something these analyses are not contemplating. Symmetry conditions applied do not allow horizontal displacements that are what makes buckling possible. That is unfortunately a deficit in this way of modeling RVEs, and that is also why BCs have been reconsidered for high-speed crashing analyses (as it will be explained in chapter 4).

3.2.3 Local stresses analysis

For a better understanding of the lattice behavior, a brief local stresses analysis is carried out. Besides being helpful in this sense, it is a proof of the fact the yield stress has been surpassed. This analysis is performed over *fbccz* only: this cell contains in fact all of the strut types present in the other cells, that are *bcc*-like struts, *fcc*-like struts, and vertical struts. Stress behaviors are basically the same among struts type.

At this point Von Mises equivalent stress and strain are registered at the inner intersection point, as it is possible to see in figure 62.

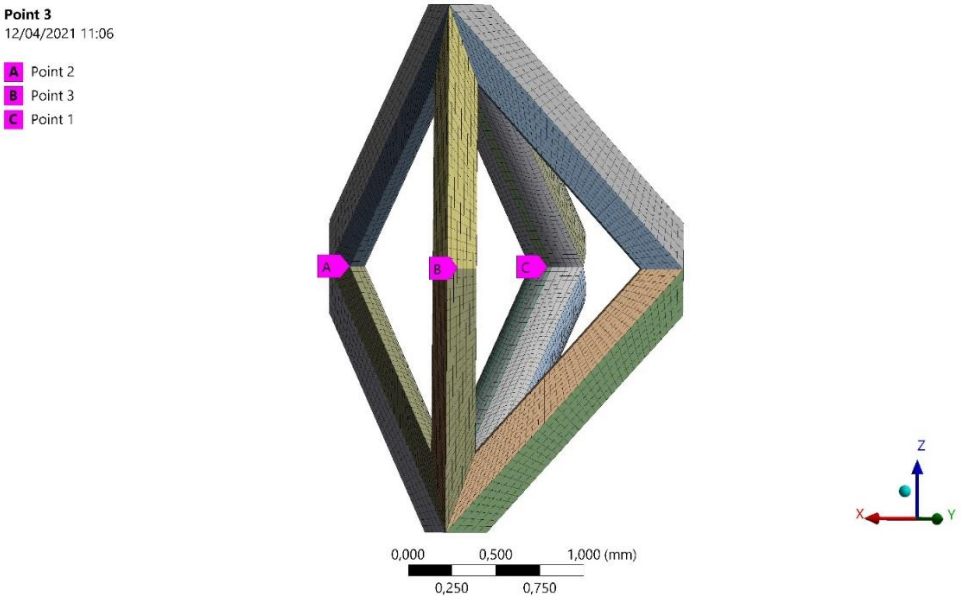

Figure 62: points where Von Mises equivalent stress and strain have been registered.

Following stress-strain diagrams (figures 63-65) are obtained:

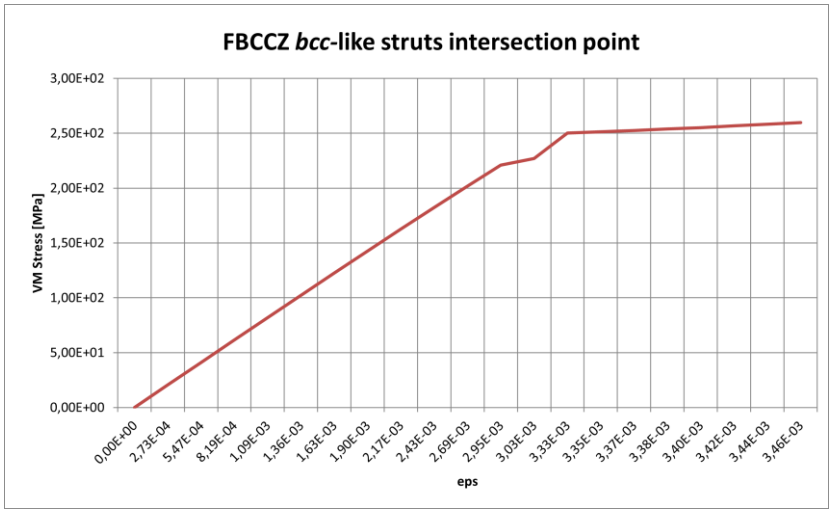

Figure 63: Von Mises stress-strain diagram for the *bcc*-like struts intersection point (C in figure 62).

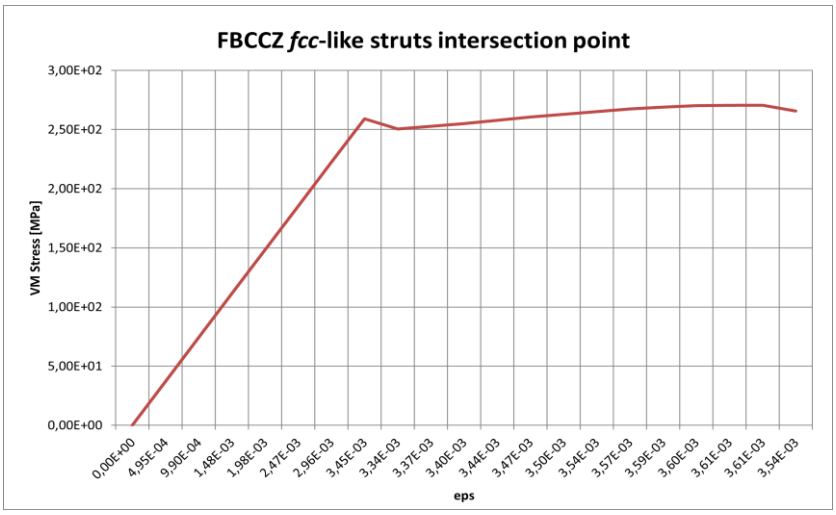

Figure 64: Von Mises stress-strain diagram for the *fcc*-like struts intersection point (A in figure 62).

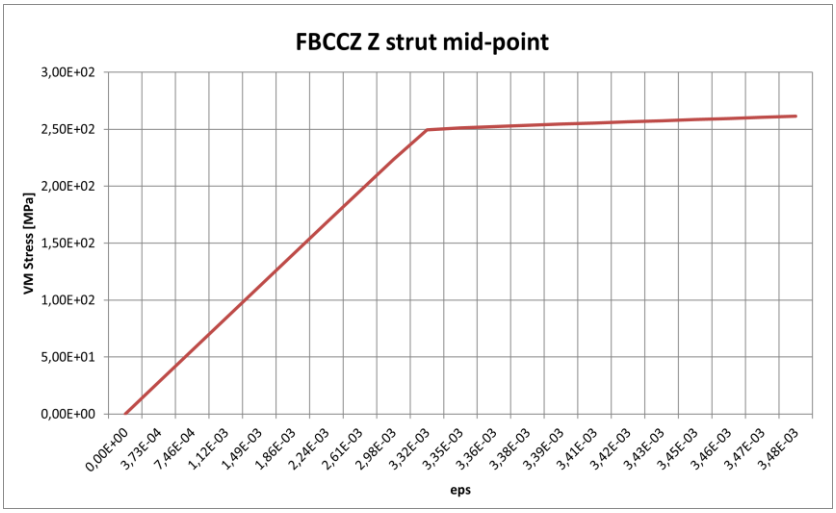

Figure 65: Von Mises stress-strain diagram for the Z struts intersection point (B in figure 62).

It is evident how yielding is always surpassed in these three critical points. It has to be stated that by the way that happens for three different combinations of stress-strain: that is due to the nature of the Von Mises stress that is actually a function of three different stress-strain fields. The Z strut diagram, being the stress field in the Z direction the most important one, almost retraces the bilinear model material diagram.

Another proof of the fact that the simulation has gone beyond yield point can be found in the estimation of failure indices. Stress used for the evaluation is max shear, that in Ansys Workbench means using the Tresca failure criterion, used for ductile materials. Ratios are calculated both with Yield and Ultimate stress. Figures 66 and 67 show fringes obtained.

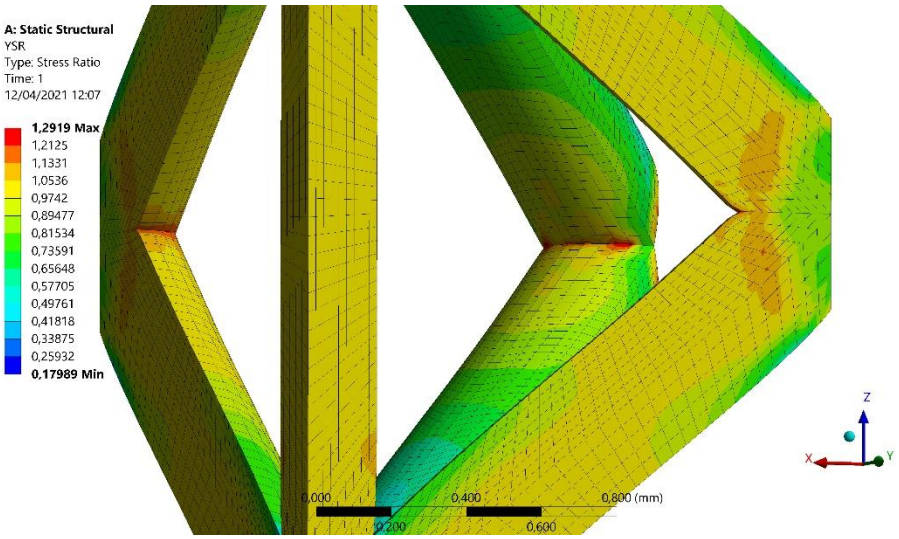

Figure 66: Max Shear over Yield Stress ratio fringe.

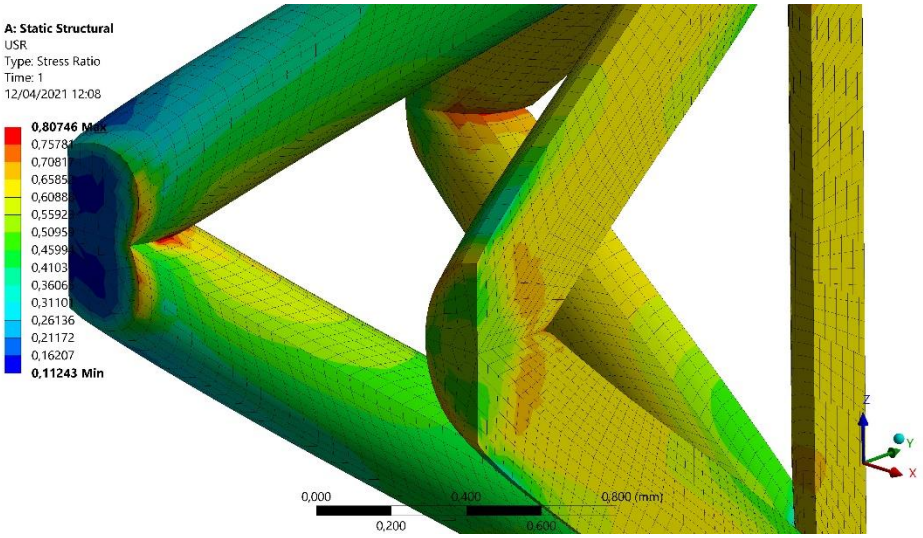

Figure 67: Max Shear over Ultimate Stress ratio fringe.

Yield point is then surpassed in many zones of the model; at the same time, ultimate is never reached. Also, fringes are slightly deviated because of load effects at the top and bottom of the model.

4 High speed crashing simulations

Now that first results from static compression analyses are collected, it is time to understand the high-speed crashing behavior of selected lattices. In order to do so, it has been necessary to use explicit dynamics analysis. It has been preferred to transient structural for the following reason: when it comes to phenomenon lasting more than 1 second, it is suggested to use transient structural, since it is like considering a sequence of quasi-static cases; while for simulations lasting less than 1 second, explicit dynamics is better since solvers used it these cases are able to catch stress shockwave (not our case) and evolution of stress and strain in high strain rate situations (high non-linearities). It is in fact commonly used for ballistic and impact tests, high speed crashing and in general high non-linear simulations. Moreover, it is far more accurate than implicit codes, and because of that it is highly time consuming.

Two models have been developed for these simulations: the first model presents problems with convergence especially for samples with vertical struts reinforcements. Second model was able to achieve better and more meaningful results.

4.1 First simulations set

At the beginning, the test was supposed to be carried out for a 3x3x3 cells sample; that was unfortunately impossible because of the nodes limit. The choice to apply symmetry conditions has therefore been made in order to reduce the model to an adequate number of nodes. ¼ of the model is generated, as it is possible to see in figure 68.

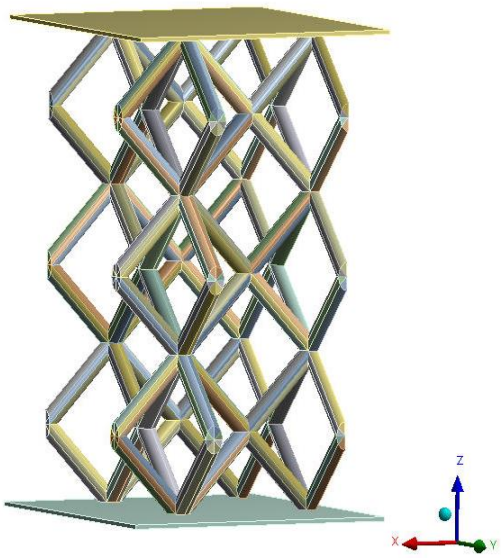

Figure 68: First model used (*fcc*).

Meshing basically follows rules defined in chapter 2. A fixed plate and a crashing plate are used respectively to hold still the sample and to apply the load (model is very similar to the one in [45] and [46]). Frictionless contact analysis is contemplated in order to link plates to the sample; normally, contacts should be imposed also for regions of the struts which are supposed to touch each other during the simulation, but for a predefined Part this is already taken into account in the explicit dynamics solver code. Symmetry regions are applied to all of the outer side surfaces. Two of the four sides are meant to be inner symmetry regions (to simulate the presence of the rest of the sample), while the two remaining are meant to be outer symmetry planes (as if the sample is part of a bigger structure); figure 69 represents these regions.

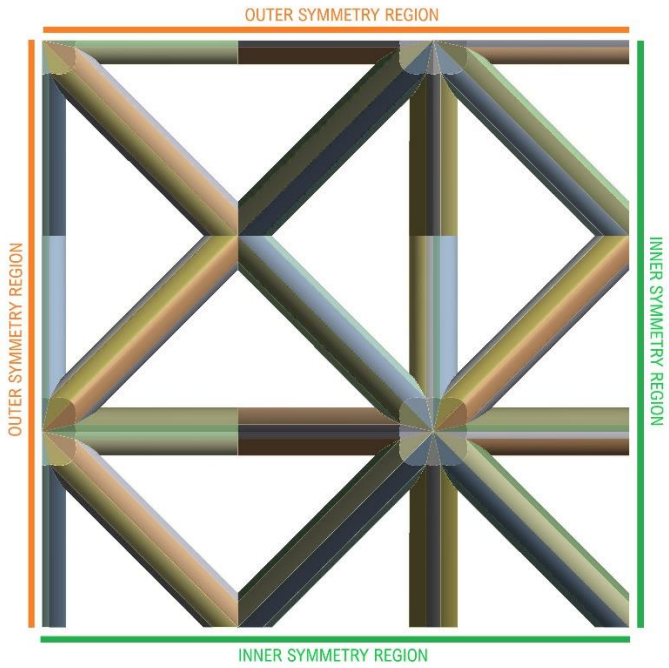

Figure 69: top view of the sample (*fbcc*).

Speed of the crashing plate is defined as 200 m/s (as the one used in [32], typical for such cases). 50% crashing is the maximum that can be obtained before incurring into errors due to convergence. Force is registered on the crashing plate, later transformed into engineering stress using section area, while engineering strain is obtained via vertical displacement. First results are then available in figure 70.

From this graph, multi-peak behavior is evident and clearly defines the consequential collapse of each single row one after another: after the linear section of each diagram there is the first peak that is the highest (for every cell) and usually defines the peak stress used for the evaluation of the crashing load efficiency. Unfortunately, *fbcc* simulation did not make it until the end because of an energy error.

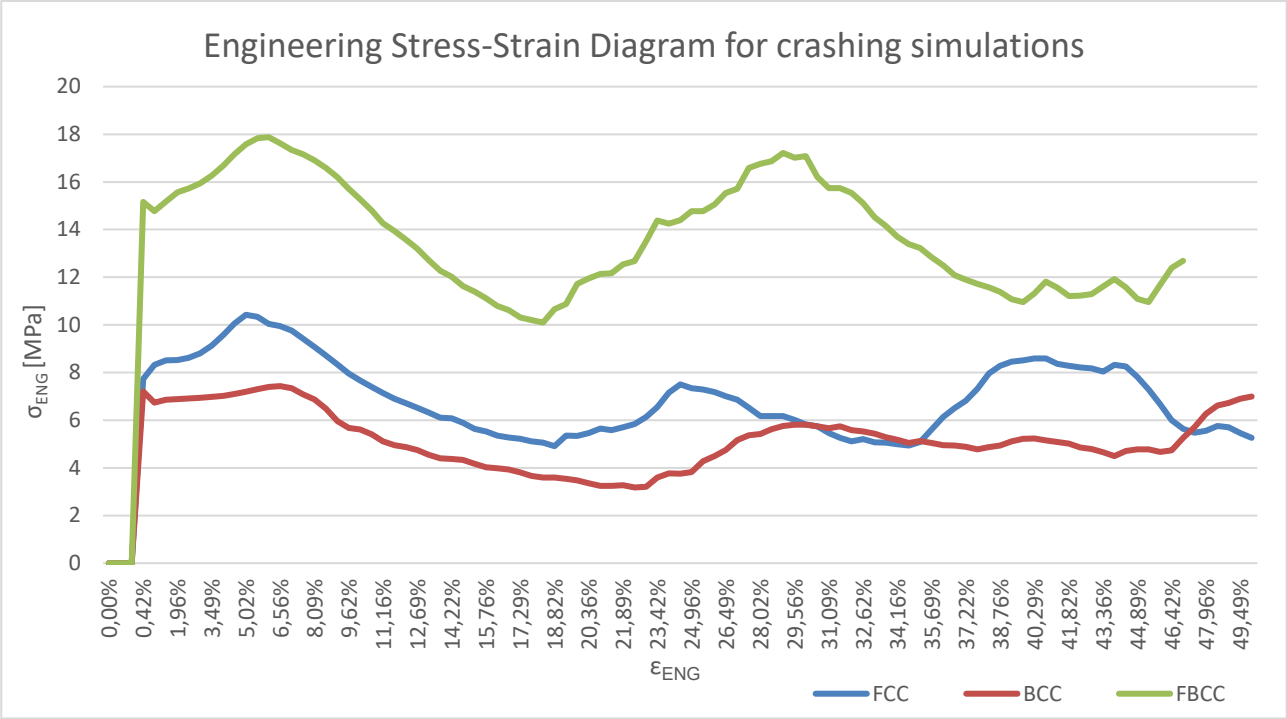

Figure 70: Stress-Strain diagrams for high speed crashing simulations with model 1.

Moreover, EA trend is quite clear from diagrams: *fbcc* is the best one, followed by *fcc* and *bcc*. Energy has not been analytically evaluated since these analyses showed severe problems. As it is possible to see, vertical reinforcements have not been considered: because of the strict boundary conditions that have been imposed, Z struts present problems with deformation in their natural way, that is buckling.

Though some positive responses of these simulations such as being able to catch general behavior of lattices under compression, and energy levels that seem to respect the ones from static analyses, there are too many problems: first of all, it is impossible to perform simulations with vertical struts because of the BCs imposed in order to reproduce symmetry conditions. Another problem (that is the one forcing the creation of a new model) is the loss of information at the border of the model: in fact, buckling is not the only phenomenon that has been lost at the border of the model. Because normal displacements and rotations have been locked on the outer surfaces of the model, of course nodes and elements are forced into those surfaces, resulting into what can be called a not true deformation path. Problem can also be seen from a graphical point of view in figure 71. A symmetric final deformation was expected, instead there is no symmetry in deformation at all because of instabilities going beyond the conditions imposed. These instabilities might be also due to the multi-row aspect of the sample. Another minor problem is as excessive hourglass effect that can be seen both in deformation, especially in the critical points of struts, and hourglass energy level (figures 72 and 73). Also considering convergence problems, probably due to these difficulties, solution time is extremely long.

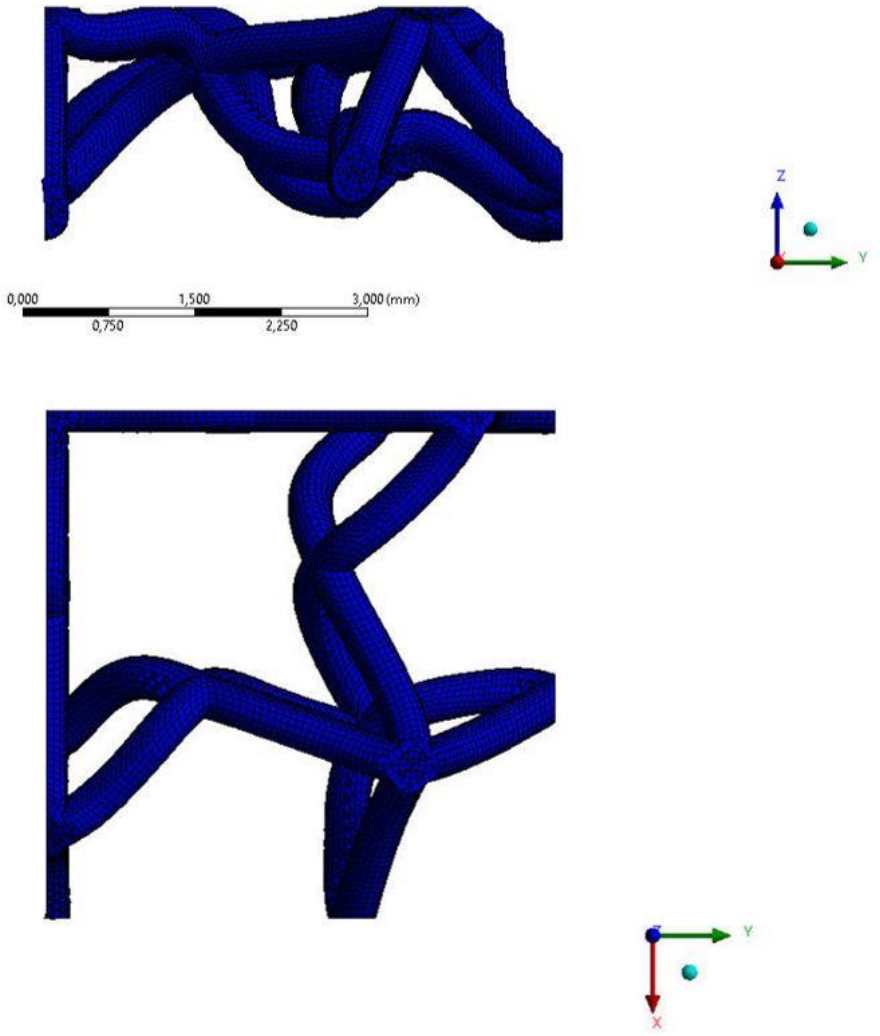

Figure 71: first row top and side view (*bcc*).

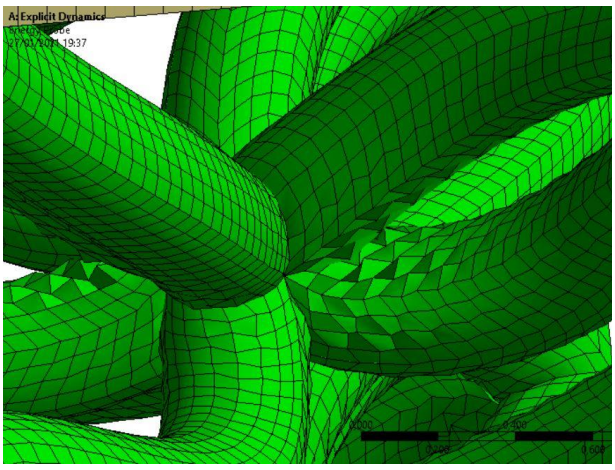

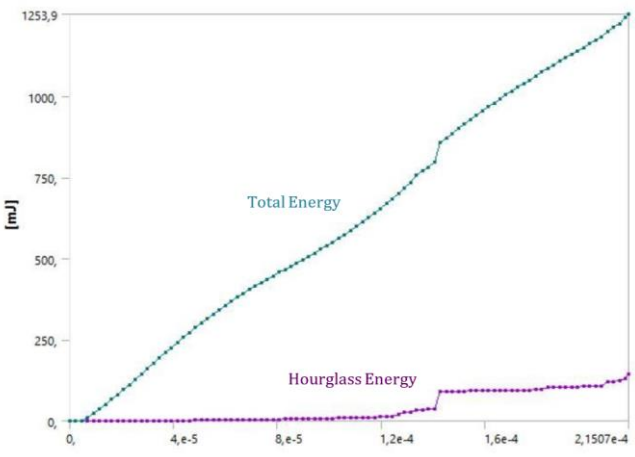

Figure 72 (left) and 73 (right): hourglass effect in deformation (*bcc*) and hourglass energy – time diagram (*fbcc*).

4.2 Second simulations set

4.2.1 Model

A second model for high speed crashing simulations has been developed in order to avoid problems occurred with the first model. This second model consists of a 3x3x1 sample, instead of ¼ of a 3x3x3 one. No symmetry conditions are applied, and there is no model division in order to reduce the node number. In this way we are also considering border effects into the results: the number of RVE are by the way enough to be representative of the typical lattices behavior, as results will show. Another important point about the border effects is that it is evident how they depend on the definition of the RVE. The cell set we decided to consider can be basically modeled in two ways, as it is possible to see in figure 74.

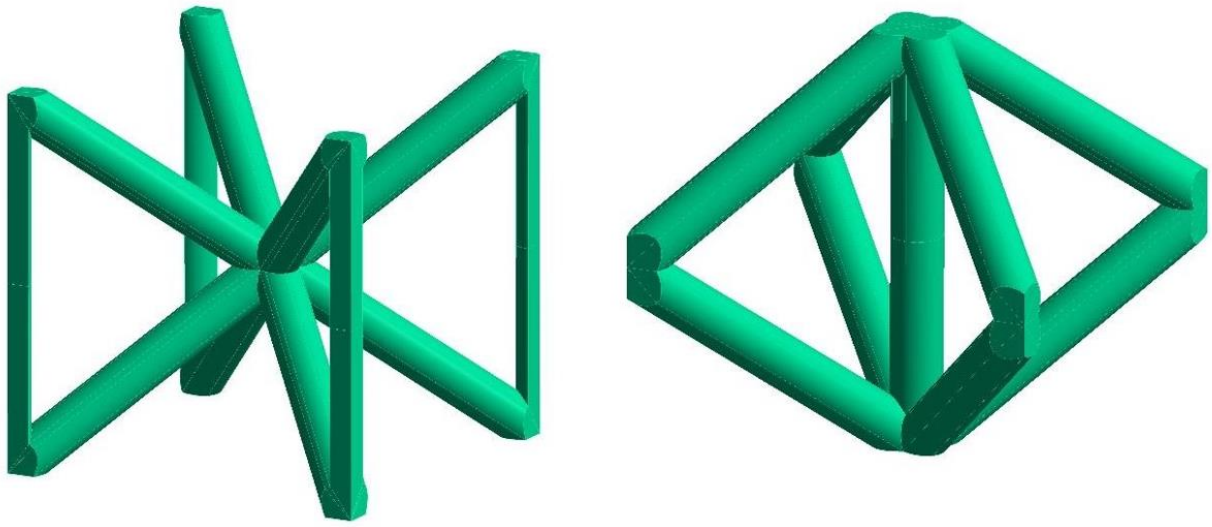

Figure 74: two ways of defining the RVE for cells set considered (*bccz*).

The first way (V1) is the one used up to now, the second way (V2) is the one meant to be used in these simulations. V2 offers the possibility to define the vertical struts in their integrity. When symmetry conditions are not present, modeling RVE with V2 can theoretically improve the quality of the results following the next considerations: a full vertical strut presents a different buckling load rather than four quarters of the same strut at the corners of the RVE; this aspect can establish a step forward in making analyses more realistic. Not only buckling and instabilities of vertical struts are points to consider in this case, but also the fact that, during the loading process, all of the struts tend toward their natural behavior when using V2. This is something that will be discussed in the result paragraph, since both configurations have been tested in order to make a confrontation possible.

The material used is of course AlSi10Mg with bilinear model. Unfortunately, it has been impossible to develop a strain rate dependent model because of the lack of experimental characterization. Meshing process is the same one used for past analyses. Once again, frictionless contact has been used to link upper and lower plate to the sample; upper plate presents a 200 m/s speed (as in the first model). There is a small offset between upper plate and sample, so that there is no initial contact between them: therefore, there is no risk of datapoints missing force entity because of timestep. Fixed plate is instead in direct contact with the sample. Figure 75 shows a picture of the model created using the V2 definition.

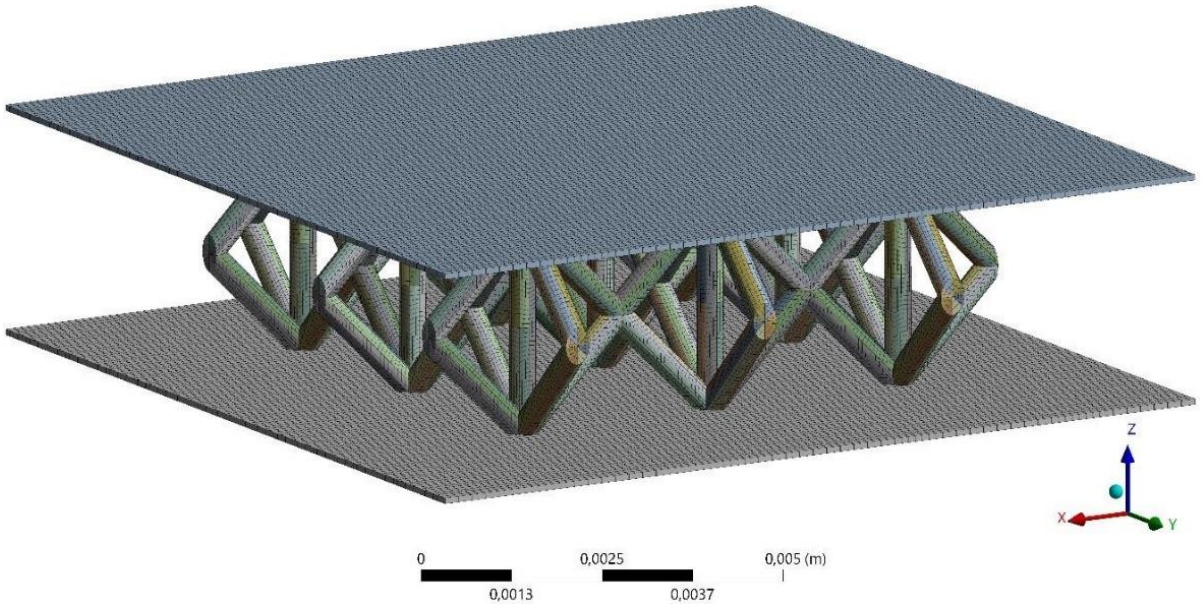

Figure 75: *fccz* V2 model.

Considering that the upper plate is moving at 200 m/s, the end time for each simulation has been set to $13*10^{-6}$ s, so that it is ensured the densification point is always reached. 300 datapoints equally distanced are used for time, force and displacement registration. Through force and displacement, it is possible to obtain stress-strain diagrams useful for energy absorption evaluations. Once again, the model just described takes inspiration from [45] and [46] for the loading application system and from [32] for the sample modeling; here actually a 5x5x1 sample is used, while for this investigation a 3x3x1 is the only possibility because of nodes limitation.

4.2.2 Post-processing

For the properties evaluation of the cells selected, a set of parameters has been established. The criteria defined in [47] and [48] best fit the description of the lattice behavior under crashing load, though the formulation of such parameters has been defined for cellular solids in general. The typical behavior can be summed up in three phases: a linear segment with an initial stress peak, a plateau

where most of the energy absorption characteristic lies and finally a rise that represent the densification. The relationship between plateau and peak stress allows the definition of the Crashing Load Efficiency (CLE). This parameter defines how the plateau gradually follows the peak: this establishes, besides the quality of the energy absorption defined by the level of the plateau, also how big is the discrepancy between the initial response of the structure and the one that actually set the most important behavior form the point of view of energy absorption. A high stress peak is also linked with the inertial response of the structure: a lower peak usually means a lower inertial response and therefore a safer condition for the rest of the structure the studied part is linked with.

Once the stress-strain diagram is obtained, the first step is of course the evaluation of the Volumetric Energy Absorption, that can be simply defined as:

$$VEA = \int_0^{\varepsilon} \sigma(\varepsilon) d\varepsilon$$

Next passage is the definition of the EA Efficiency Parameter η. This parameter relates the energy absorbed by the considered structure with the energy absorbed by an ideal absorber, when both present the same peak stress:

$$\eta = \frac{\int_0^{\varepsilon} \sigma(\varepsilon) d\varepsilon}{\sigma_{pk}}$$

Peak stress σ_{pk} is the maximum stress registered up to the strain when the integral is estimated. Using η it is possible to determine the densification strain ε_{cd}, in other words the strain where the Energy Absorption Parameter reaches its maximum, The phenomenon of the densification and the strain that is related to it can be pre-defined approximatively making a simple consideration: subtracting the number of the struts that are opposing to the crashing action in the load direction multiplied for the strut diameter from the RVE height it is possible to determine a theoretical densification displacement though which we can establish a pre-analytical densification strain. This consideration might be useful for analyses making use of a simpler model, and results will be a good feedback, as next paragraph will show. ε_{cd} is the last parameter needed for the calculation of the plateau stress:

$$\sigma_{pl} = \frac{\int_0^{\varepsilon_{cd}} \sigma(\varepsilon) d\varepsilon}{\varepsilon_{cd}}$$

The actual range of evaluation should be starting from the stress coincident with the beginning of the plateau. Due to oscillations following the peak stress, there is not a way to analytically define this strain; so, the energy accounted in the numerator of the previous expression also considers the linear

part of the diagram (the one with the initial peak). Since the biggest energy absorption contribution comes from the plateau region and not from the linear region, it is possible to assume that in the total amount of energy registered from strain zero to ε_{cd} the linear energy is neglectable with respect to the plateau energy, allowing a valid way to define the plateau stress. At this point the Crashing Load Efficiency can be evaluated:

$$CLE = \frac{\sigma_{pl}}{\sigma_{pk}}$$

In order to make comparison between cells possible, energy parameters such as pure EA, SEA and VEA have been evaluated at densification points (that are by the way very similar to each other).

4.2.3 Results

Next pictures (figures 76-84) show Stress - Strain, Volumetric Energy Absorption - Strain and Energy Absorption Efficiency - Strain diagrams for V1 configuration simulations.

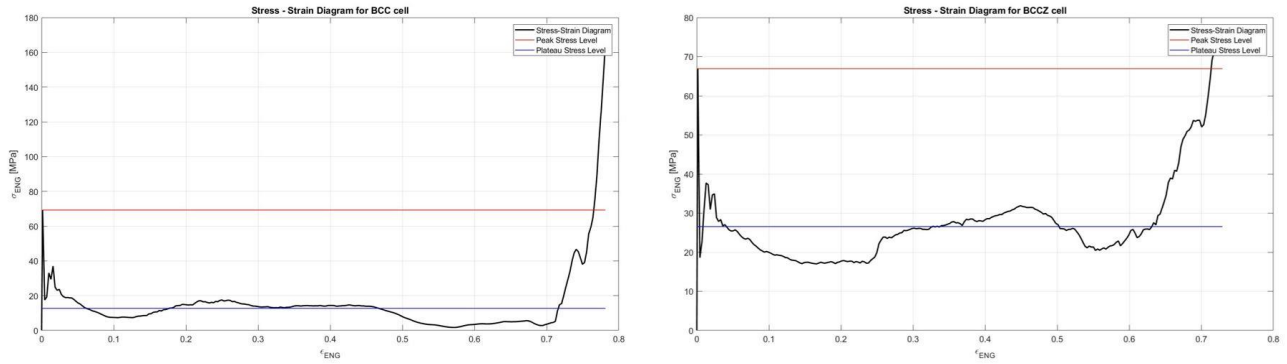

Figure 76: Stress - Strain diagrams for *bcc* and *bccz* V1 configuration.

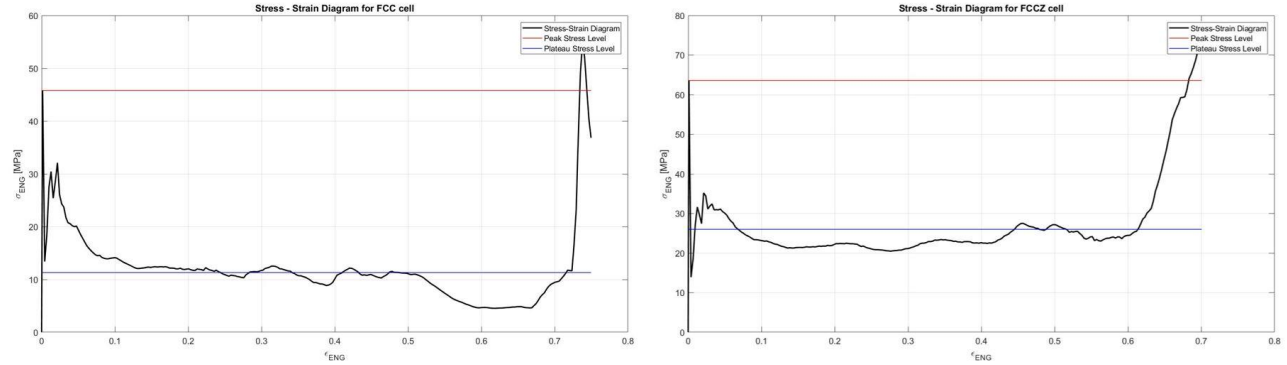

Figure 77: Stress - Strain diagrams for *fcc* and *fccz* V1 configuration.

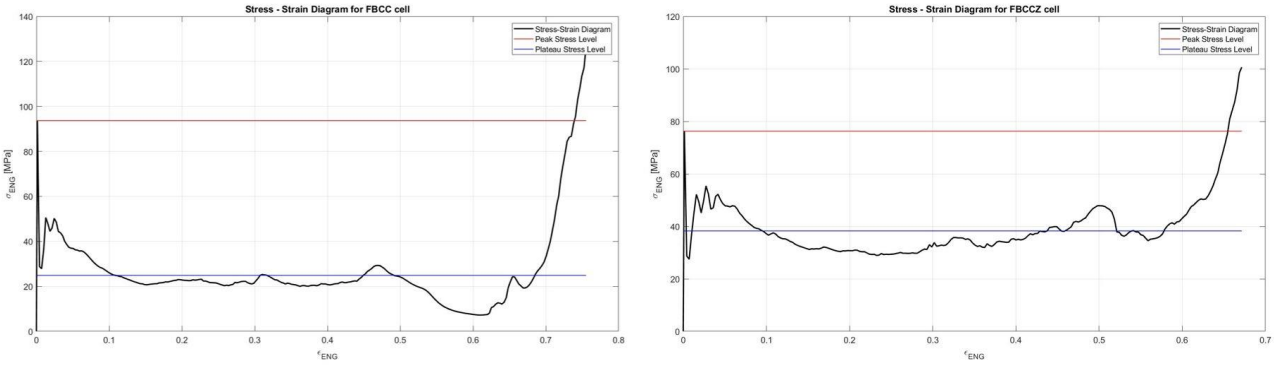

Figure 78: Stress - Strain diagrams for *fbcc* and *fbccz* V1 configuration.

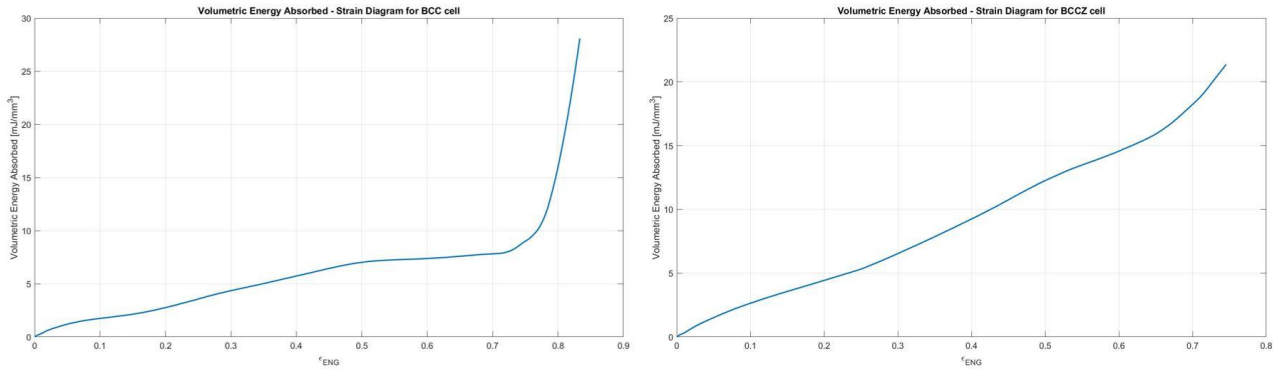

Figure 79: Volumetric Energy Absorption - Strain diagrams for *bcc* and *bccz* V1 configuration.

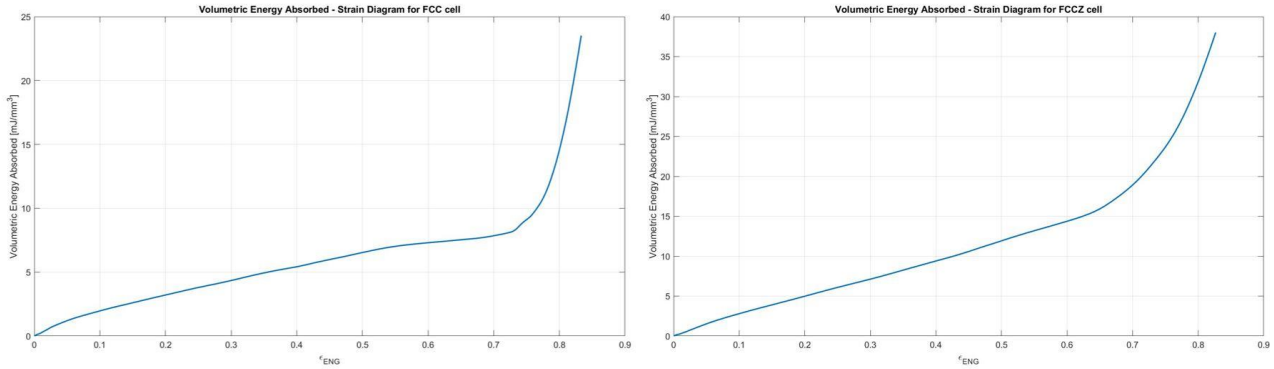

Figure 80: Volumetric Energy Absorption - Strain diagrams for *fcc* and *fccz* V1 configuration.

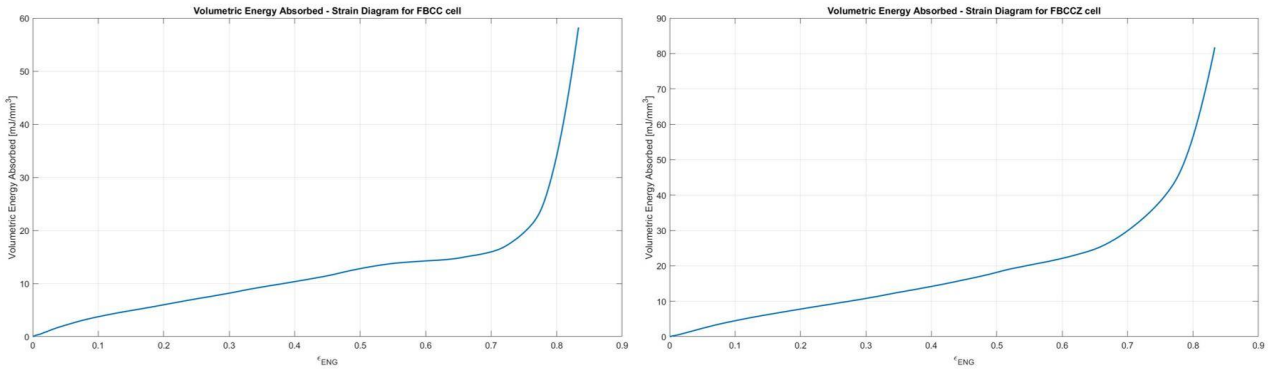

Figure 81: Volumetric Energy Absorption - Strain diagrams for *fbcc* and *fbccz* V1 configuration.

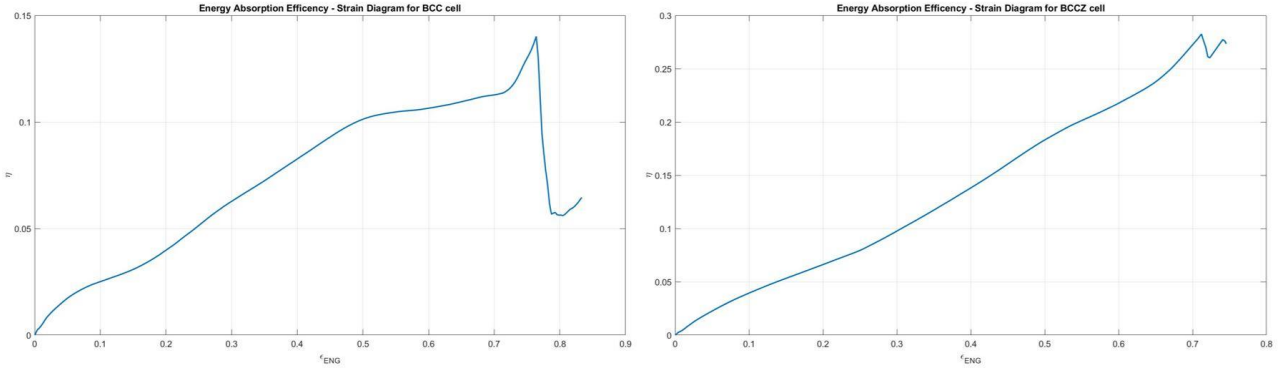

Figure 82: Energy Absorption Efficiency - Strain diagrams for *bcc* and *bccz* V1 configuration.

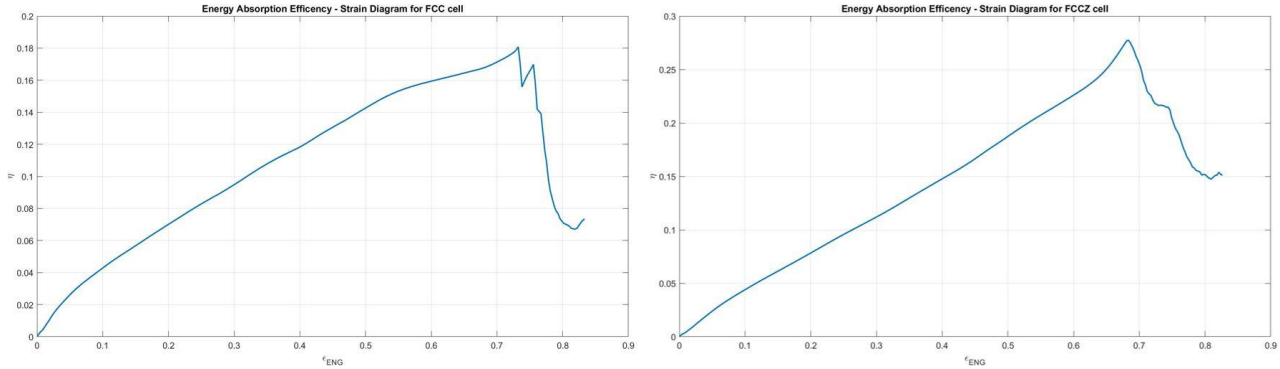

Figure 83: Energy Absorption Efficiency - Strain diagrams for *fcc* and *fccz* V1 configuration.

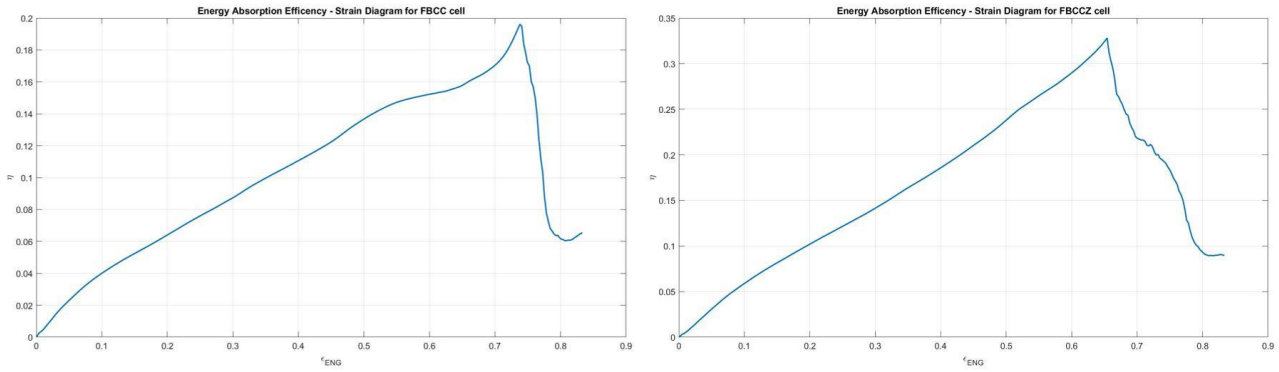

Figure 84: Energy Absorption Efficiency - Strain diagrams for *fbcc* and *fbccz* V1 configuration.

From Stress - Strain diagrams it is evident that the way of defining plateau and peak stress has worked quite good from the graphical point of view. It is impossible to establish a precise plateau stress since the plateau region is filled with oscillations; by the way method used has provided a good average level (blue lines on diagrams). The three stages behavior (introduced in chapter 1) is evident in every diagram. Energy Absorption and Efficiency - Strain diagrams show different levels going from non-reinforced to reinforced cells; compromise between energy and mass will be discusses later though. It is also evident where the densification point is for every cell. This point is very similar for *bcc*, *fcc* and *fbcc* while for reinforced cells densification arrives before, because of the vertical struts that works against the crashing action together with oriented struts.

Something that can be concerning about simulations for V1 is the deformation of the outer struts of the model: this problem can be actually found in both vertical and oriented struts. As previously said, when it comes to model vertical struts of the outer surfaces, these have to be split into halves or quarters. Because of this, the buckling load is going to radically change due to geometry, and this can result into non-realistic ways of deformation and loads and therefore in information loss (see figure 85).

Another similar issue about outer struts is the fact that oblique ones are hanging freely as oriented cantilever beams. While the upper plate is crashing these struts, the force application point starts going toward the inner part of the sample, resulting into what can be seen as a wrong behavior of the strut (figure 86). This once more is a nonrealistic way of deformation.

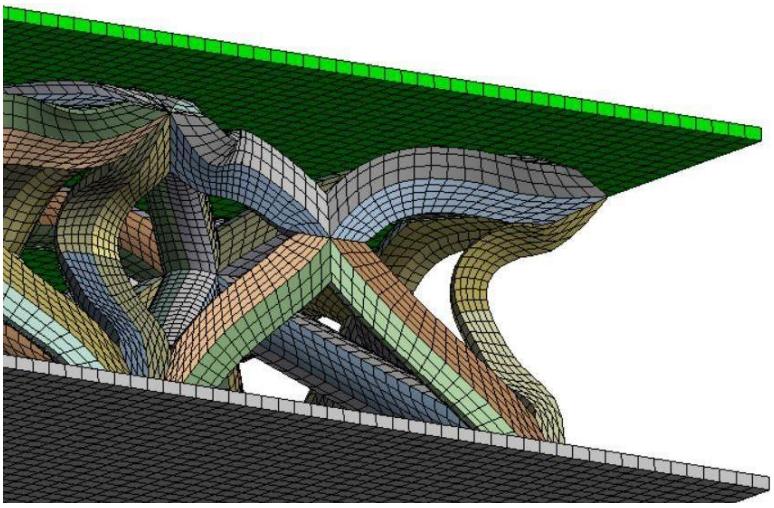

Figure 85: buckling in outer quarters and halves of vertical struts (*fbccz* V1).

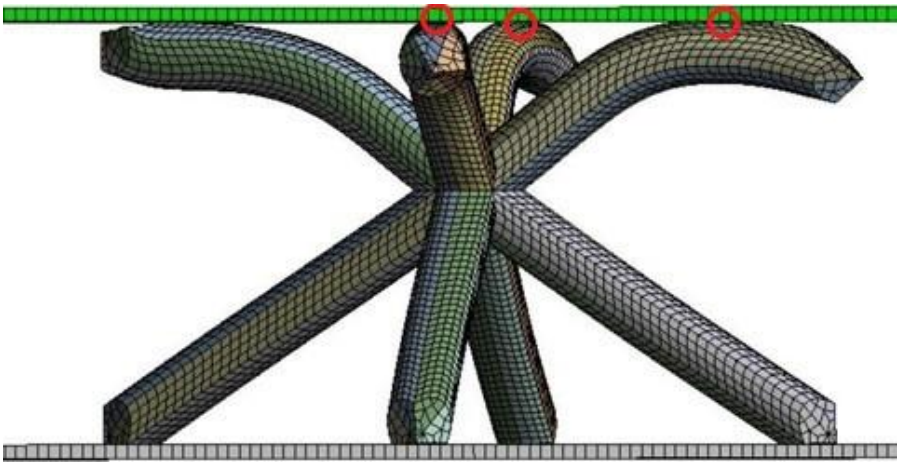

Figure 86: touching points (red circles) between struts and upper plate in a border cell (*bcc* V1).

These issues lead to the attempt to define the RVE in a different way, that is V2 configuration. Results for V2 are showed in figures 87-95.

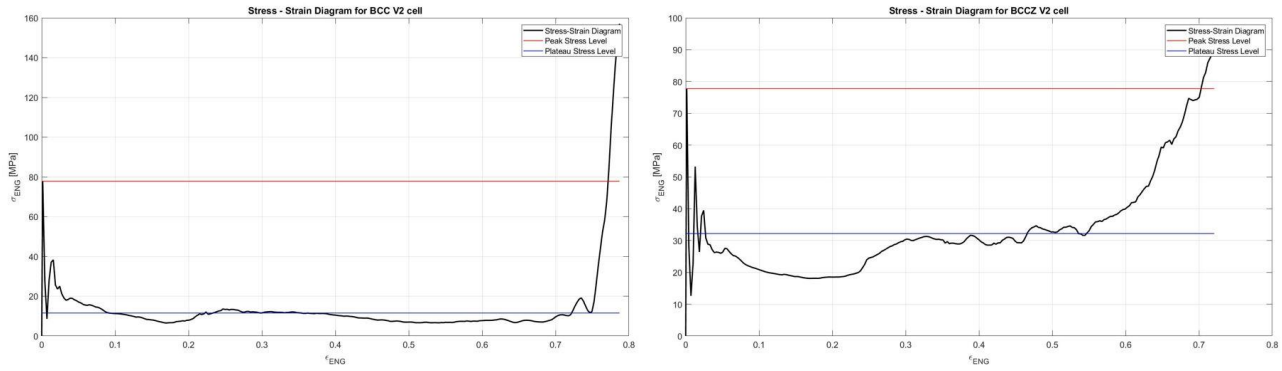

Figure 87: Stress – Strain diagrams for *bcc* and *bccz* V2 configuration.

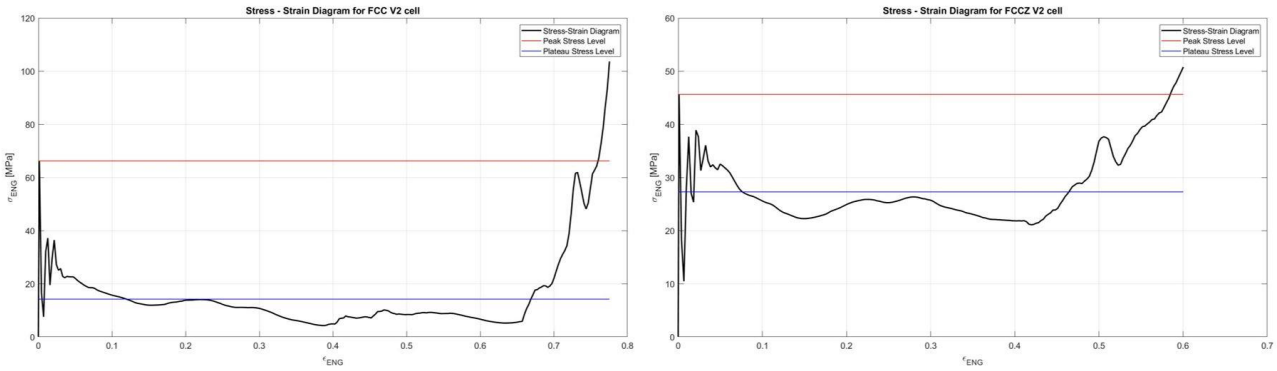

Figure 88: Stress – Strain diagrams for *fcc* and *fccz* V2 configuration.

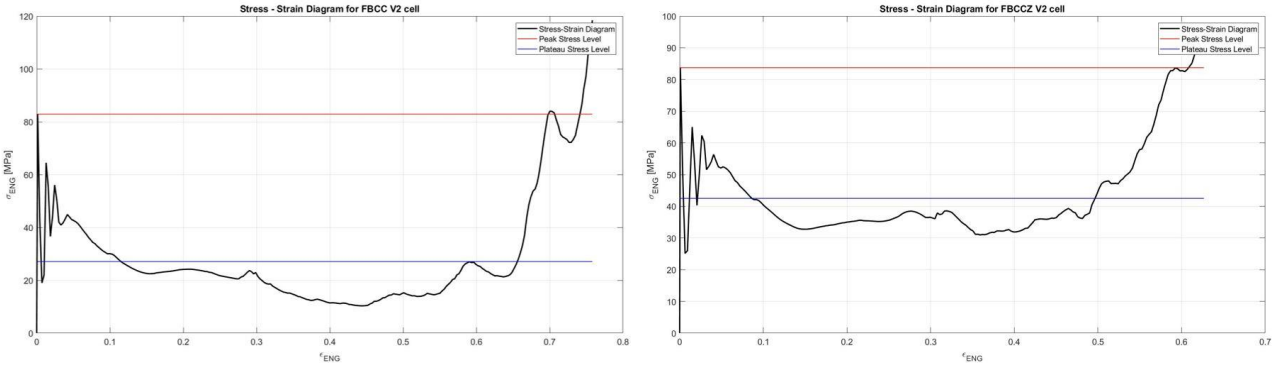

Figure 89: Stress – Strain diagrams for *fbcc* and *fbccz* V2 configuration.

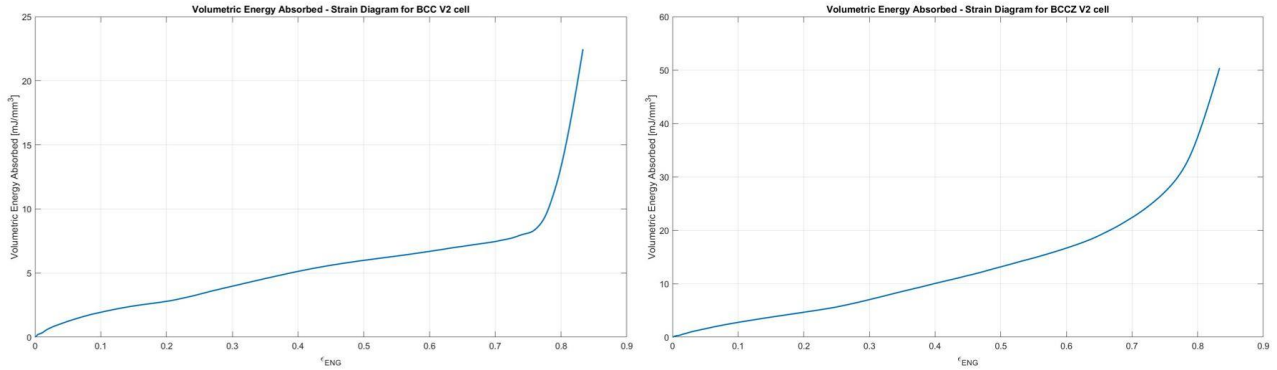

Figure 90: Volumetric Energy Absorption – Strain diagrams for *bcc* and *bccz* V2 configuration.

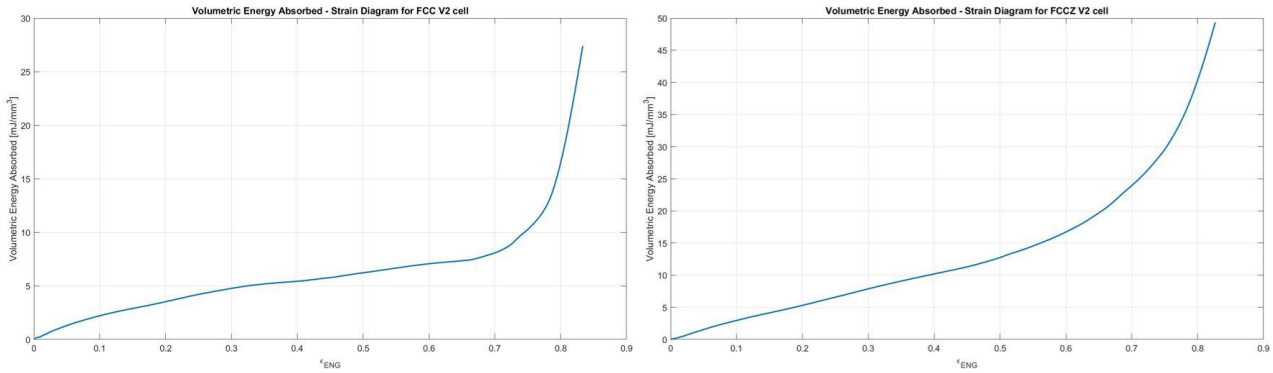

Figure 91: Volumetric Energy Absorption – Strain diagrams for *fcc* and *fccz* V2 configuration.

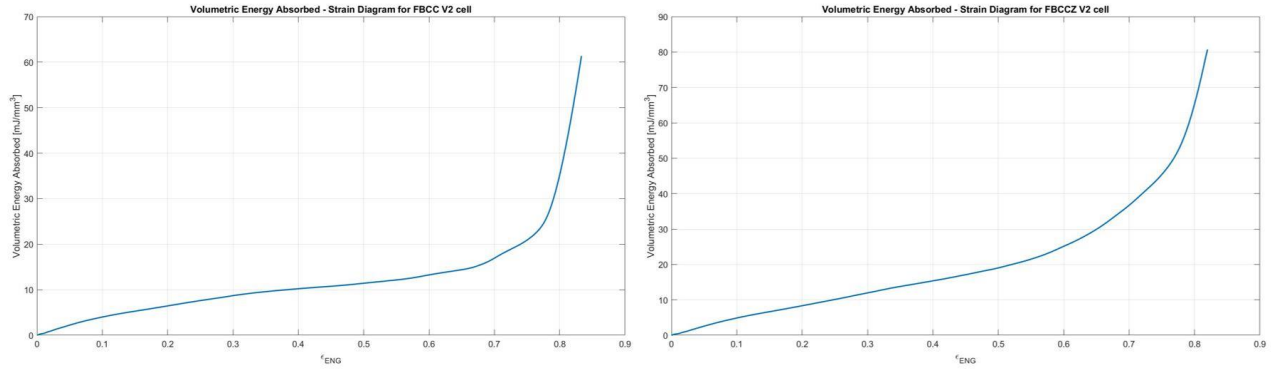

Figure 92: Volumetric Energy Absorption – Strain diagrams for *fbcc* and *fbccz* V2 configuration.

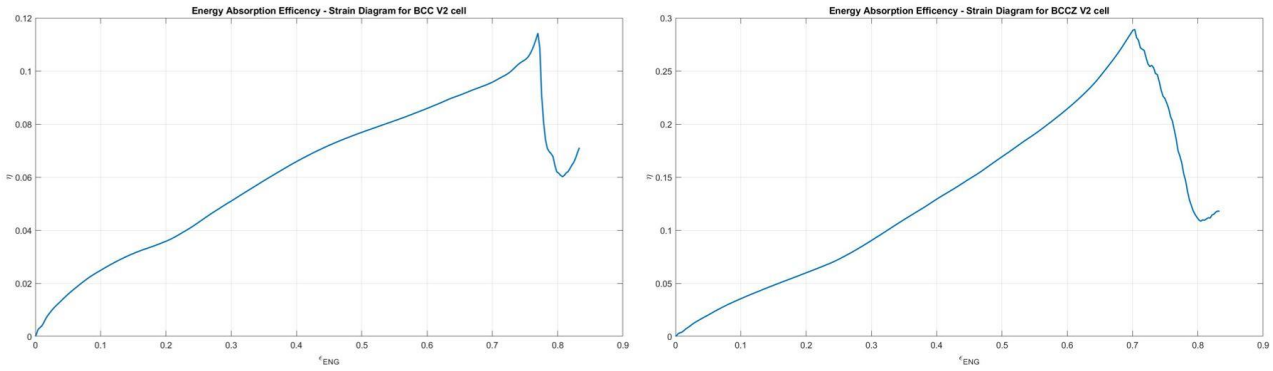

Figure 93: Energy Absorption Efficiency – Strain diagrams for *bcc* and *bccz* V2 configuration.

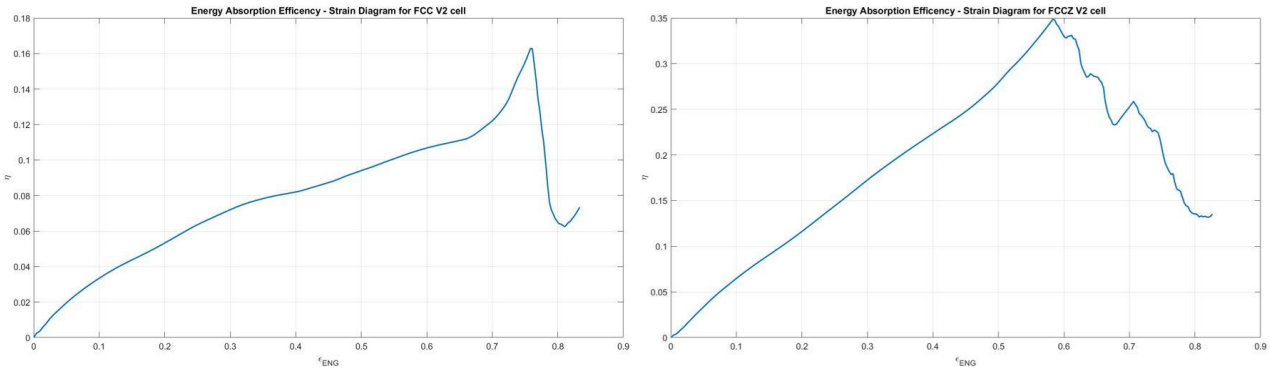

Figure 94: Energy Absorption Efficiency – Strain diagrams for *fcc* and *fccz* V2 configuration.

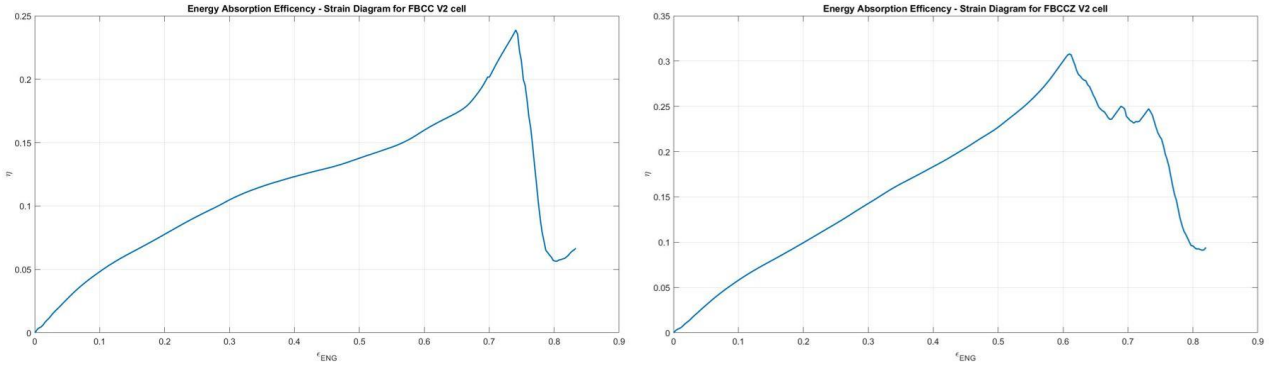

Figure 95: Energy Absorption Efficiency – Strain diagrams for *fbcc* and *fbccz* V2 configuration.

Qualitatively, V2 configuration diagrams appear to be similar to the V1 ones. Main difference between the two models lies in the local deformation, shown in figure 96.

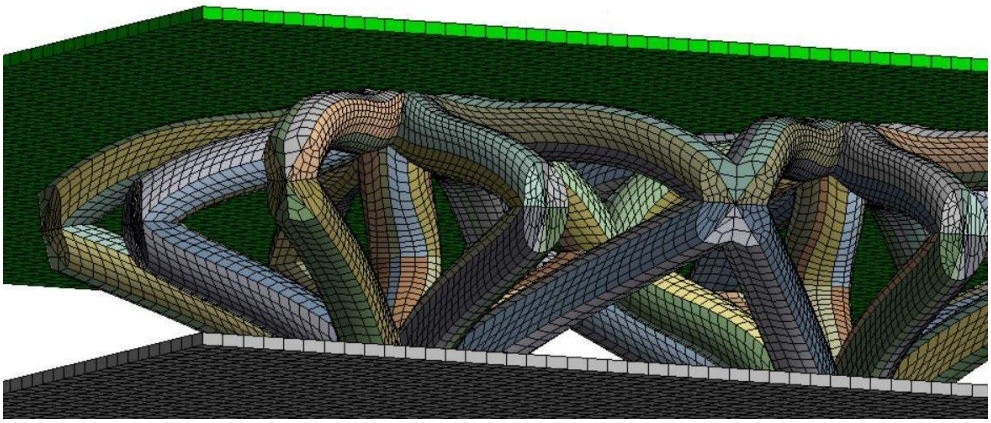

Figure 96: deformation caught during the plateau region (*fbccz* V2).

First of all, there are nine full vertical struts (for cells where reinforcement is due) for each sample and that means a more realistic buckling phenomenon rather than having halves and quarters of

vertical struts at the border, as in V1. Also, all of the struts are "activated": in other words, also *fcc*-like and *bcc*-like border struts are behaving respectively in stretching and bending. Of course, border effects are still present but limited with respect to V1 configuration, since struts intersection points at the border are still free to displace.

Besides considerations made up to now about the two configurations, a better comparison is possible by looking at data in Table 12 and 13:

V1	σ_{pk}	σ_{pl}	ε_{cd}	EA	VEA	SEA	CLE	$\bar{\rho}$	mass
	MPa	MPa	/	mJ	mJ/mm^3	mJ/g	/	/	g
bcc	69,29	12,71	0,7640	2359,537	9,7100	49241,40	0,1834	0,0736	0,0479178
bccz	66,94	26,55	0,7120	4594,342	18,9068	84809,40	0,3967	0,0832	0,0541726
fcc	45,81	11,31	0,7322	2012,545	8,2821	51295,20	0,2469	0,0602	0,0392346
fccz	63,60	26,01	0,6833	4318,237	17,7705	95644,60	0,4089	0,0693	0,0451488
fbcc	93,66	24,89	0,7380	4463,727	18,3692	54211,63	0,2658	0,1264	0,0823389
fbccz	76,30	38,26	0,6542	6083,196	25,0337	68952,31	0,5015	0,1355	0,0882232

Table 12: data for V1 configuration simulations.

V2	σ_{pk}	σ_{pl}	ε_{cd}	EA	VEA	SEA	CLE	$\bar{\rho}$	mass
	MPa	MPa	/	mJ	mJ/mm^3	mJ/g	/	/	g
bcc	77,86	11,56	0,7698	2161,434	8,8948	45107,17	0,1484	0,0736	0,0479178
bccz	77,75	32,19	0,7034	5501,207	22,6387	101549,71	0,4139	0,0832	0,0541726
fcc	66,20	14,21	0,7583	2618,289	10,7749	66734,26	0,2147	0,0602	0,0392346
fccz	45,62	27,28	0,5830	3864,292	15,9024	85590,18	0,5979	0,0693	0,0451488
fbcc	82,91	27,08	0,7409	4876,338	20,0672	59222,75	0,3267	0,1264	0,0823389
fbccz	83,74	42,49	0,6095	6293,851	25,9006	71340,05	0,5074	0,1355	0,0882232

Table 13: data for V2 configuration simulations.

There are various discrepancies between the two models, but overall magnitudes are the same for the shown properties. In order to better understand these results, they have been graphed (figures 97-108).

The most variable parameter among the gathered data is the peak stress: it seems that in presence of bending behavior (*bcc*/*fbcc*) the addition of vertical struts tends to keep constant the peak stress (it slightly decreases for V1 and stays constant for V2). The real difference between the two configurations lies in the peak stress for *fcc* and *fccz*: V1 presents an increase going from non-reinforced to reinforced cells, the opposite happens for V2. In general, it can be said that the peak stress, looking at reinforcements as particular cases of normal cells, is higher in *fbcc* followed by *bcc* and *fcc* respectively: it can be noticed how this trend follows the relative density scale. The main effect of vertical struts can be seen in plateau stress (instead of peak stress, as supposed in the previous

chapter): while levels are extremely similar between V1 and V2 (slightly higher in V2, probably due to higher buckling load), plateau for reinforced cells always increases with respect to normal ones; this will have an important effect on CLE, as next graphs will show. Trend for non-reinforced cells is the same for both configurations. Main difference is, as expected, in the reinforced ones: *fccz* V1 presents a lower peak than the V2 version and this is due to the discrepancy in the peak stress discussed before. What is ensured is that the addition of vertical struts always tends to increase the efficiency of the crash, allowing less difference between peak and plateau, therefore a more stable process.

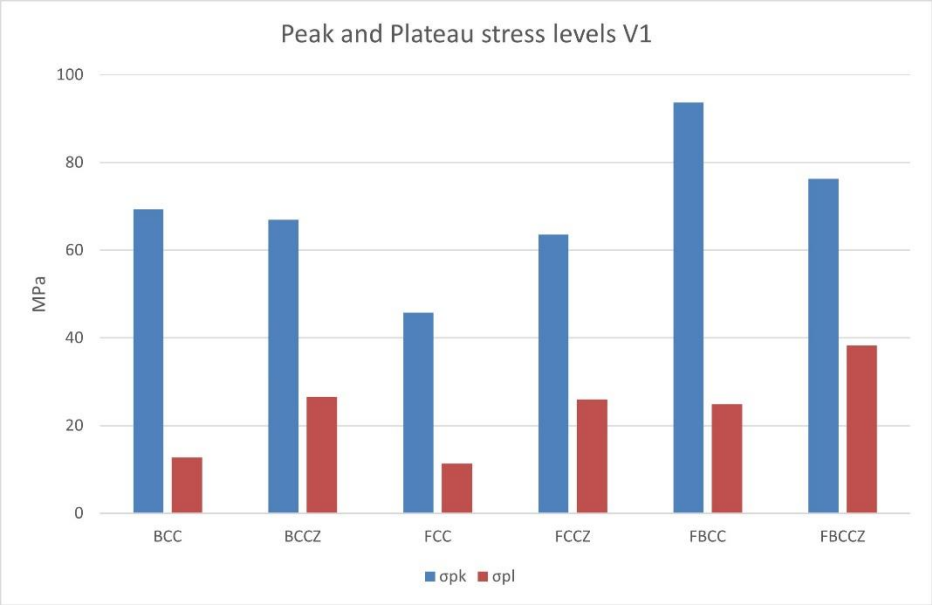

Figure 97: peak and plateau stresses for V1 configuration.

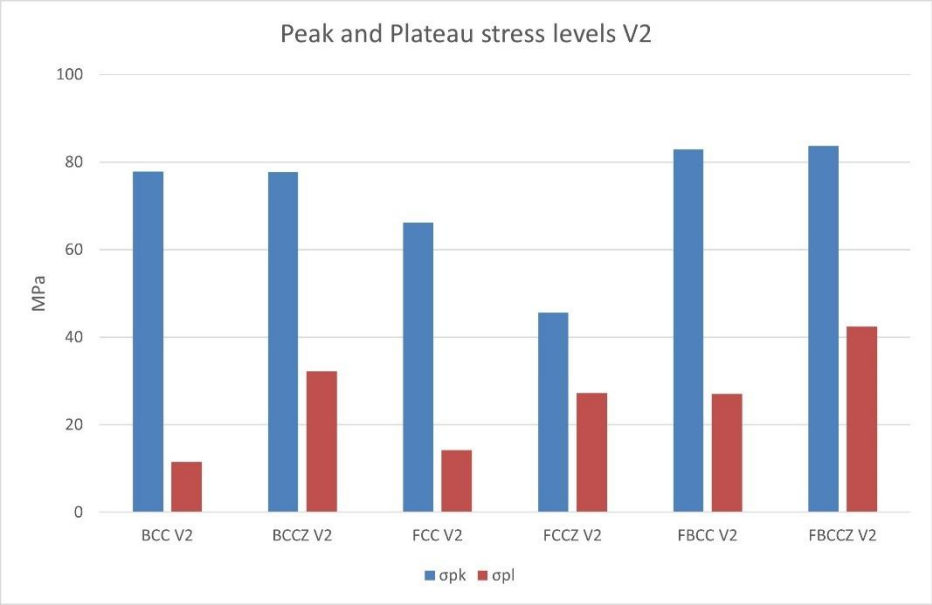

Figure 98: peak and plateau stresses for V2 configuration.

Tendencies are quite clear from the point of view of CLE also: CLE trend can be qualitatively compared with force reaction from static analyses: it can be seen in fact as a non-dimensional force parameter. The only not expected parameter is the *fccz* V2 CLE that goes beyond the *fbccz* one: that is due to the peak-plateau stresses inversion described before (that could be also due to the datapoints frequency registration). A good result can by the way be noticed in *bccz* from this parameter point of view; situation for this cell will even be better with energy parameters.

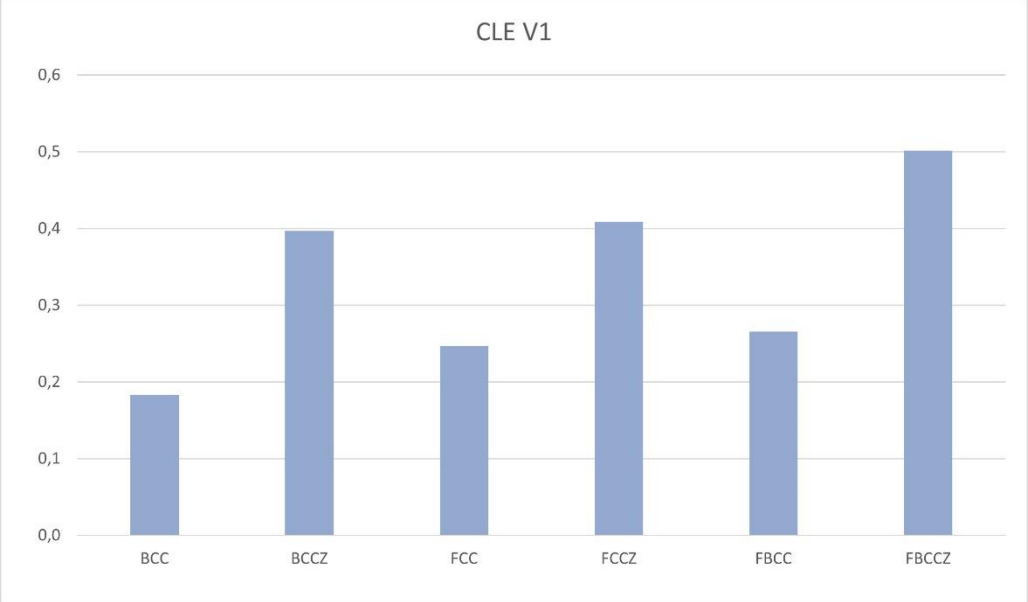

Figure 99: Crash Load Efficiency for V1 configuration.

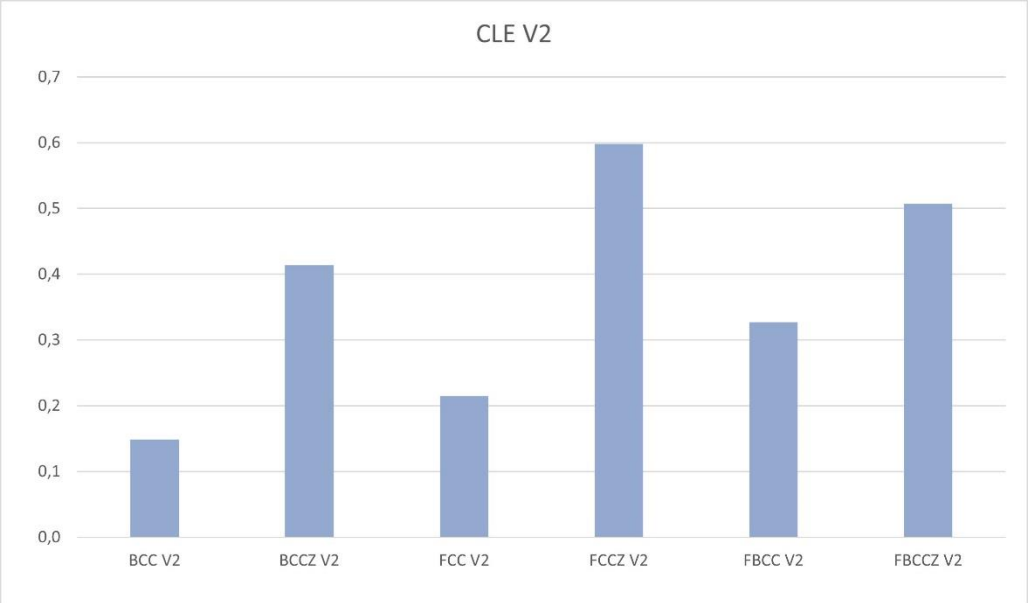

Figure 100: Crash Load Efficiency for V2 configuration.

The parameter where differences between V1 and V2 are extremely small is the densification point. This is good since it is the confirmation that the consideration that are going to be made on EA, SEA and VEA will be valid and a genuine comparison between configuration can be made for those parameters as well as it has been done for stresses parameters. The cells with highest densification strain are *bcc*/*bccz* and this is something that will highly influence energy parameters: this by the way is an advantage for these cells and it is something to consider for sure; because it means that the field where the energy absorption phenomenon is still efficient is larger in comparison with other cells.

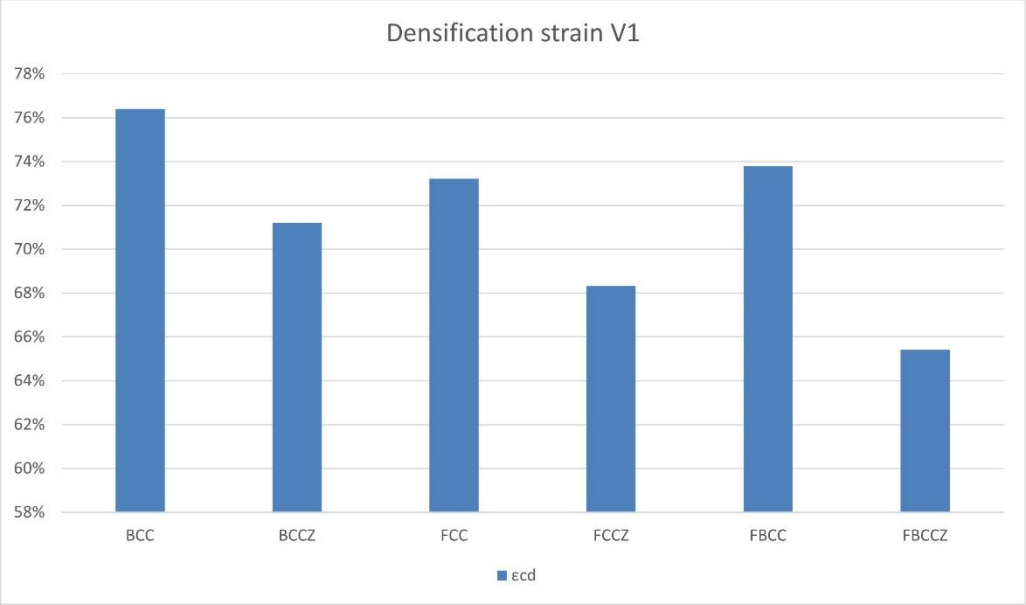

Figure 101: Densification Strain for V1 configuration.

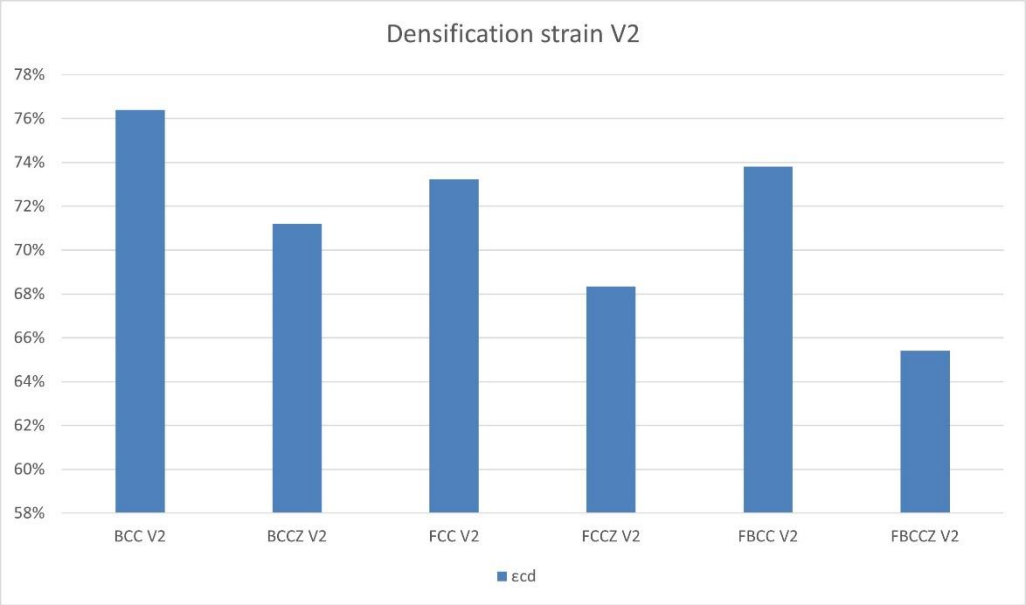

Figure 102: Densification Strain for V2 configuration.

When it comes to EA, there are basically two things that really differ in the shown graphs. The first is the evident difference between *bccz* V1 and V2 energy levels: in V2 results, *bccz* level surpass the *fccz* one. The motivation here lies in the higher densification strain that allows the absorption of a larger energy quantity; also, it can be concluded that vertical struts tend to work better for bending dominated cells rather than stretching dominated ones.

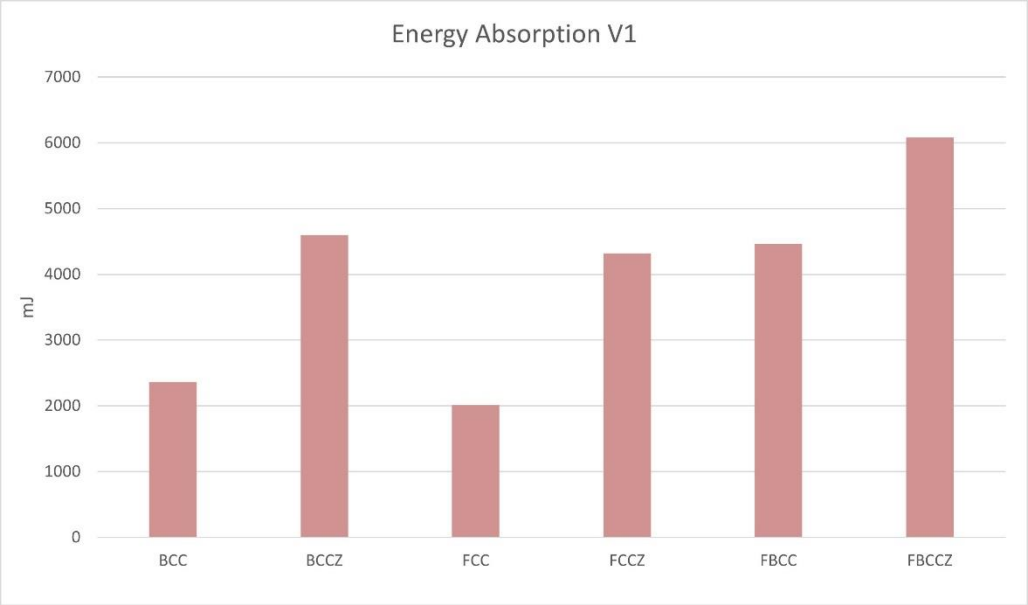

Figure 103: Energy Absorption for V1 configuration.

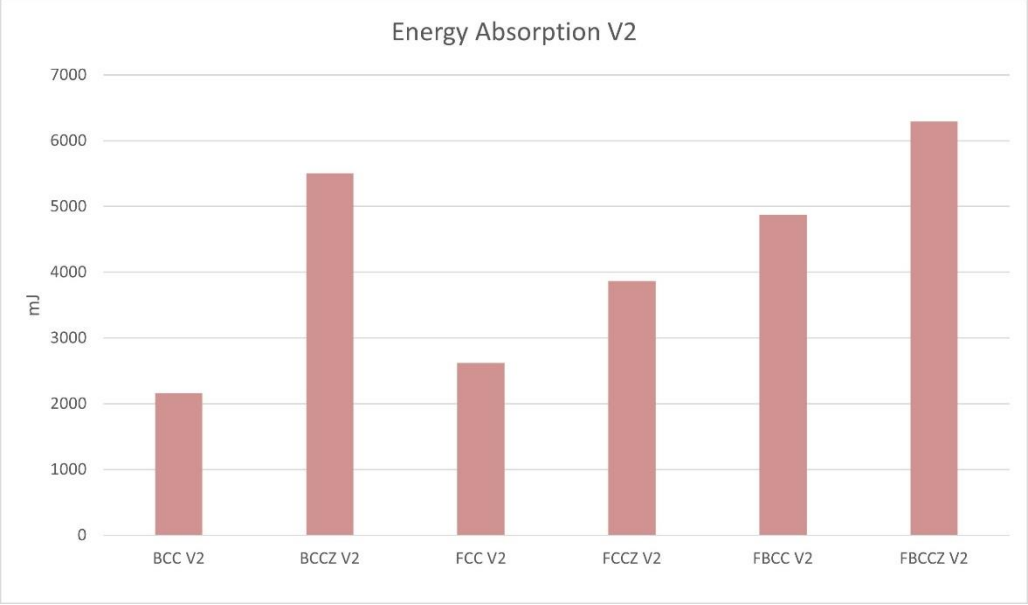

Figure 104: Energy Absorption for V2 configuration.

The second difference is that V2 version shows a higher energy level for *fcc* than for *bcc*, the opposite happens in V1. The second configuration tends to be much more similar (purely from a qualitative

point of view) to static analyses results; exception made for the *bccz* peak in EA, due to motivation that static analyses could not catch.

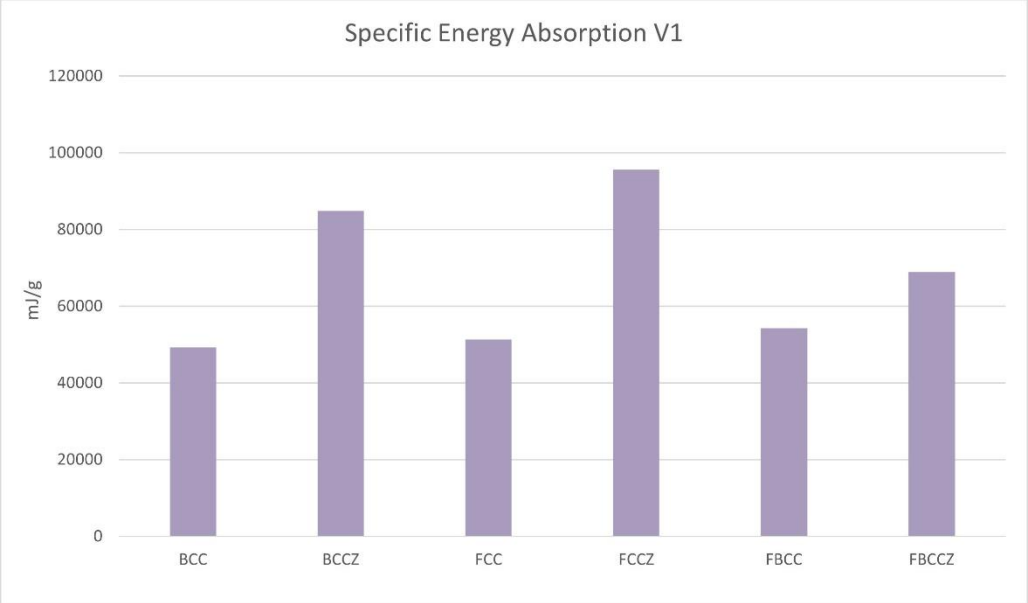

Figure 105: Specific Energy Absorption for V1 configuration.

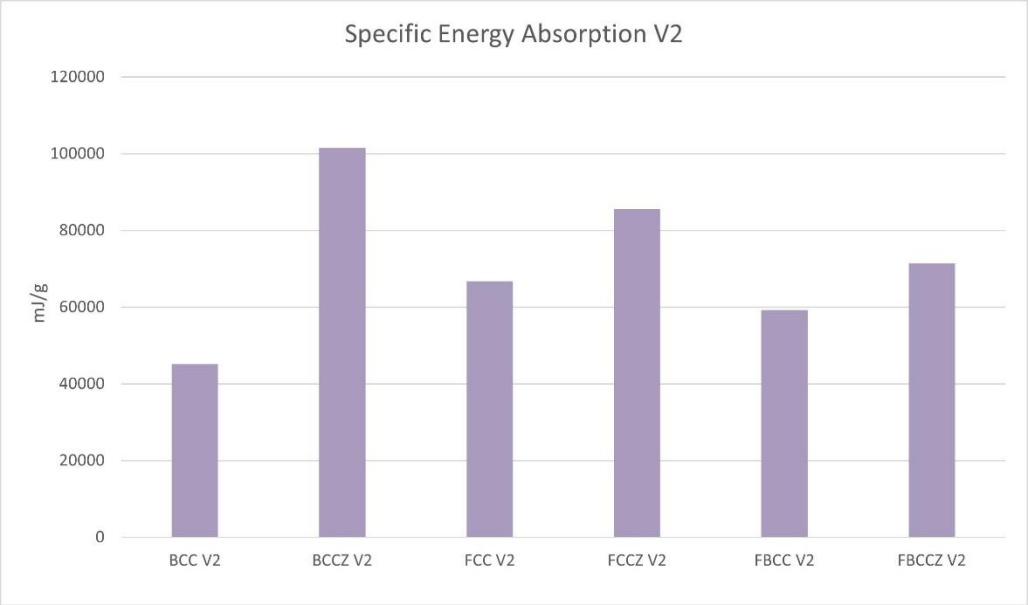

Figure 106: Specific Energy Absorption for V1 configuration.

Considering just *bcc*, *fcc* and *fbcc*, SEA can be compared to static results once again. Even from this point of view *bcc* gained much more importance because of the higher densification, though *bccz* relative density is slightly higher than *fccz* one, showing an excellent compromise for this cell. The main difference between the two configurations is again in the *bccz* levels: the motivation lies in the

vertical struts modeling that is way better for V2 configuration. VEA of course follows the exact trend of EA, being sample volumes the same for every simulation.

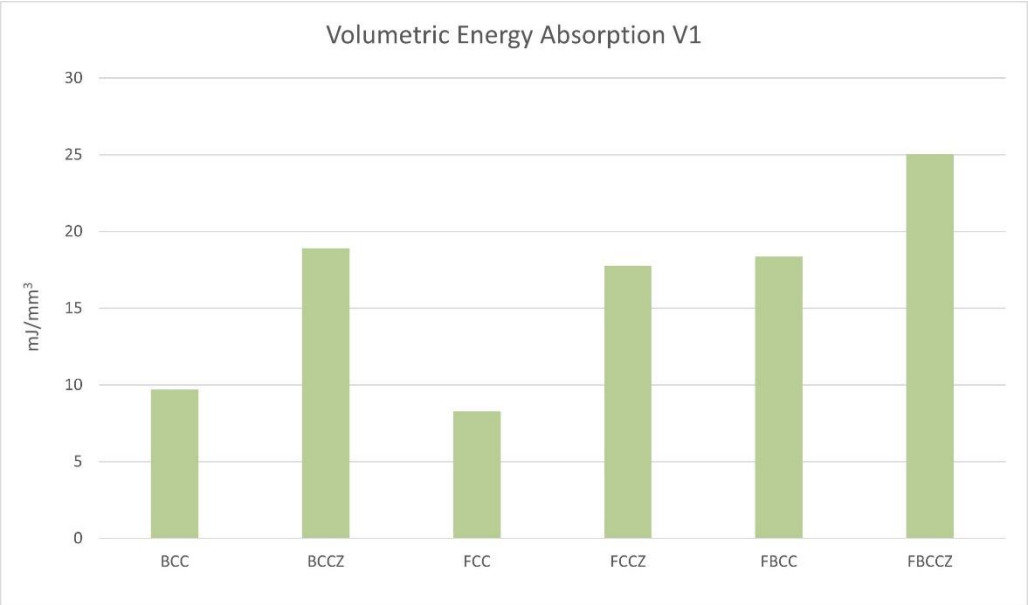

Figure 107: Volumetric Energy Absorption for V1.

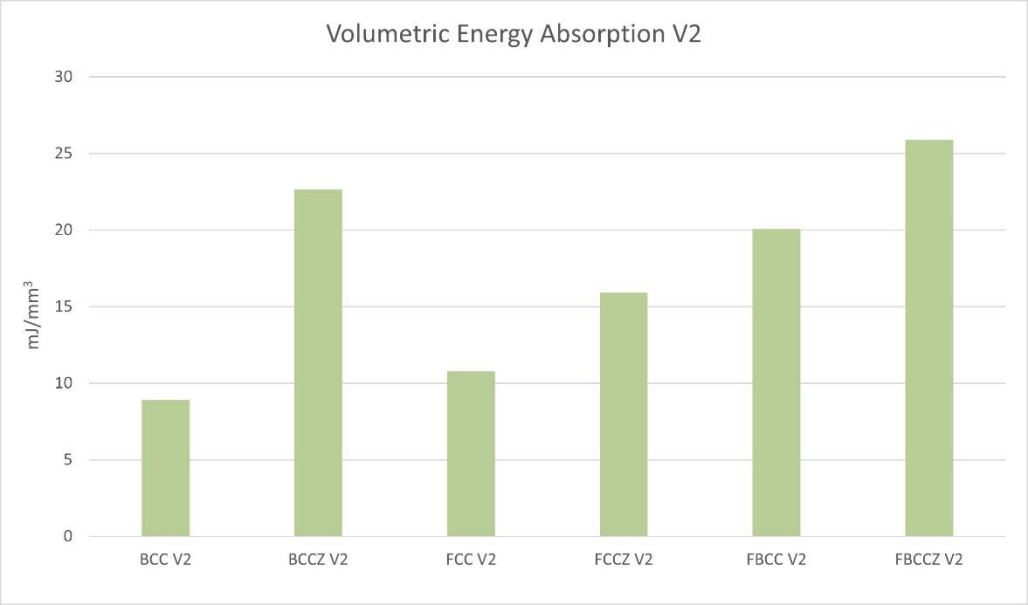

Figure 108: Volumetric Energy Absorption for V2.

4.2.4 Discussion

In the end, as expected, V2 configuration shows the most coherent results. Specific Energy Absorption levels, where *bccz* and *fccz* seem to be the most adequate energy absorbers, recall and confirm results about stress parameters where once again these cells achieved best CLE (in both configurations actually). Results from high speed crashing simulations confirmed static simulations

ones and at the same time gave us new information about Z-struts and their behavior in compression at high strain level and about how densification point can influence performance. In fact, from static analyses, vertical reinforcement seemed to be efficient for EA and VEA but not for force reaction (where a high force reaction was a problem because of inertia loads). The situation here changes, the CLE represent in fact the how the plateau stress is related to the peak stress, and besides giving us information about the stress in time and in evolving strain it also is a reference for EA, being the energy strictly related to plateau region. What maybe can give us information about eventual inertia loads is the peak stress, where once again bcc and *fcc* show lower peaks than *fbcc*; there is no big difference in peak stress going from non-reinforced cells to reinforced ones.

There actually is no main driver that can lead us in choosing the best cell among the ones considered, since many considerations of different nature have been made. It can be said though that, with the rule of compromise, *fccz* could be the most valid candidate showing both high CLE and SEA, but not very high pure EA level (where *bccz* and *fbccz* lead). The important role of Z-struts has been confirmed, showing excellent results from the point of view of both stress parameters and energy ones. Also, the influence of a higher densification strain makes *bccz* a very good candidate when it comes to SEA. Combination of cell (*fbcc* and *fbccz*) seems to be efficient from the point of view of CLE and pure energy absorbed, the problem with these is the higher relative density that results into limited SEA levels.

5 Homogenization

The interest of this investigation leads in the end toward multi-morphology design, that will be treated in the chapter 6: in order to make simulations more affordable for larger samples, a homogenization process is needed. In fact, making use of homogenization, lattices mesoscopic properties are linked with a medium, used in simulations as a bulk material. Homogenization models are for sure dependent on how more or less accurate the microstructure/mesostructure model the method is based on is well structured. These methods have been originally developed for composite materials, and that is why they are typically called Micromechanics models: when it comes to modeling lattices using these methods they are commonly referred to as Homogenization methods, also because lattices actually present a mesoscopic scale rather than microscopic one.

5.1 Homogenization process

For lattices and cellular solids in general, energy absorption lies in the plastic field rather than the linear one. That is the motivation that led to set aside the classic strain energy homogenization process. This process generates a linear orthotropic medium material whose properties are defined through linear static simulations for compression/traction and shear in the main principal directions. Once the stiffness matrix of the material is defined via simulations outputs, this is used to obtain the moduli needed for the definition of the orthotropic material (full process described in [49]). As said, this method is also used for properties definition of most composites where there are two or more phases composing a single repetitive section of a material: in such cases the process can describe a wide set of situations, because most composite materials present a linear behavior. That is not our case, we need a step forward for the definition of the medium: in other words, we need a material model that can describe the plastic field.

In bilinear and linear simulations, as well as in high speed crashing ones, AlSi10Mg plasticity has been modeled with bilinear isotropic hardening model. Resulting static crushing stress-strain diagrams (using node displacement to impose the loading) are basically bilinear as well, exception made for the yield passage that is gradual and not instantaneous. Plasticity for the medium material can be described quite well using bilinear model and making the assumptions that will be discussed in the next paragraph (a similar model is used in [50]). Initially an orthotropic model has been considered but later abandoned even though cells considered are transversely isotropic form the macroscopic point of view: these cells has been modeled keeping in mind they present a defined load direction: *fcc* for example is actually a *f2cc*, having struts only on the surfaces parallel to planes XZ

and YZ. It is not possible by the way to define bilinear orthotropy, thus it has been decided to use bilinear isotropy but only considering a prescribed load direction (Z), not being interested in the other directions (X/Y) behavior.

5.1.1 Bilinear static simulations

First step consists of performing static compression simulations necessary for the definition of stress-strain diagrams. One of the main assumptions of this model is the imposition of the Poisson ratio equal to zero: this is a strong assumption but, besides simplifying a lot the model, it is also valid for simple monoaxial loading. As said, all assumptions and limits of the process will be discussed later separately. Imposing ν = 0, G modulus will be automatically defined using the isotropic relationship:

$$G = \frac{E}{2(1+\nu)} = \frac{E}{2}$$

Tests are defined using the model described in chapter 2. The only thing that differs is that a 0,5 mm displacement is applied in the *-z* direction (and that is equal to strain 0,1667). It is sufficient both for going beyond the yield point and for gathering enough datapoints in the plastic field, later used for the definition of the plastic behavior. Large deflection option is used (being the RVE size 3mm), and stress stiffening effects are therefore considered. In these cases, moreover, conditions imposed at the middle vertical planes of the model used for avoiding torsional buckling, are extremely important: among static simulations performed up to now, this is the one with the highest displacement applied and results could be very influenced by these instabilities. Figure 109 shows stress – strain diagrams obtained.

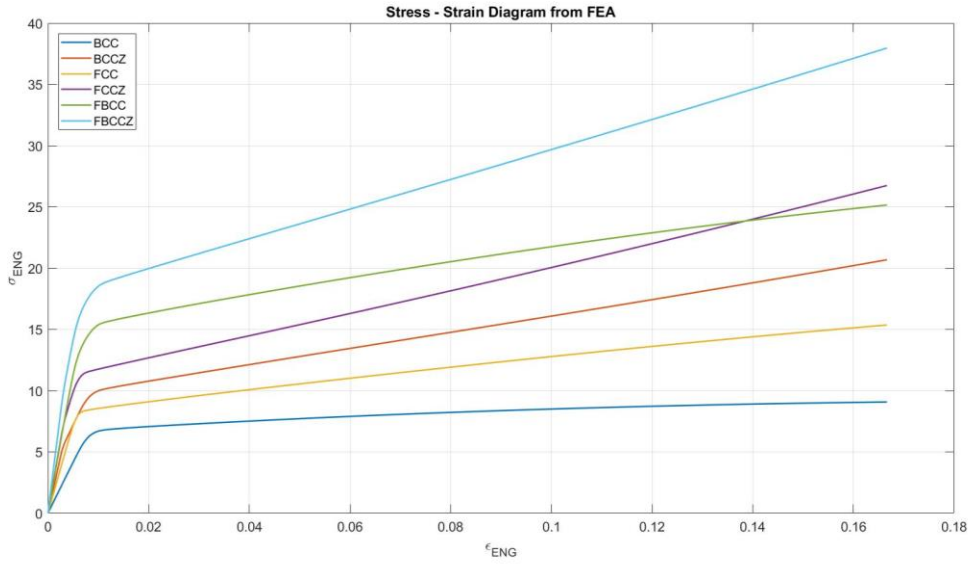

Figure 109: Engineering Stress – Strain obtained from static simulations for homogenization.

From the diagrams it is already evident the different behavior both in stiffness and yield stress, as well as the residual stiffness in the plastic segment. As expected, vertical struts tend to increase all of the cited properties in a very efficient way. Next steps are about defining these properties in a quantitative way.

5.1.2 Definition of E and E_T moduli

A set of 300 datapoints have been registered for each simulation; is it now possible to determine the two moduli defining the slope of the two main segments for each curve. To do so, Minimum Square Method has been used in order to construct a linear fit for each segment with a certain level of accuracy.

For the first segment, that is the linear one used for the evaluation of E modulus, the slope is defined using the datapoint from zero to X: datapoint X is the one that allows to obtain a R^2 equal to one, that is a perfect fit. Linear fits obtained can be seen in figure 110. While, for the plastic segment the slope is defined going from datapoint Y to the last one (that is coincident with strain 0,1667): Y datapoint is established as the one where strain is equal to 0,015 for every cell. R^2 factor for the second linear fit depends on the cell we are considering but never goes below 0,99 except for BCC where it is equal to 0,9679. Plastic linear fits are shown in figure 110.

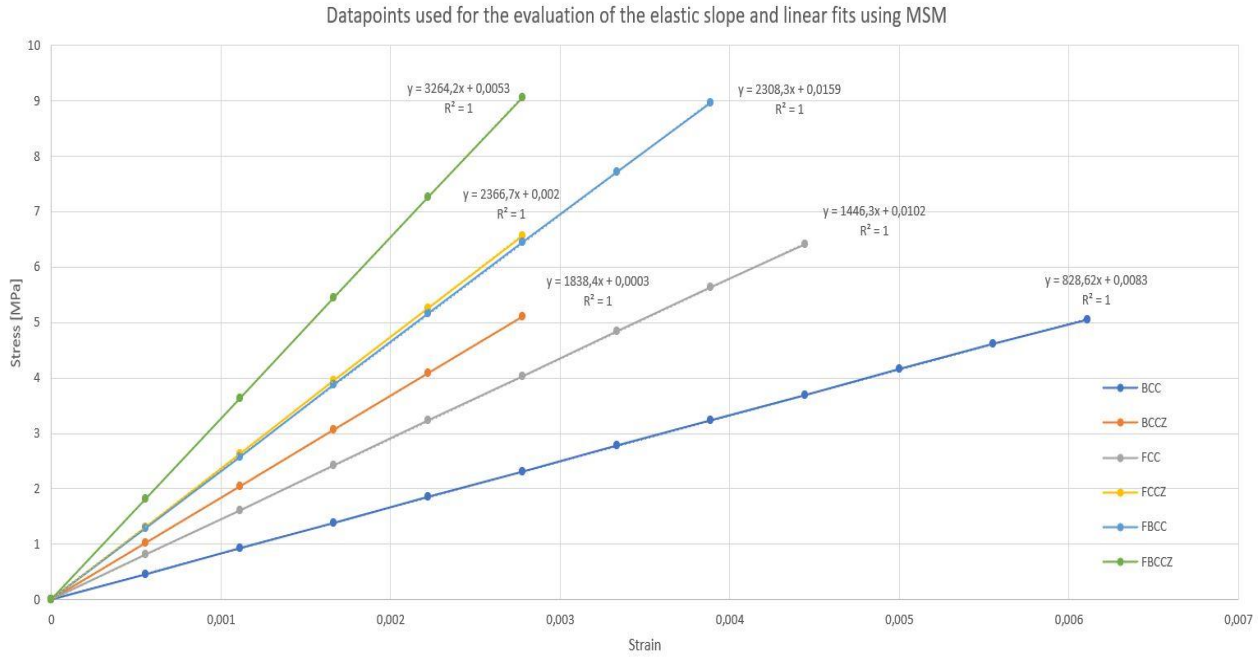

Fig. 110: Datapoints used for the evaluation of the elastic slope, and therefore the E modulus, and the relative linear fits (notice how the number of datapoints considered is selected so that R^2 factor is always equal to 1);

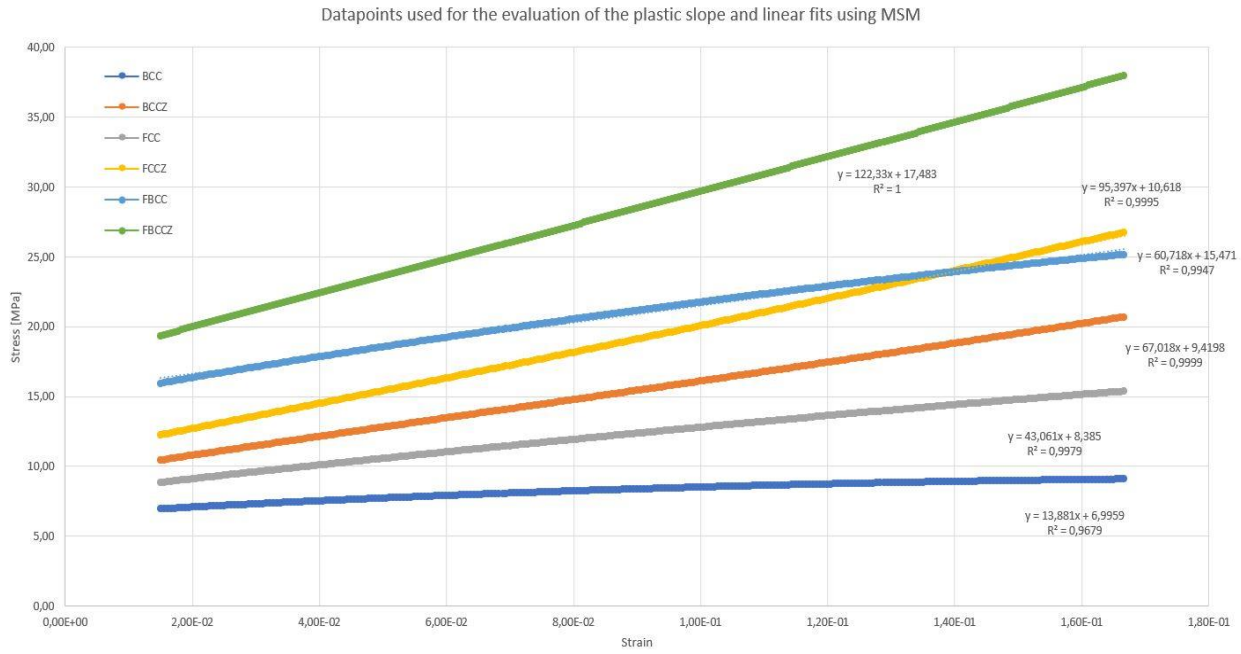

Fig.110: Datapoints used for the evaluation of the plastic slope, therefore the E_T modulus, and the relative linear fits;

With this passage we have already defined the linear and the tangent moduli: values can be read in the diagrams above as well as in the final table containing all the results achieved with the process.

5.1.3 Definition of the yield stress

Yield stress has been evaluated as the stress coincident with the intersection point of the two linear fits. Evaluation of the intersection point has been performed using Matlab script. In figure 111-116 original stress-strain diagrams and bilinear models are shown.

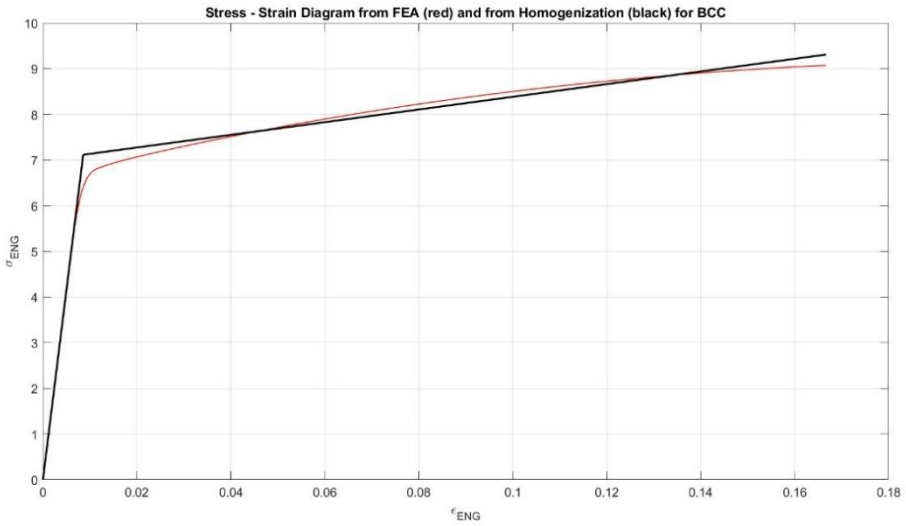

Figure 111: stress – strain diagram obtained using the homogenization process and the original one (*bcc*).

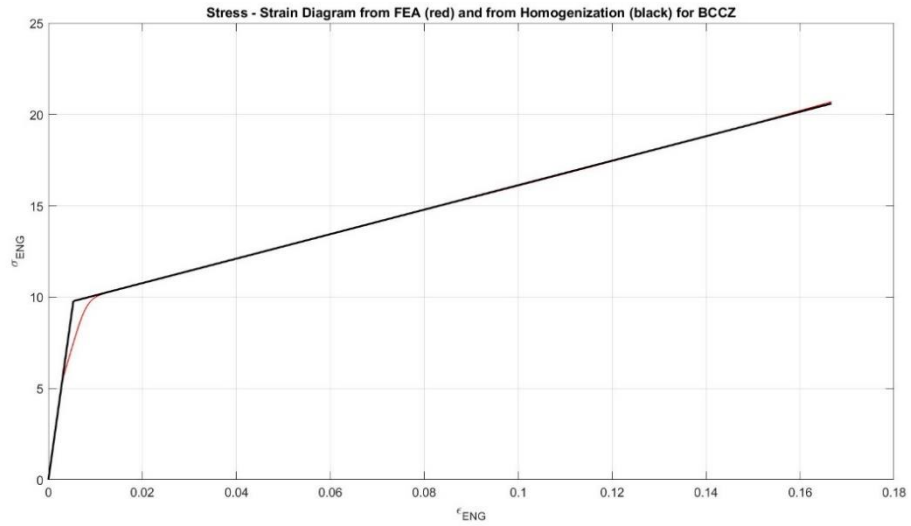

Figure 112: stress – strain diagram obtained using the homogenization process and the original one (*bccz*).

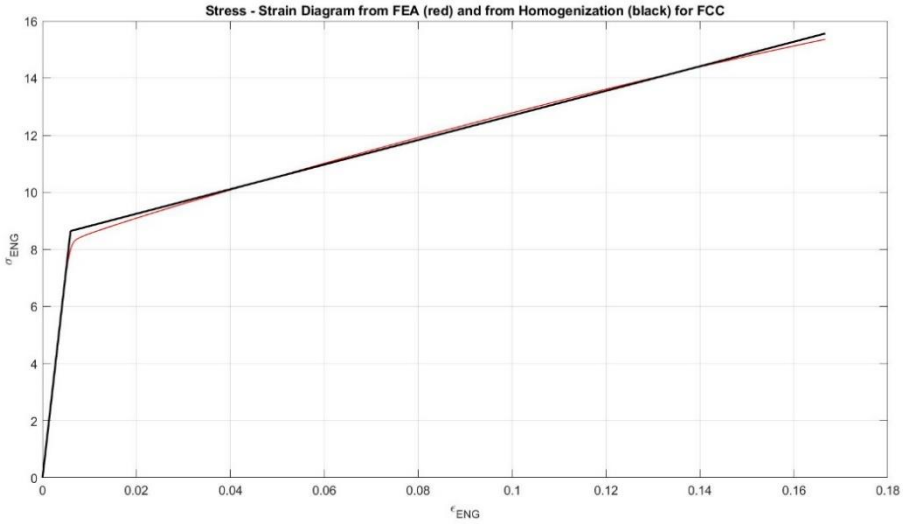

Figure 113: stress – strain diagram obtained using the homogenization process and the original one (*fcc*).

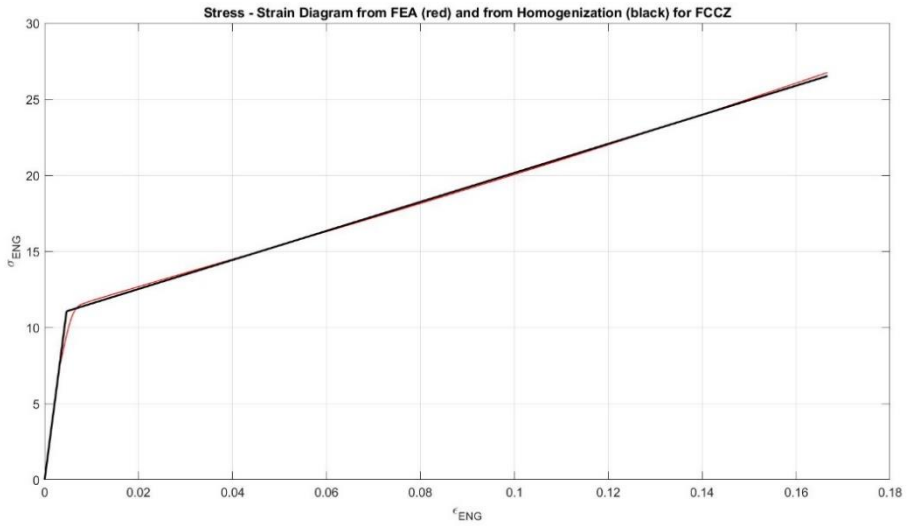

Figure 114: stress – strain diagram obtained using the homogenization process and the original one (*fccz*).

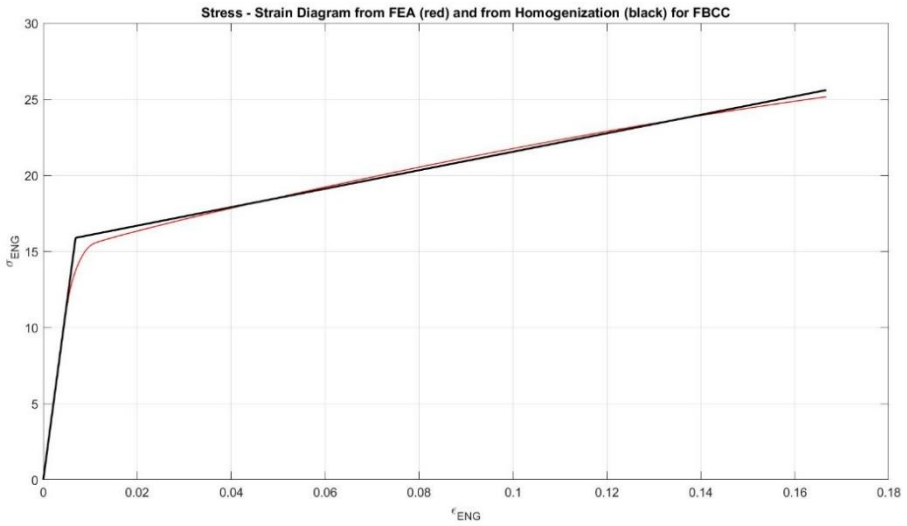

Figure 115: stress – strain diagram obtained using the homogenization process and the original one (*fbcc*).

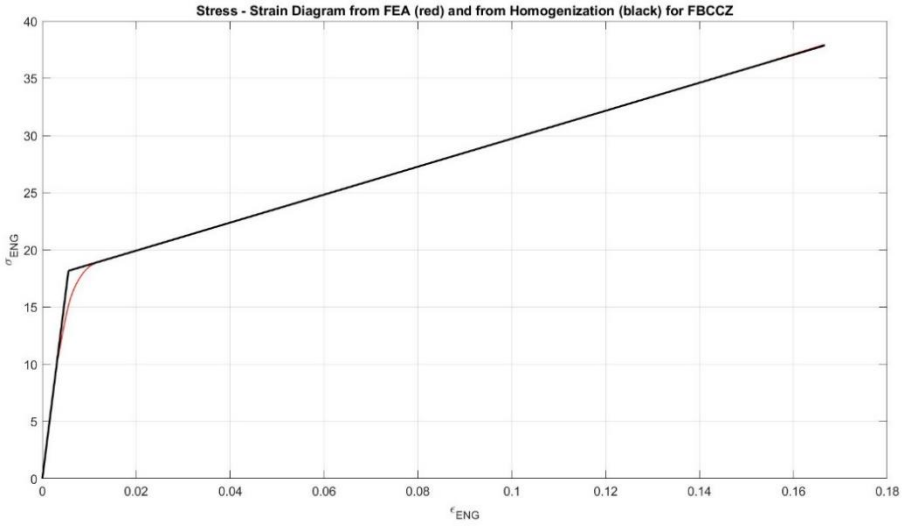

Figure 116: stress – strain diagram obtained using the homogenization process and the original one (*fbccz*).

Properties are summarized in Table 14.

Cell	ρ	E	E_T	σ_Y	ε_Y	m
	g/cm³	*MPa*	*MPa*	*MPa*	*/*	*g*
BCC	0,19719	828,62	13,88	7,12	8,59E-03	0,0053242
BCCZ	0,22293	1838,38	67,02	9,78	5,32E-03	0,00601917
FCC	0,16146	1446,31	43,06	8,64	5,98E-03	0,0043594
FCCZ	0,18580	2366,66	95,40	11,06	4,67E-03	0,00501653
FBCC	0,33884	2308,29	60,72	15,89	6,88E-03	0,00914877
FBCCZ	0,36306	3264,24	122,33	18,16	5,56E-03	0,00980258

Table 14: material properties obtained via homogenization (mass and density will be useful for multi-morphology simulations).

At this point there is have everything needed for the definition of the medium material. Density is evaluated based on the mass of a single cell (keep in mind the material selected is AlSi10Mg) and the RVE volume.

5.2 Applicability limits and deviations from the original model

Though the model can be very useful in making analyses more convenient and lighter, precaution need to be taken: limits of the model will be discussed and errors and deviation from the original model will be evaluated.

5.2.1 Applicability limits

Because of the assumptions made there are limits this model presents:

- *Isotropy*: in order to achieve a more accurate bilinear model, orthotropy has been set aside. That means a load direction has been preferred and that it is not possible to consider properties in other directions that are not the one considered in the first step of the homogenization process. In other words, this model works good for monoaxial load cases, that is sufficient for the analyses we need to carry on.
- *Poisson Ratio set to zero*: with this strong assumption we are basically not considering at all stress development in any other direction that is not the loading one. Also, G modulus is automatically defined once E and ν are established, incurring in a not realistic G modulus. Once again, assuming we are going to carry only monoaxial loading simulation, G loses its importance since there is not a shear configuration generation in the way we are modelling loads.
- *Plastic segment slope is constant*: the definition of the E_T modulus, that lies in the slope of the plastic segment of the stress-strain diagram, is based on a limited number of datapoints where the last one coincides with an engineering strain equal to 0,1667 (where it has been decided to stop the FEA simulations). That means we are assuming that the slope of the plastic segment is constant until the limit displacement the elements that are going to be used for the medium are capable of (that would theoretically be the densification point). The fact the slope of the plastic section is constant is not necessarily true, on the contrary it is evident how *bcc* plastic segment is varying slope going on with strain for example; the problem is that it has to be defined a finite point where to stop for numerical considerations and it has been arbitrary decided to stop at the mentioned strain level, since it is sufficient to gather valid and coherent data for the process. Further investigation could lead to the definition of a multilinear model

instead of a bilinear one for better accuracy. Also, it is impossible with this simple model to actually define a densification point where the element would have to stop absorbing energy in an efficient way.

- *Neglection of a small part of energy absorption*: looking at the diagrams going from figure 111 to 116 it is evident how areas under the curves, that is EA, are different going from the original stress-strain diagram to the bilinear one. That is because the yield transition in the FEA happens consequentially and not at a precisely defined point as in this model. Also, the fact the R^2 factor is not always equal to 1 means that there are differences between the two plastic curves as well. Table 15 shows percent errors for EA (until strain 0,1667) for every cell, and it is evident how the error tends to decrease going from bending dominated behavior to stretching dominated one as well as cells with vertical struts: it can be stated that more the struts tend to be aligned with the load direction, more the stress-strain diagram from FEA will tend to the bilinear one. The errors evaluated in table 15 refer to the ones between the original stress-strain diagrams and the bilinear model, that are different from the errors evaluated in the next paragraph: these are in fact the one evaluated between the original stress – strain diagrams and the ones obtained from results with models making use of the medium material.

Cells	*BCC*	*BCCZ*	*FCC*	*FCCZ*	*FBCC*	*FBCCZ*
EA % Error	2.52 %	1.34 %	1.88 %	1.31 %	1.45 %	0.89 %

Table 15: EA percent errors.

Besides the considerations about the limit of the model to respect in order to achieve valid results, considerations about applicability can also be made: while there could be lack of information about stiffness due to estimated errors and the way the yield stress is defined, the model can be valid for analyses where the main property to consider is energy absorption. Being able to describe the plastic field (in contrast with classic strain energy homogenization process) where most of the EA lies, it can be predicted results will be valid in a certain range of approximation, as next paragraphs will show.

5.2.2 First verification tests set

A first validation test has been performed as follows: six cubes of the same dimensions as the RVE we have been considering up to now (3x3x3 mm) have been generated and bilinear models for the six cells have been applied to each one of those. At this point lower surfaces have been fixed while a -0,5 mm displacement has been applied on upper surfaces in the load direction (simulation setup in figure 117).

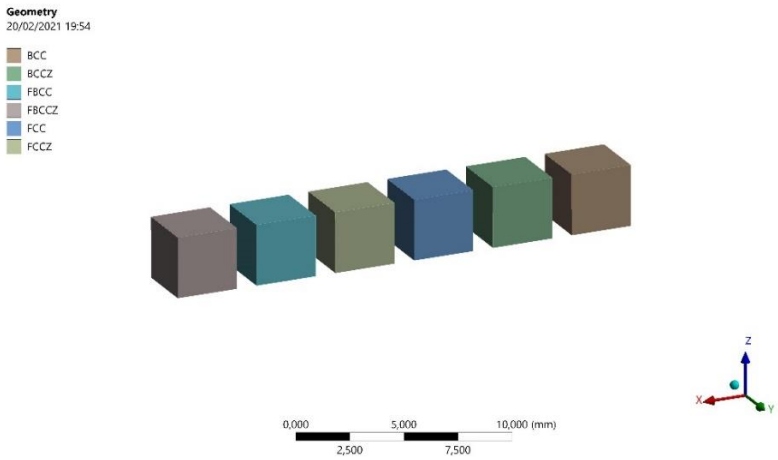

Fig. 117: simulation setup for homogenization process validation.

What we need to see in this validation is if stress levels obtained with this model are somehow comparable with the ones achieved with the starting simulations. At first the cubes are modelled with one element each: important results are obtained from the point of view of Equivalent Von Mises stresses (used because this stress is the combination of stress contributions in different direction, therefore if this stress is equal to the original one, it means the model is developing stress in one direction only) that are quite similar with the ones expected. In figure 118 Equivalent Von Mises stresses are graphed together with strains. Even though final stress levels are a bit smaller than the ones expected, the behavior and magnitude are still respected.

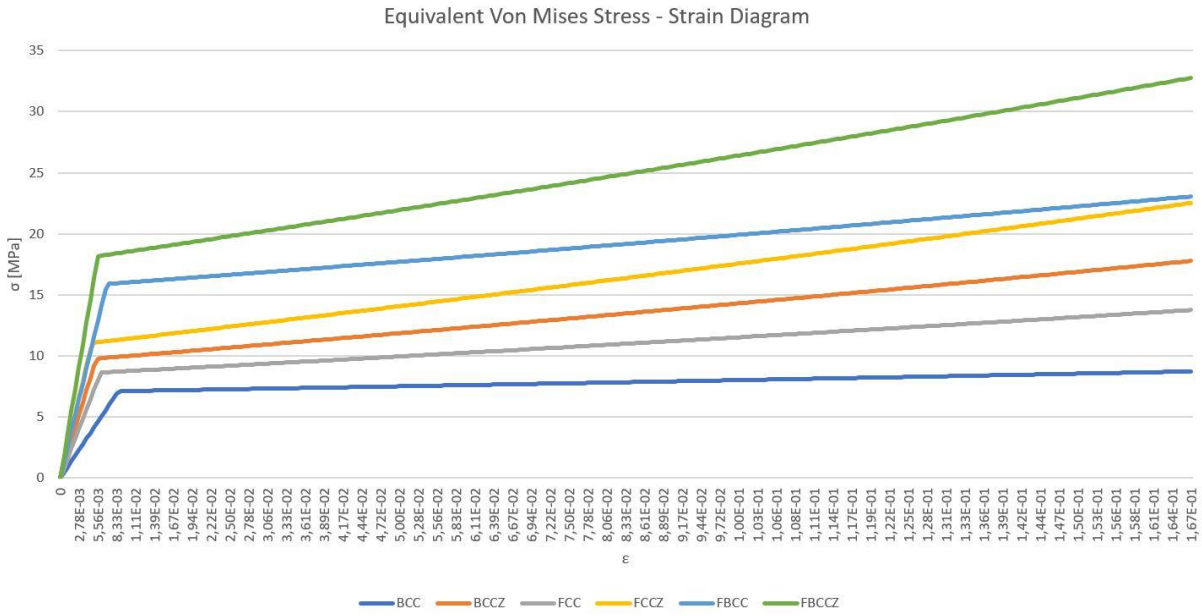

Fig.118: Equivalent Von Mises Stress – Strain diagram from validation test.

Modelling the RVE using only one element it does not offer good results if force reaction is transformed into engineering stress. A more accurate force reaction probing is possible if the mesh is finer: modelling the RVE with 0,3 mm solid elements (10 times smaller than before), a new simulation

has been performed, probing the forces on the upper surfaces and transforming them into engineering stress in order to create stress – strain diagrams (fig.119), useful for comparison.

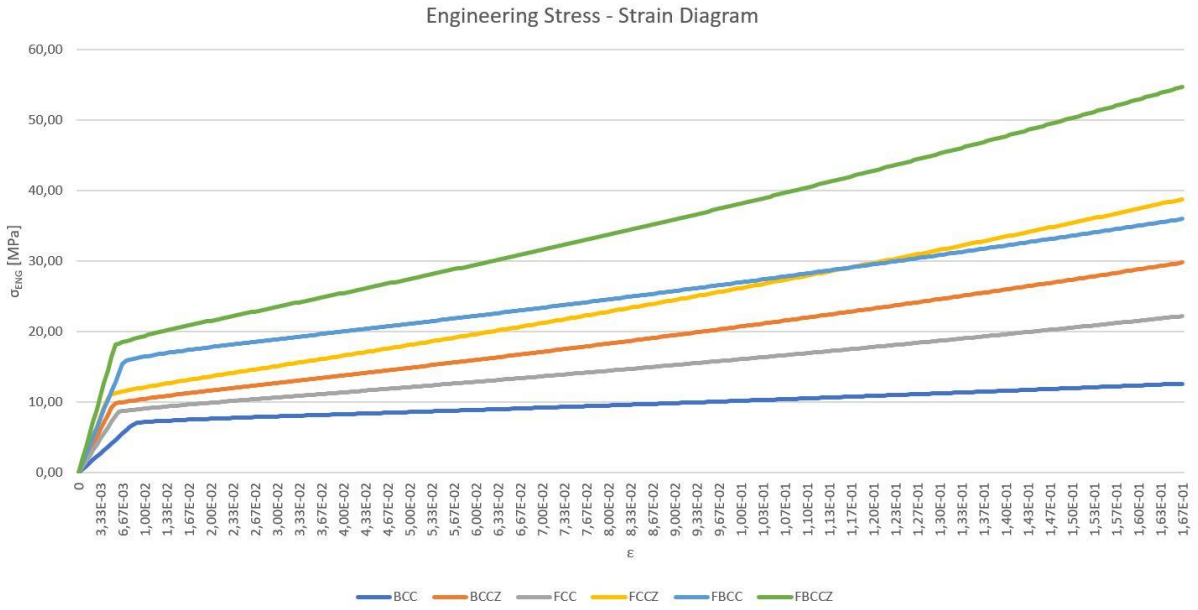

Fig. 119: Engineering Stress-Strain diagram from the second validation test.

For both set of diagrams obtained it is possible to evaluate the EA error (once again until strain equal to 0,1667), in order to consider the problem from a quantitative way; errors are evaluated as deviation from the original stress – strain diagrams (table 16).

	BCC	BCCZ	FCC	FCCZ	FBCC	FBCCZ
% Error for first validation test (using Equivalent Von mises stress)	5.87 %	10.85 %	9.17 %	12.19 %	8 %	10.76 %
% Error for second validation test (using engineering stress from force reaction)	17.05 %	25.86 %	23.56 %	27.72 %	21.42 %	25.53 %

Table 16: EA percent errors

It is evident how the first way of reading results using Von Mises stress is better and more accurate than the second one. There are moreover two advantages in using this way: first, simulation can be extremely lighter with respect to the second way that needs a finer mesh to get acceptable results; second, being stress levels reached using Von Mises stress as output lower than the one of the bilinear model, this way is also conservative in contrast to engineering stresses of the second validation test that are higher than the original ones.

5.2.3 Second verification tests set

Using Equivalent Von Mises stress as output is therefore conservative, as stated in the previous paragraph; by the way all of the considerations made up to now are valid until a defined strain, that is 0,1667. What is necessary now is to evaluate how far the model can go committing a neglectable error. To do so, the full topology simulations (the ones where the geometry of the cell is totally defined and that have been used to obtain the homogenization raw data) have been pushed to the limit, where the limit is the highest strain possible before incurring in error depending on the excessive distortion of elements: these distortions tend to create excessive energy errors and unusual peak stresses. Simulation configuration is the same as the one described in previous reports. Maximum strain possible for the topologies selected is 0,4 (for some of them it is 0,5 but the same limit is used for all of the simulations).

In order to evaluate differences between results from the homogenized material simulations and the ones from the full topology simulations, a compression test using the medium material for each cell has been performed, where one cell is modeled with one element. Crashing tests with full topology model are defined as in chapter 2, while for the medium material model simulations, Equivalent Von Mises stress has been used as output. Figures 120-125 present comparisons between stress – strain diagrams obtained from the two models.

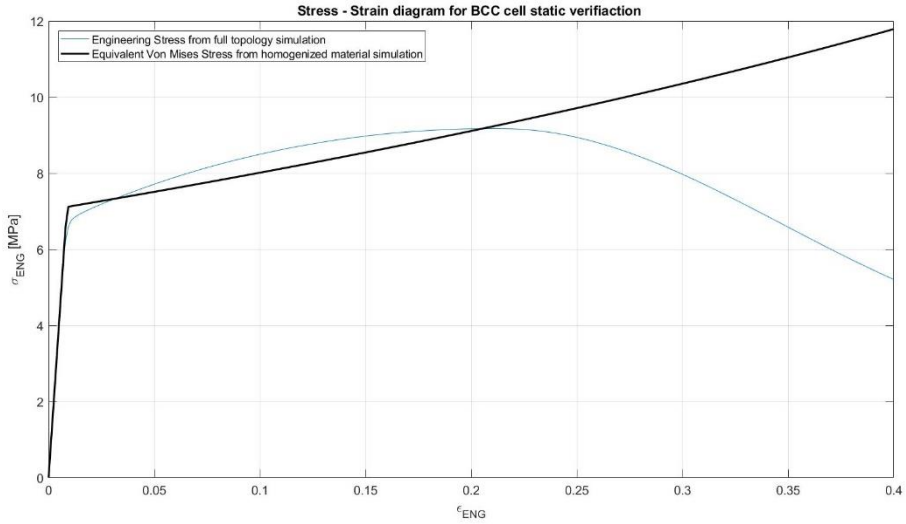

Figure 120: Stress – Strain diagrams for the homogenized material model and the full topology model for *bcc*.

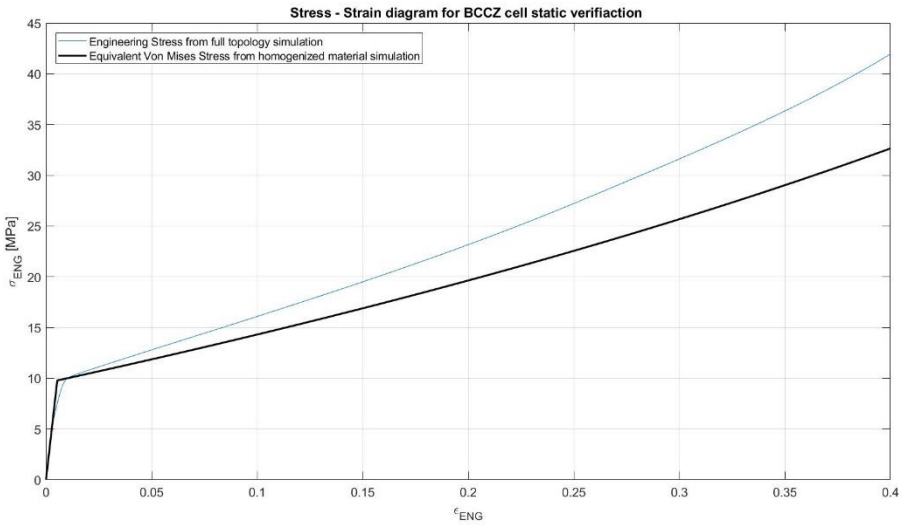

Figure 121: Stress – Strain diagrams for the homogenized material model and the full topology model for *bccz*

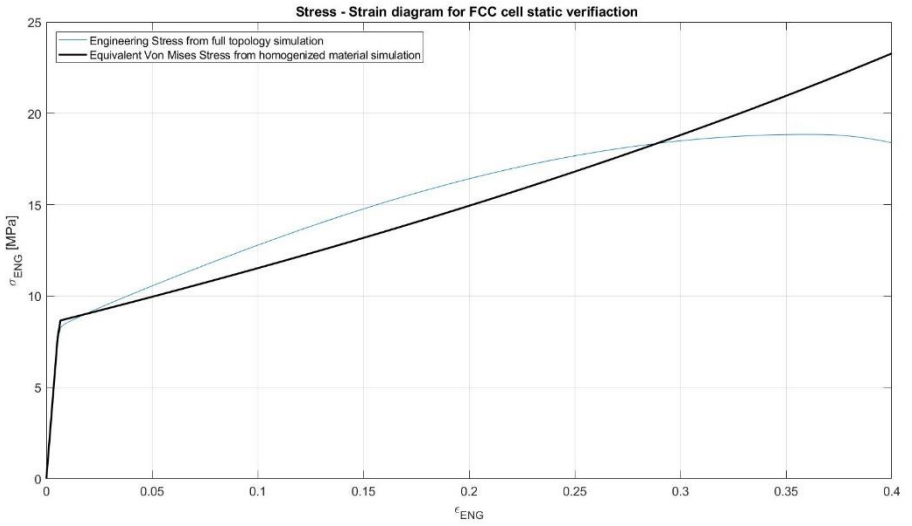

Figure 122: Stress – Strain diagrams for the homogenized material model and the full topology model for *fcc*.

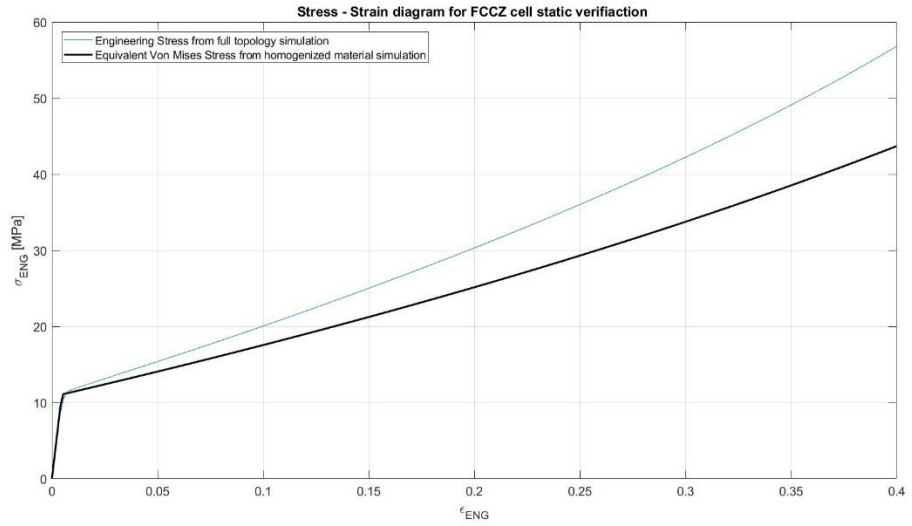

Figure 123: Stress – Strain diagrams for the homogenized material model and the full topology model for *fccz*.

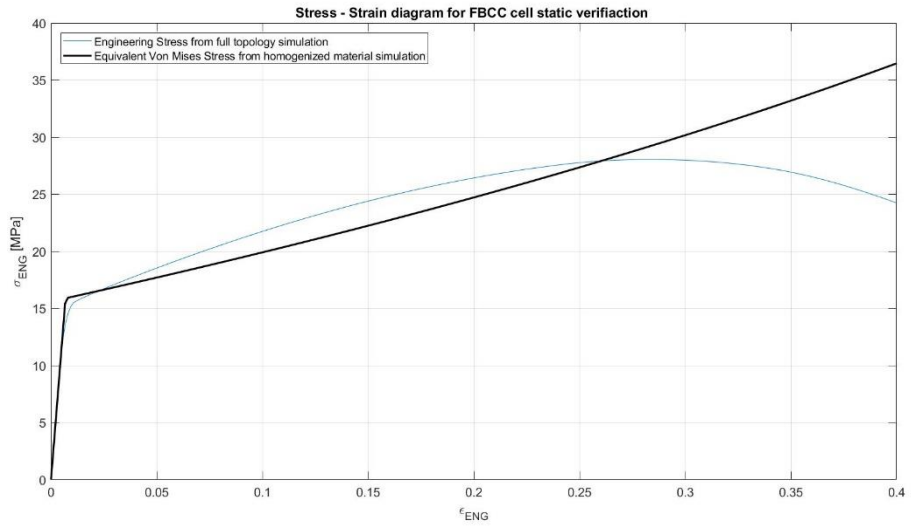

Figure 124: Stress – Strain diagrams for the homogenized material model and the full topology model for *fbcc*.

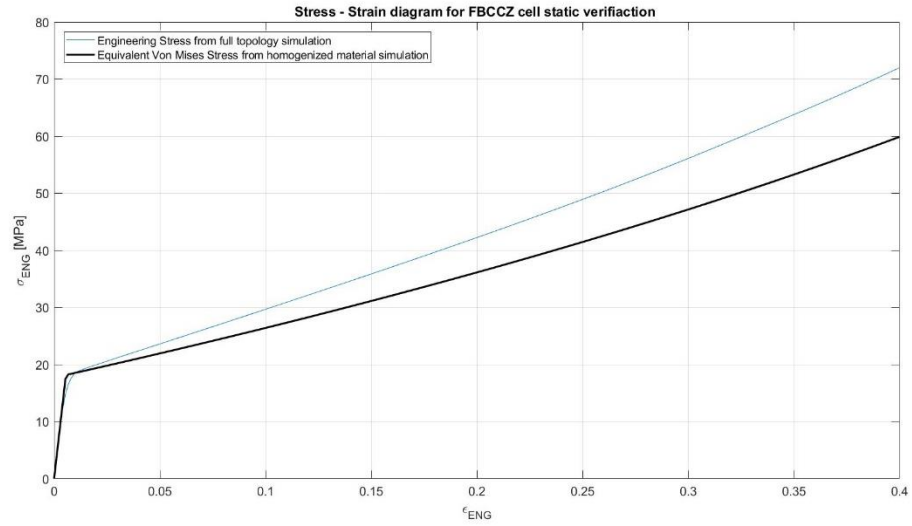

Figure 125: Stress – Strain diagrams for the homogenized material model and the full topology model for *fbccz*.

Cells where vertical reinforcement is absent show a qualitatively different diagram from the one referring to the cells with Z struts. Diagrams presenting data about *bcc*, *fcc* and *fbcc* from full topology model show a decrease in stresses with increasing strain: this is something that of course the medium material model is not able to take care of and this will be therefore evident once the deviation will be evaluated. The stress fall happens right after a maximum, and that maximum depend on the cell we are considering. Bending dominated *bcc* presents this maximum before stretching dominated *fcc*, and this was expected since stiffness in stretching dominated cell is always higher: even though here we are talking about residual stiffness after the yielding point. While *fbcc* shows the maximum almost at the same point as *fcc*.

For reinforced cell the behavior is totally different and more in line with homogenized model results, though error is still present. After the yielding point that visually happens almost at the same point

for both models, there is a plastic regime where stress is not linear but suffers a hardening process. It is possible to consider stress stiffening also in the medium material model by simply activating "Large Displacement" option in the Ansys analysis settings. This option offers a more realistic stress path than the simple bilinear one, which is by the way used for the definition of the bulk medium material itself.

At this point it is possible to evaluate deviations. In first place, pure and percent deviations stress are calculated with these simple expressions:

$$\sigma_{DEV} = \sigma_{FT} - \sigma_{MM}$$

$$\sigma_{DEV}^{\%} = \frac{\sigma_{FT} - \sigma_{MM}}{\sigma_{FT}} * 100$$

Where σ_{FT} is the stress for the full topology model, while $\sigma_{MM}$is the stress for the medium material model. Percentage is evaluated relating the stress deviation to the full topology model stress: figures 126 and 127 shows deviations – strain diagrams. Deviations are not calculated using absolute values in order to take account of conservativeness of reinforced cells.

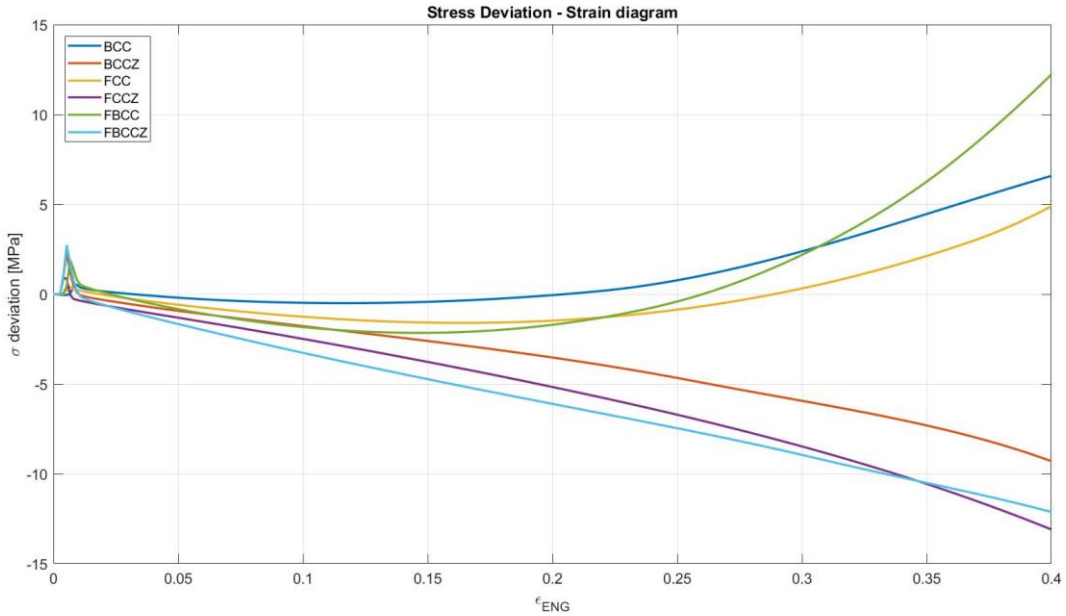

Figure 126: Stress deviations – Strain diagram

After a first peak for every cell that recalls the stress discrepancy during the yielding process (which is totally neglectable for every cell), levels tend to define different behaviors according to the fact that the cell is reinforced or not.

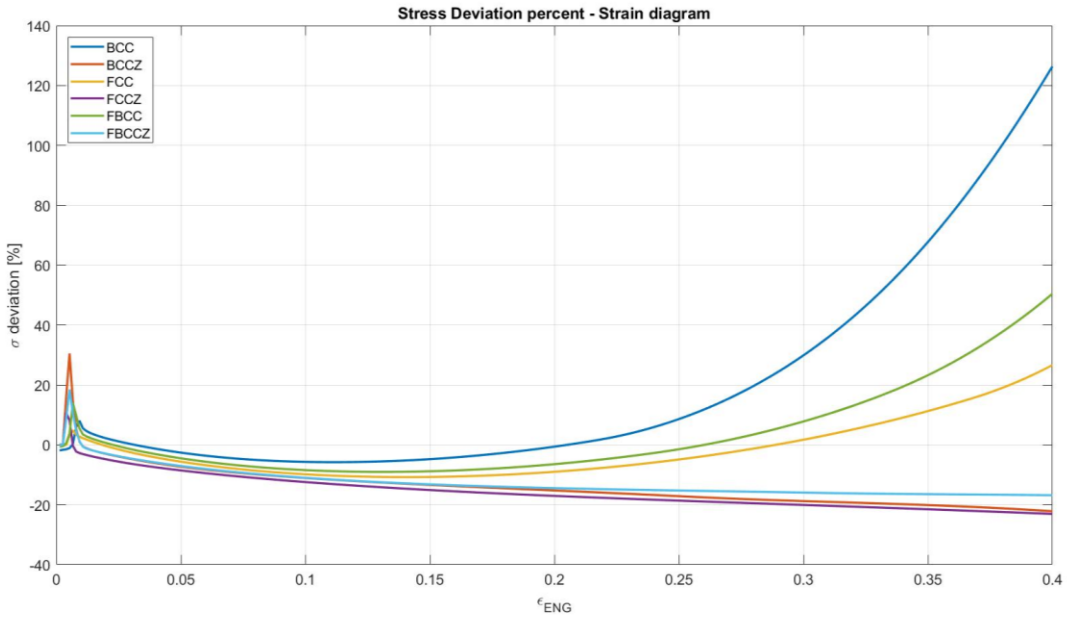

Figure 127: Stress deviations percent – Strain diagram.

For non-reinforced ones, right after a first minimum (that happens after the yielding point, where stresses merge) there is a strain range where deviation decrease, going below zero: that happens because of the stress differences in the first part of the plastic regime. The deviation level reached in this range is by the way acceptable (we are below -20% of error, maximum for *fcc*). A second zero is following this cited range, and here is where stresses merge once again before the final fall. After this zero, deviations increase almost exponentially: and here is where the biggest error is registered because the behavior of the full topology model and the one of the medium material model diverge totally. This final divergence can be well seen in the final part of the percent stress deviation – strain diagram where *bcc* shows more than 120% error around 40% of strain.

Reinforced cells, after the first peak coinciding with yielding, present a constantly falling deviation: minimum reached is by the way around -25% maximum at 40% compression. After the first peak in the positive section of the deviation percent due to yielding, the trend for these cells is to be conservative (being the stress levels reached for the medium material model always lower than the actual stresses).

Besides deviations evaluated on stress levels, most important considerations have to be made on Energy Absorption. EA – Strain diagrams, shown in figure 128 and 129, have been generated using numerical integration.

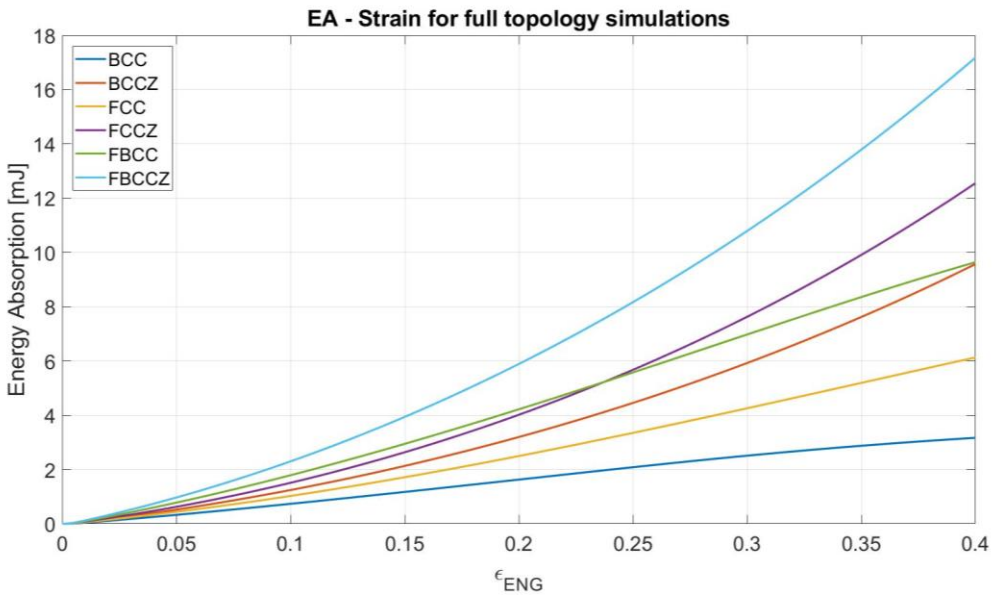

Figure 128: EA – Strain diagrams for full topology model.

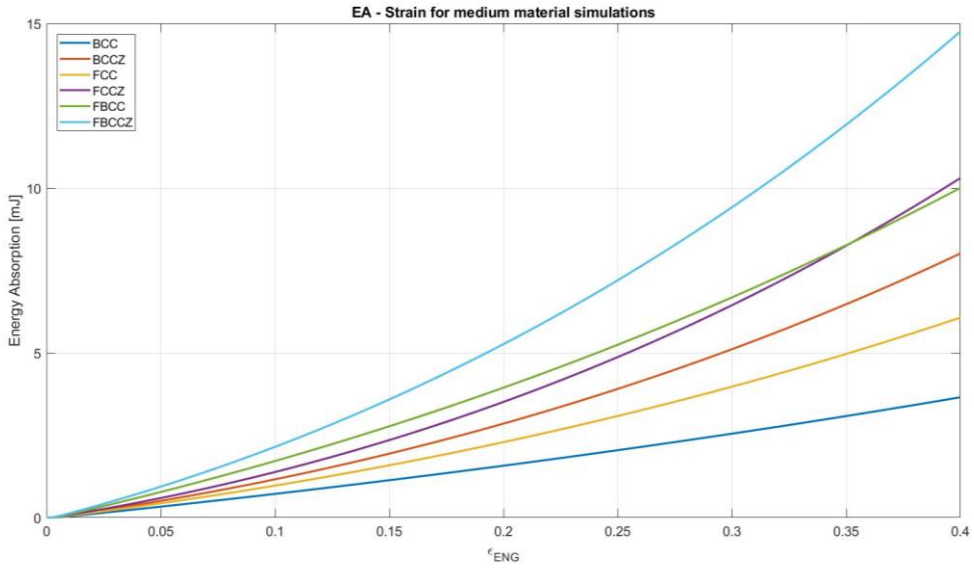

Figure 129: EA – Strain diagrams for medium material model.

Qualitatively diagrams are very similar, main differences are between EA level reached. EA deviations are therefore evaluated, both as pure and as percentage (figures 130 and 131) with the following expressions:

$$EA_{DEV} = EA_{FT} - EA_{MM}$$

$$EA^{\%}_{DEV} = \frac{EA_{FT} - EA_{MM}}{EA_{FT}} * 100$$

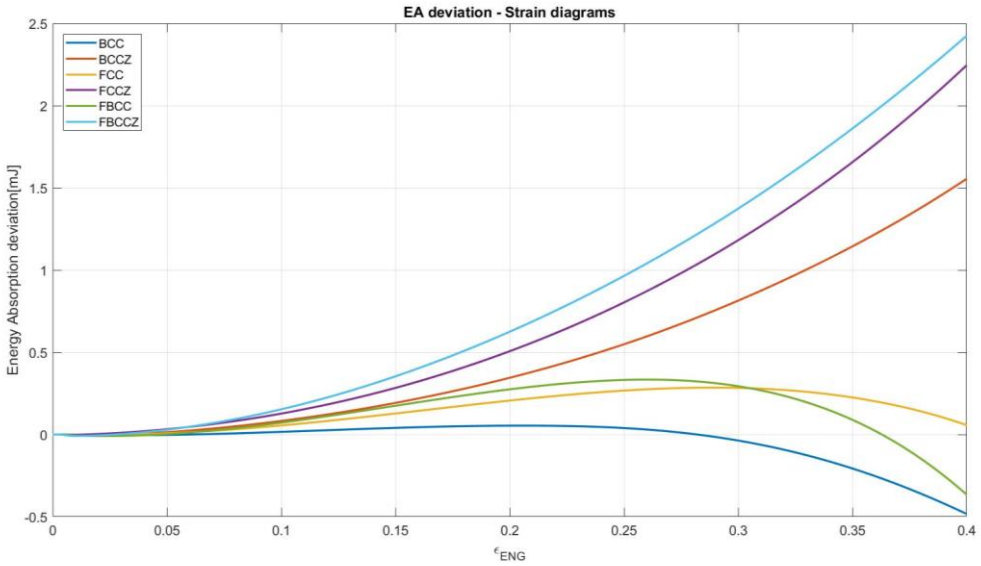

Figure 130: EA deviation – Strain diagrams.

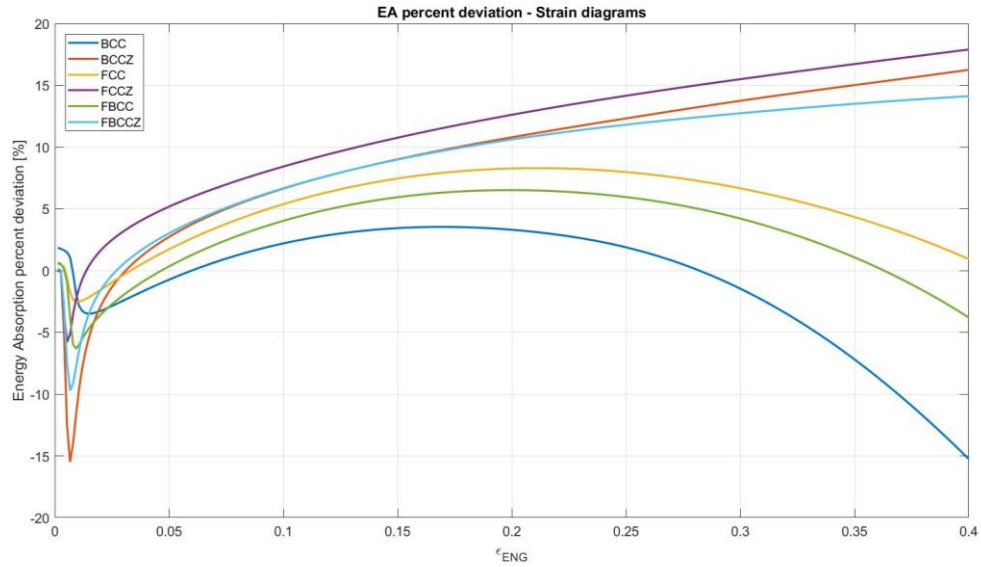

Figure 131 : EA percent deviation – Strain diagrams.

Though deviations diagrams are similar between EA and stress, data they are delivering are quite different. For non-reinforced cells there is a starting rise in deviation, a following zero and then a fall. This time the zero is not showing the point where the stress merge in the plastic domain, but it is the point where the area under the curve of the two model is the same. For every cell, in the percent diagrams there is a minimum at the beginning: it simply is the deviation in the yielding point and it can be neglected, also because there is no evidence of this peak in the pure deviation diagram.

For reinforced cells the deviation always increases presenting no minimum after the yielding one, but the error is limited around 20% (maximum for *fccz*) for max strain possible (40%).

For a final decision to define the strain limit when using the medium material model, the following diagram is used (fig. 132).

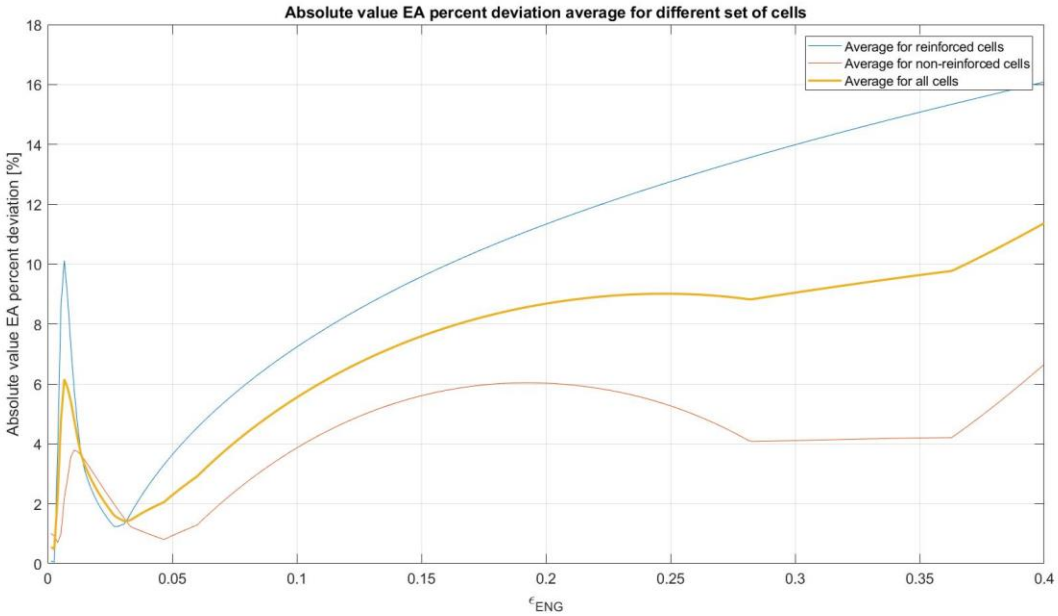

Figure 132: EA absolute value percent deviation for different cells set.

Absolute values have been used in order to evaluate a general error with regards to all of the cells, since the same strain limit has to be defined for all of them. For non-reinforced cell, the error can be limited at an average of 6% within a range where the upper limit is around 0,3 – 0,35 strain. For reinforced cells instead, there is no range where the error can be limited since the average keep growing with no minimum (except the one coincident with the modeled yielding point): the error at 0,3 strain is around 15%, so it is still limited and acceptable. Summing up all the cells for a general average, we can see that 0,3 seems to be the best strain if we want to limit the total general error around 9%. In order to perform multi-morphology analyses that can in the end be compared, a unique strain, that will be translated into a displacement, has to be defined for all of the analyses to be performed: 0,3 is the best candidate.

6 Multi-morphology design

Optimization over lattice structures is a strong tool to obtain components that can fit multi-functional aims. Based on topology modification in order to achieve particular request, optimization of course plays with shapes the world of lattices offers and generates either variations of classic geometries, as it can be seen in [51], or multi-morphology designs, the ones this study is more interested in; these are based on boundary conditions and objectives depending on the analysis requests. In most cases, such designs are coupled with computational micromechanics and homogenization methods in order to make analyses more convenient and ideal for optimization solvers. Literature is rich with such investigations: in [52], a mix of homogenization and topology optimization has been employed for a cantilever beam design. These methods can also be used for grading designs, for example [53], [54] and [55] present an investigation of optimized functionally graded structures. Different types of cells can be used in the same sample/component to achieve multi-morphology designs as well: the concept is very similar to graded structures, but there is the possibility to gather different properties and different behaviors in order to study effects of combinations; [50] is an example, where optimization process has been used as well.

In this investigation topology optimizations will not be considered, instead a multi-morphology design where sample configurations based on classical Voigt, Reuss and balanced panels models is presented. Samples will be analyzed using medium material models obtained from homogenization in chapter 5. Though models for configuration are well known, [56] has been inspiring in this design.

6.1 Design and analyses

6.1.1 Cells combinations and configurations

As said, multi-morphology investigation lies in studying the effects of the presence of different types of cell in the same sample or component. Combinations presented here make use of the cells that have been analyzed up to now: obviously, not all of the combinations possible have been explored but a selection has been made, for the ones that are particularly interesting. Three different groups are considered:

- Group I: the first group considers two combinations, that are *bcc* + *fcc* and the reinforced version *bccz* + *fccz*. It has been considered in order to study the effects of combination of stretching and bending behavior dominated lattices on energy absorption.

- Group II: this second group consists of four combinations that are *bcc* + *fbcc*, *fcc* + *fbcc* and their reinforced versions. The aim of this group lies in investigating the effects on EA of the mixture of bending/stretching dominated behavior (*bcc*/*fcc*) and a combination of lattices that is supposed to present both behavior at once (*fbcc*). The focus here is to determine if prevalence of a singular behavior can result into efficient achievements. Reinforced versions are always considered.
- Group III: last group presents three combinations: *bcc* + *bccz*, *fcc* + *fccz* and *fbcc* + *fbccz*. It basically wants to investigate effects of mixing simple lattices and their reinforced versions.

For every combination, feasibility has been considered with a simple consideration: it is always possible to accost cells in terms of jointing nodes at contact surfaces, because of the nature of the cells that have been selected. In this way there is no risk of presence of struts that are not connected to other ones in the interfaces dividing different types of cell.

Besides cell combinations this chapter wants to investigate, there is the need of finding ways to arrange these cells into configurations that could present advantages from the energy absorption point of view. Taking inspiration from [56], four different configurations have been developed:

- Configuration HA (horizontal-alternate): directly inspired by the classical Reuss model, it has been employed to study effects of series loading. For each HA configuration, two different versions have been investigated by simply changing the cell type of the first layer.

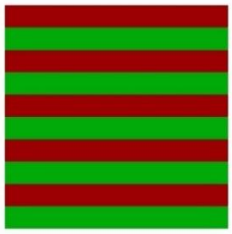

Figure 133: configuration HA.

- Configuration HD (horizontal-double): to be considered as a modification of the previous configuration, where only two larger layers are modeled. Based on previous consideration, two versions are present.

Figure 134: configuration HD.

- Configuration VA (vertical-alternate): inspired by Voigt model, it is a configuration useful for studying effects of parallel loading.

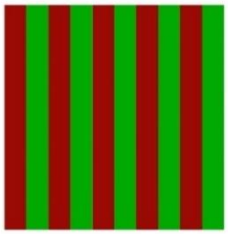

Figure 135: configuration VA.

- Configuration CA (circular-alternate): inspired by classical balanced panel model, it is a circular hybrid arrangement presenting symmetry along x and y axes. Two version are considered depending on the cell type present on the external shell.

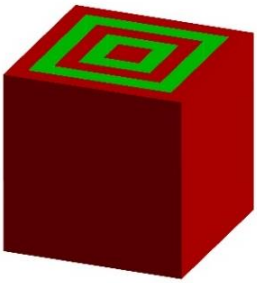

Figure 136: configuration CA.

Having nine cell combinations and seven configurations, sixty-three analyses have to be performed. Next paragraph shows the way these analyses are settled. Moreover, for every layer/shell there are 2 rows of cell, for advantaging continuity in terms of behavior.

6.1.2 Nomenclature and analyses

In order to manage the big amount of analyses to be performed, a nomenclature has been developed. Three to four indicators for each test are necessary, scheme is shown in figure 137:

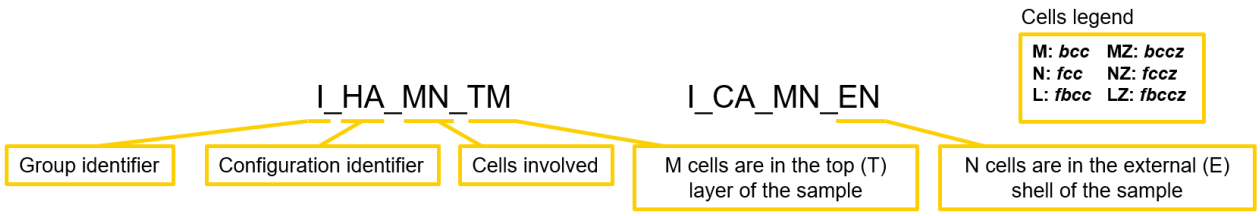

Figure 137: nomenclature used for simulations.

Last identifier is not necessary for VA configuration, presenting only one version.

Analyses settlement is very similar to the one used for crashing simulations presented in chapter 4. It has to be said that first of all, samples are modeled using medium material obtained from the homogenization process and that has allowed a huge saving of time. Every one of the sixty-three simulations performed lasted about 2 minutes. If analyses were to be performed modeling all of the aspects of the topology, they would have lasted days (if not weeks), and that is for sure the most advantageous characteristic of the homogenization process employed.

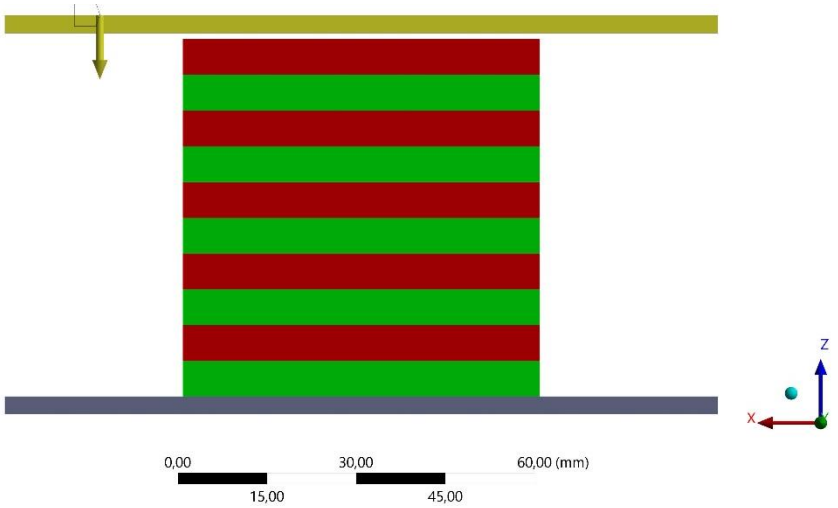

Figure 138: scheme of the simulations.

Dimension of the sample are 60x60x60 mm, consisting of 20x20x20 cells: a large number of cells, in fact, makes the simulations highly representative and also allow the generation of each of the configurations previously described. Once again there is a fixed plate and a crashing plate (crashing speed is equal to 200 m/s) connected to the sample using frictionless contact tool. As seen in the last chapter, strain equal to 0,3 is the limit for the homogenized material before incurring into excessive errors, that is the motivation why crashing is limited to 30%. Explicit code is used for simulations.

Three extra tests, where samples are modeled using only one cell type are also created (cells considered are *bcc*, *fcc* and *fbcc*), these tests will be used for comparison with multi-morphology designs.

6.2 Results and discussion

6.2.1 Results

First, stress – strain diagrams have been generated; they are shown in figure 139-148.

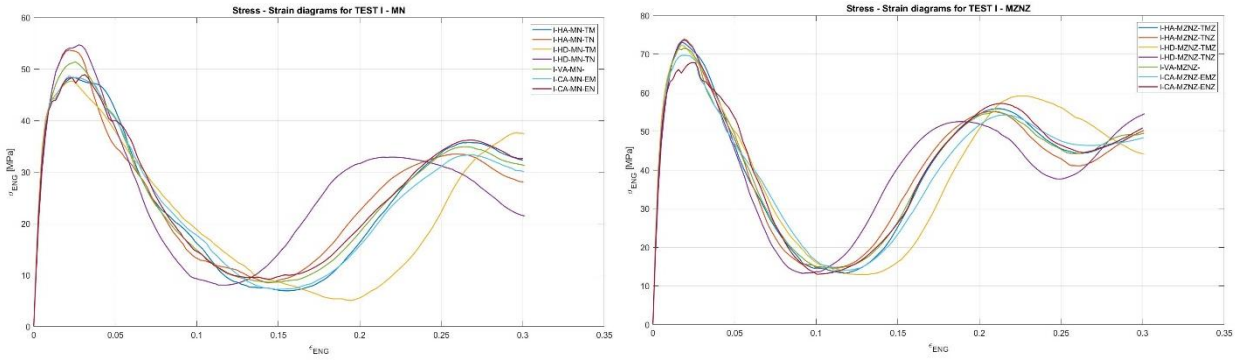

Figure 139-140: stress – strain diagrams for MN and MZNZ combinations.

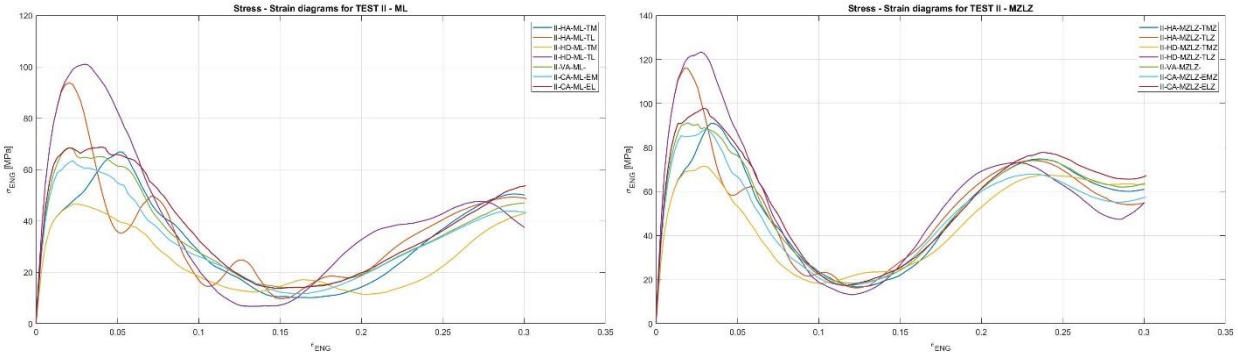

Figure 141-142: stress – strain diagrams for ML and MZLZ combinations.

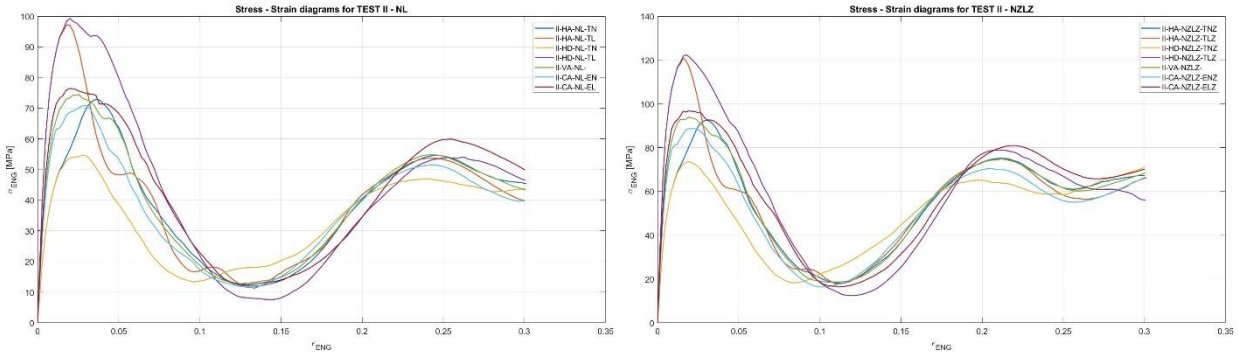

Figure 143-144: stress – strain diagrams for NL and NZLZ combinations.

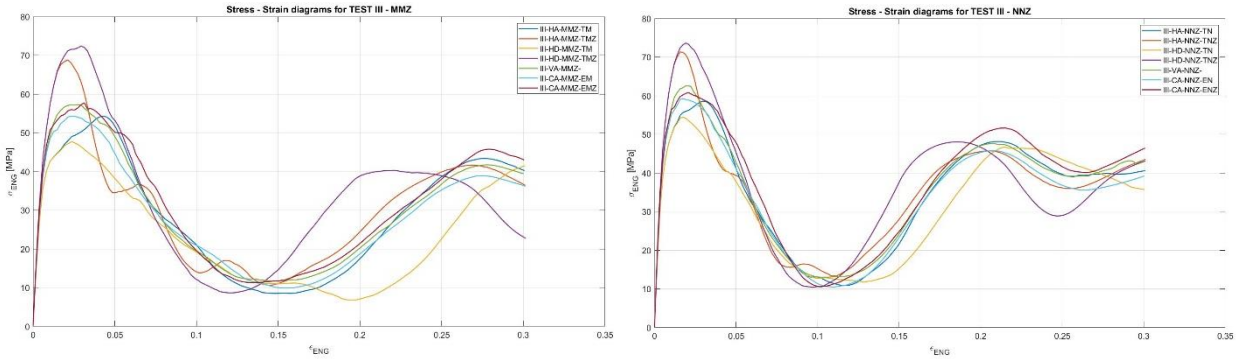

Figure 145-146: stress – strain diagrams for MMZ and NNZ combinations.

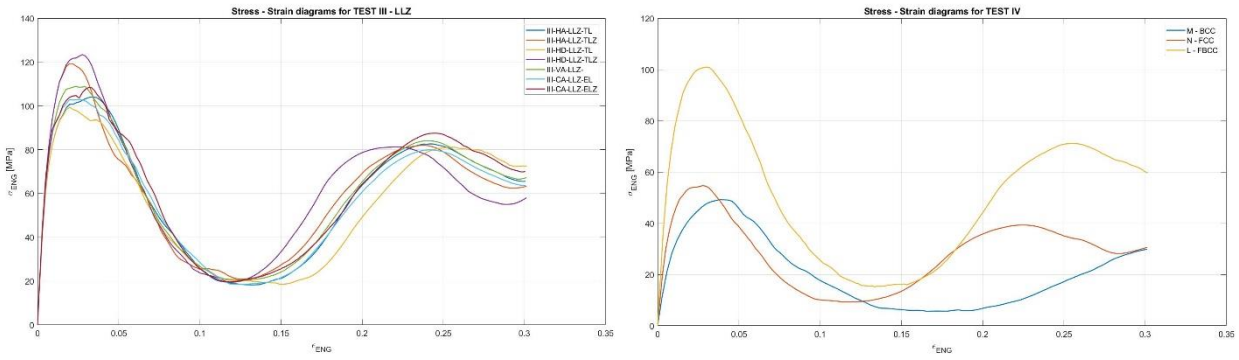

Figure 147-148: stress – strain diagrams for LLZ combinations and M/N/L extra tests.

Since samples are modeled using medium material, it is impossible to catch the typical multi-peak behavior, but the first peak still could be a useful information for the starting stiffness of the samples. Energy absorption can be obtained by integration. EA results are gathered in bar graphs to allow a better comparison. Showed EA levels (figure 149-158) are at 30% crushing.

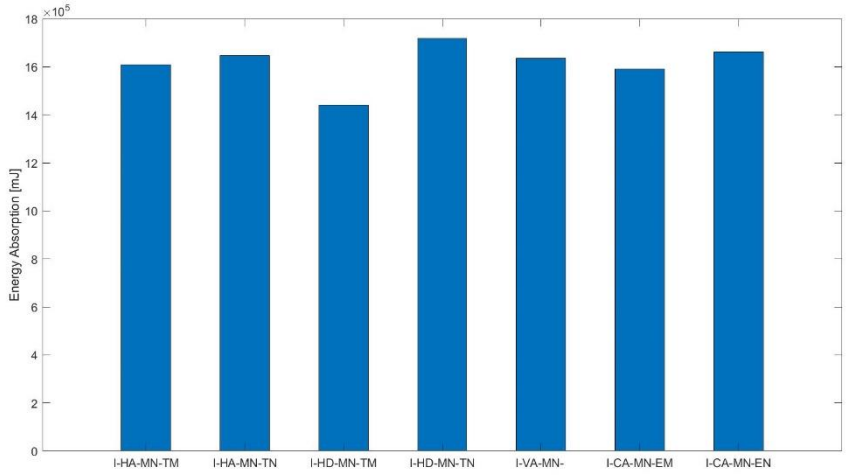

Figure 149: EA for MN combinations.

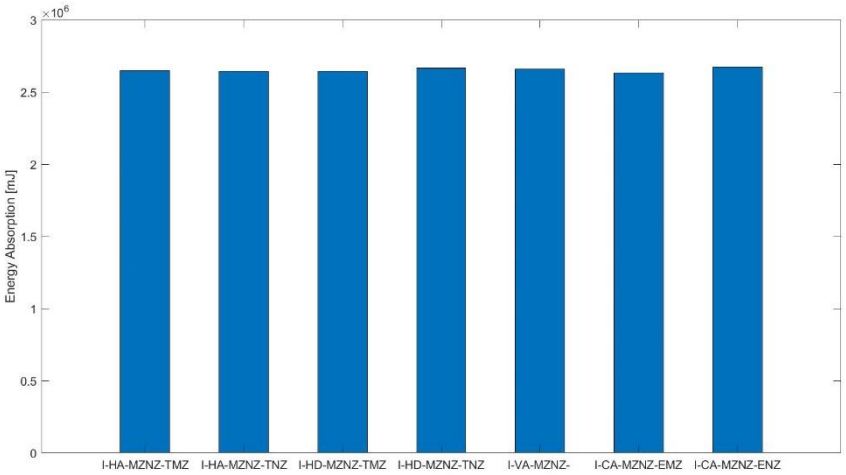

Figure 150: EA for MZNZ combinations.

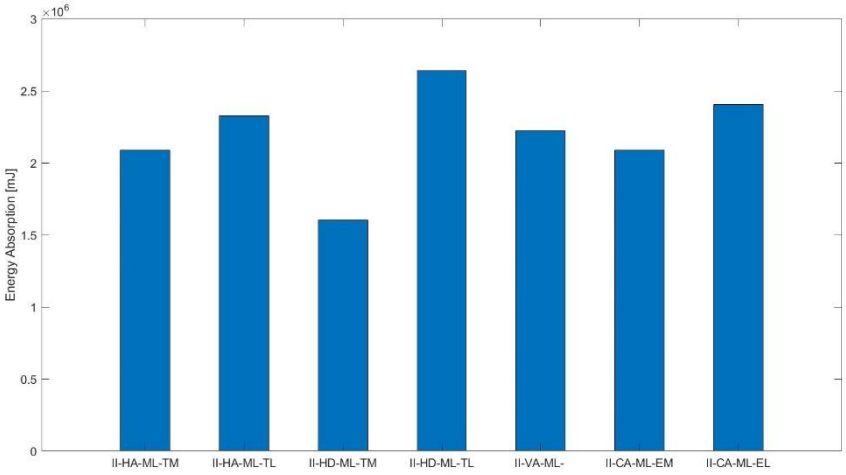

Figure 151: EA for ML combinations.

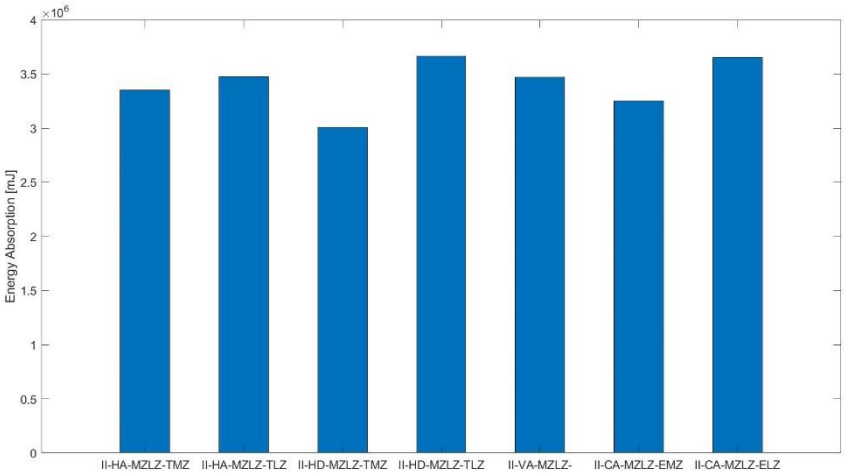

Figure 152: EA for MZLZ combinations.

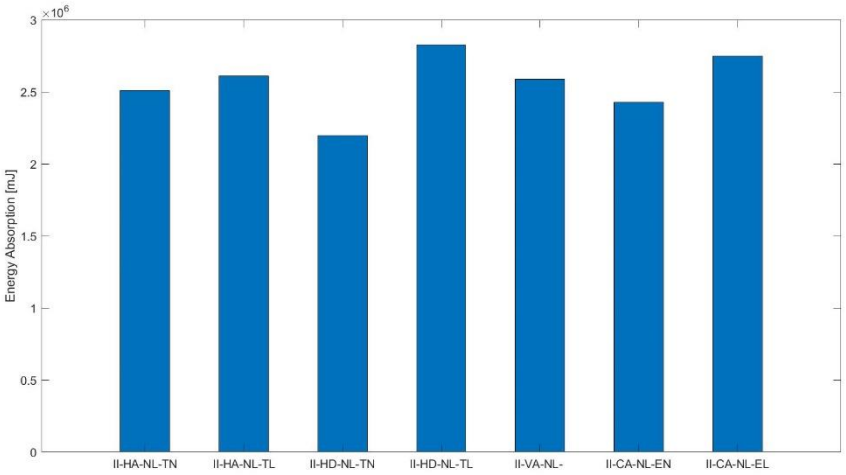

Figure 153: EA for NL combinations.

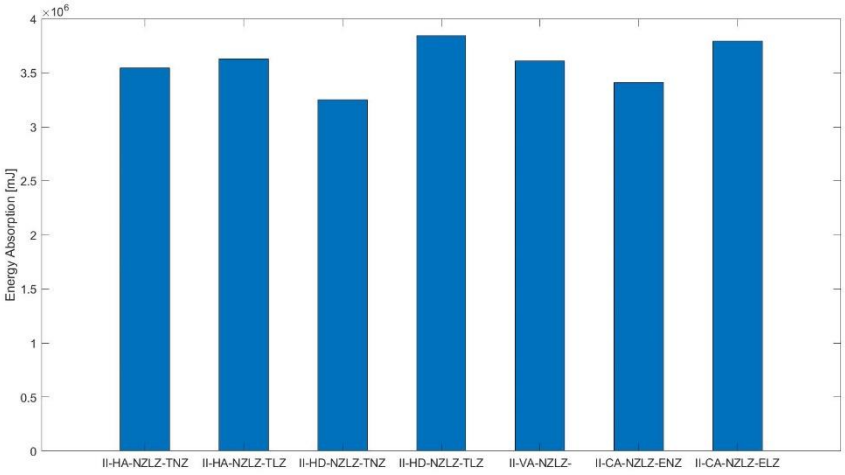

Figure 154: EA for NZLZ combinations.

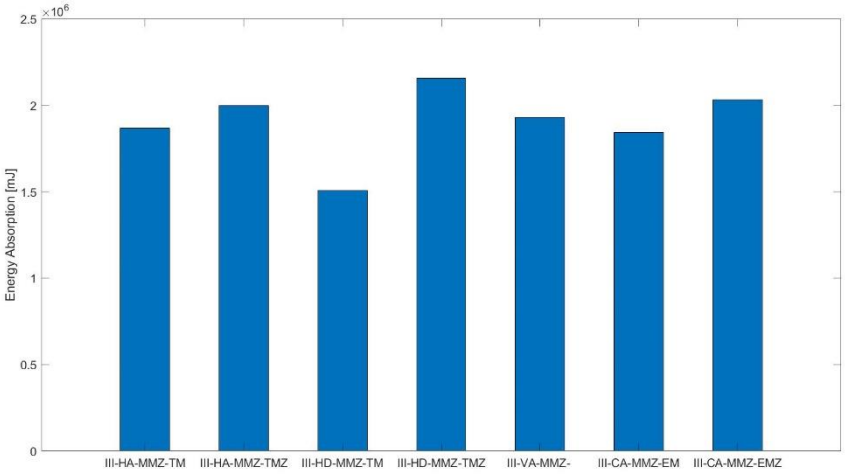

Figure 155: EA for MMZ combinations.

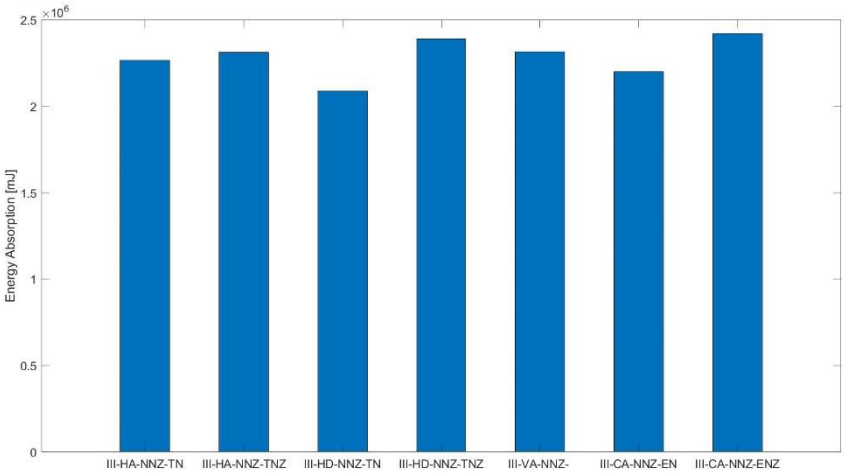

Figure 156: EA for NNZ combinations.

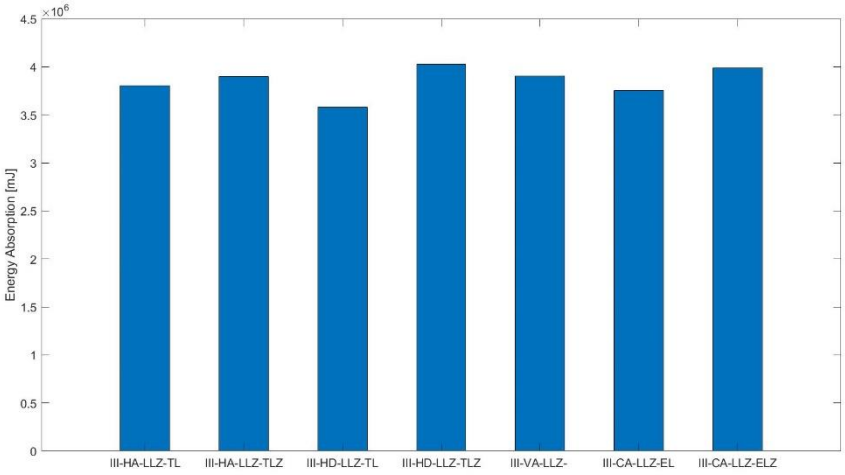

Figure 157: EA for LLZ combinations.

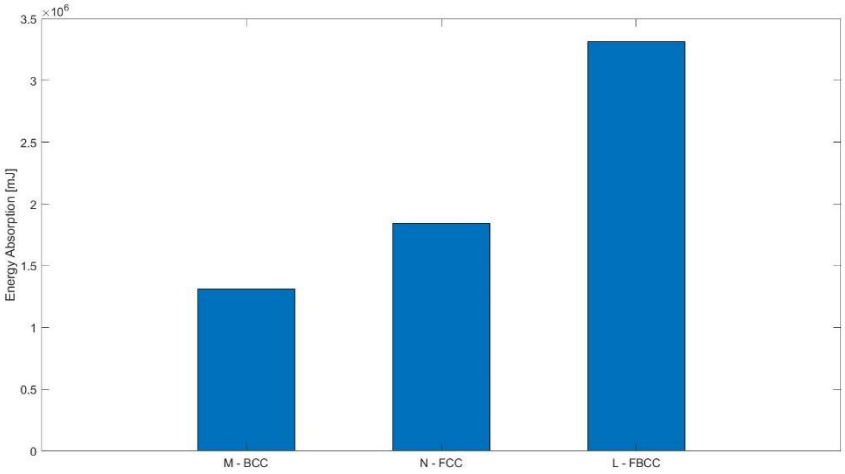

Figure 158: EA for M/N/L extra tests.

Sample masses have been evaluated and used for the calculation of specific energy absorbance together with EA. Results are shown in figure 159-165: while EA graphs are gathered according to groups and combinations, SEA results are instead gathered according to configurations in order to determine which combination is the more convenient.

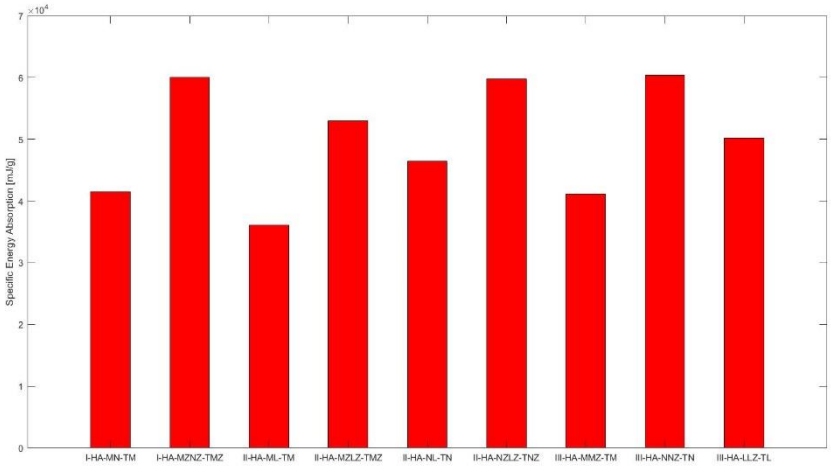

Figure 159: SEA for HA version 1 configurations.

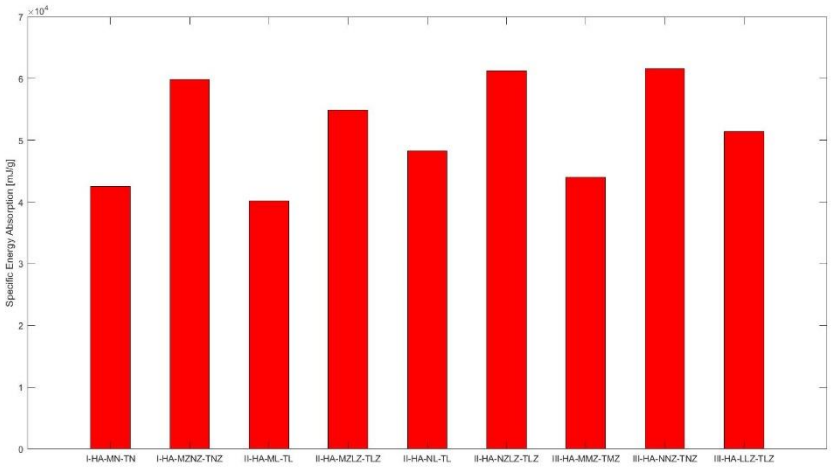

Figure 160: SEA for HA version 2 configurations.

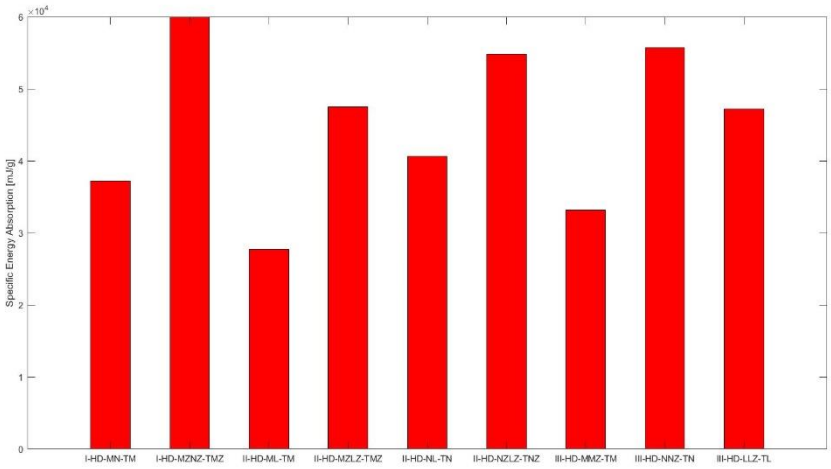

Figure 161: SEA for HD version 1 configurations.

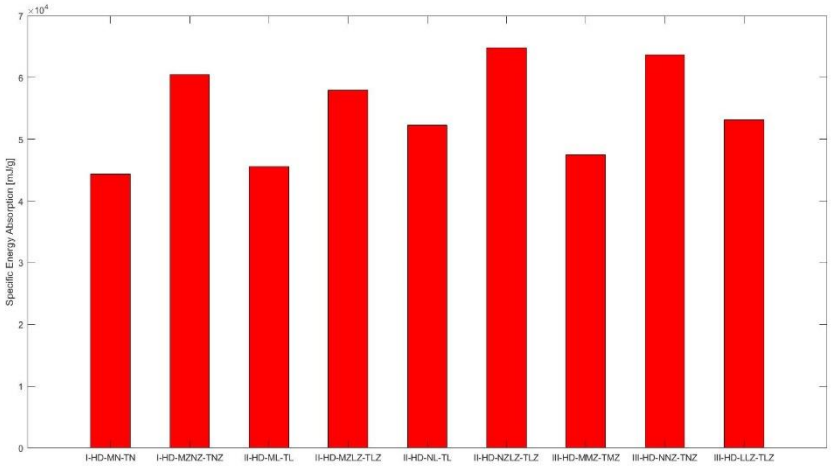

Figure 162: SEA for HD version 2 configurations.

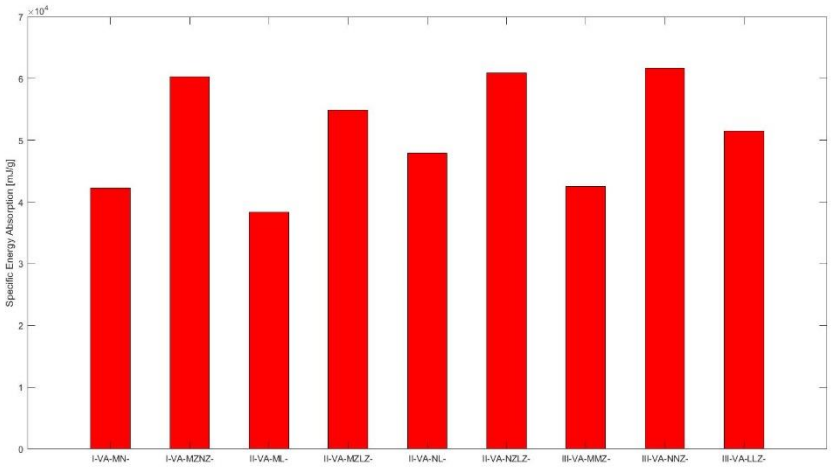

Figure 163: SEA for VA configurations.

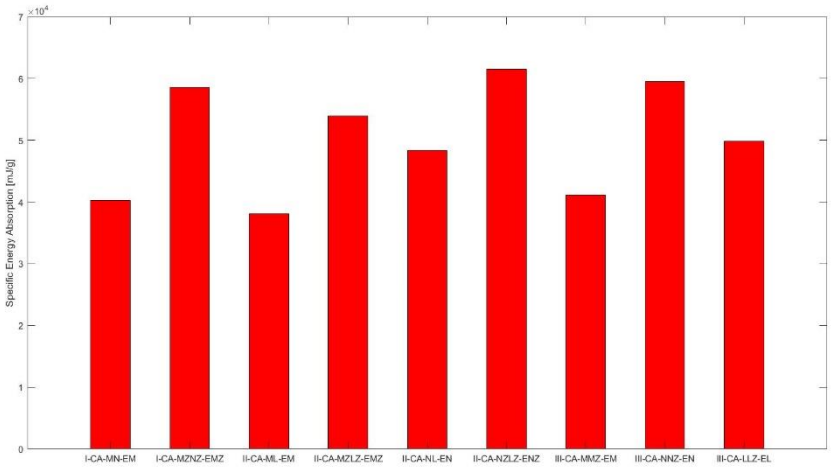

Figure 164: SEA for CA version 1 configurations.

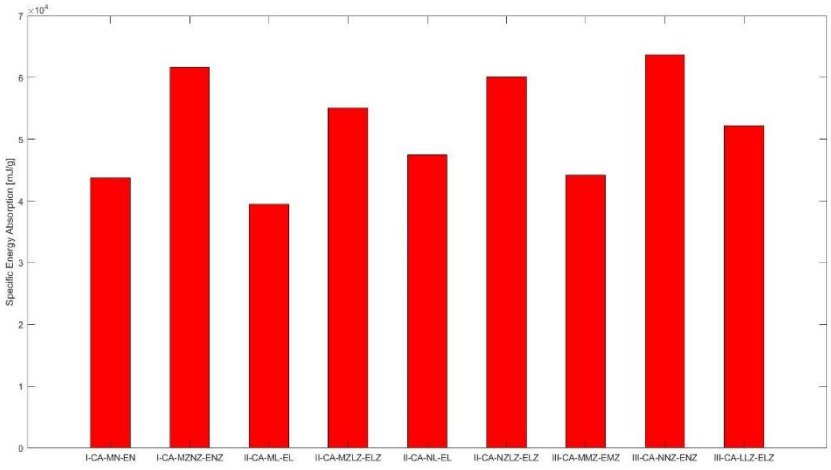

Figure 165: SEA for CA version 2 configurations.

Using results from extra tests performed over all *bcc* and *fcc* sample, a table where percent rise/fall in both mass and EA of every test with respect to the extra ones is shown in table 17.

			Percent mass rise(+) / fall(-) with respect to BCC(M)	Percent mass rise(+) / fall(-) with respect to FCC(N)	Percent EA rise(+) / fall(-) with respect to BCC(M)	Percent EA rise(+) / fall(-) with respect to FCC(N)
			%	%	%	%
GROUP I	MN	I_HA_MN_TM	-9,06	11,06	22,48	-12,77
		I_HA_MN_TN	-9,06	11,06	25,42	-10,67
		I_HD_MN_TM	-9,06	11,06	9,65	-21,91
		I_HD_MN_TN	-9,06	11,06	30,80	-6,84
		I_VA_MN_	-9,06	11,06	24,57	-11,28
		I_CA_MN_EM	-7,25	13,28	21,09	-13,76
		I_CA_MN_EN	-10,87	8,85	26,55	-9,86
	MZNZ	I_HA_MZNZ_TMZ	3,64	26,57	101,68	43,64
		I_HA_MZNZ_TNZ	3,64	26,57	101,19	43,29
		I_HD_MZNZ_TMZ	3,64	26,57	101,44	43,47
		I_HD_MZNZ_TNZ	3,64	26,57	103,12	44,67
		I_VA_MZNZ_	3,64	26,57	102,54	44,26
		I_CA_MZNZ_EMZ	5,52	28,87	100,48	42,78
		I_CA_MZNZ_ENZ	1,76	24,27	103,61	45,02
GROUP II	ML	II_HA_ML_TM	35,92	65,99	59,00	13,25
		II_HA_ML_TL	35,92	65,99	77,14	26,17
		II_HD_ML_TM	35,92	65,99	22,13	-13,02
		II_HD_ML_TL	35,92	65,99	100,93	43,11
		II_VA_ML_	35,92	65,99	69,11	20,44
		II_CA_ML_EM	28,73	57,22	59,04	13,27
		II_CA_ML_EL	43,10	74,77	83,23	30,50
	MZLZ	II_HA_MZLZ_TMZ	48,59	81,47	155,20	81,77
		II_HA_MZLZ_TLZ	48,59	81,47	164,50	88,38
		II_HD_MZLZ_TMZ	48,59	81,47	128,88	63,01
		II_HD_MZLZ_TLZ	48,59	81,47	179,01	98,72

		II_VA_MZLZ_	48,59	81,47	164,36	88,29
		II_CA_MZLZ_EMZ	41,48	72,79	147,59	76,34
		II_CA_MZLZ_ELZ	55,69	90,14	178,20	98,14
	NL	II_HA_NL_TN	26,86	54,93	90,99	36,03
		II_HA_NL_TL	26,86	54,93	98,67	41,50
		II_HD_NL_TN	26,86	54,93	67,07	18,99
		II_HD_NL_TL	26,86	54,93	115,08	53,19
		II_VA_NL_	26,86	54,93	97,17	40,43
		II_CA_NL_EN	17,86	43,94	84,79	31,61
		II_CA_NL_EL	35,85	65,92	109,28	49,06
	NZLZ	II_HA_NZLZ_TNZ	39,17	69,97	169,81	92,17
		II_HA_NZLZ_TLZ	39,17	69,97	176,39	96,86
		II_HD_NZLZ_TNZ	39,17	69,97	147,51	76,28
		II_HD_NZLZ_TLZ	39,17	69,97	192,72	108,48
		II_VA_NZLZ_	39,17	69,97	174,83	95,74
		II_CA_NZLZ_ENZ	30,18	58,99	159,70	84,97
		II_CA_NZLZ_ELZ	48,16	80,95	188,90	105,77
GROUP III	MMZ	III_HA_MMZ_TM	6,53	30,10	42,18	1,26
		III_HA_MMZ_TMZ	6,53	30,10	52,06	8,30
		III_HD_MMZ_TM	6,53	30,10	14,66	-18,34
		III_HD_MMZ_TMZ	6,53	30,10	64,20	16,95
		III_VA_MMZ_	6,53	30,10	46,85	4,59
		III_CA_MMZ_EM	5,22	28,51	40,38	-0,02
		III_CA_MMZ_EMZ	7,83	31,69	54,62	10,12
	NNZ	III_HA_NNZ_TN	-11,95	7,54	72,41	22,79
		III_HA_NNZ_TNZ	-11,95	7,54	75,97	25,33
		III_HD_NNZ_TN	-11,95	7,54	59,08	13,30
		III_HD_NNZ_TNZ	-11,95	7,54	81,97	29,61
		III_VA_NNZ_	-11,95	7,54	76,25	25,53
		III_CA_NNZ_EN	-13,18	6,03	67,52	19,31
		III_CA_NNZ_ENZ	-10,71	9,04	84,34	31,29
	LLZ	III_HA_LLZ_TL	77,98	117,36	189,49	106,19
		III_HA_LLZ_TLZ	77,98	117,36	196,80	111,39
		III_HD_LLZ_TL	77,98	117,36	172,58	94,14
		III_HD_LLZ_TLZ	77,98	117,36	206,60	118,37
		III_VA_LLZ_	77,98	117,36	197,22	111,69
		III_CA_LLZ_EL	76,75	115,86	185,70	103,48
		III_CA_LLZ_ELZ	79,20	118,86	203,59	116,23

Table 17: Percent mass and EA rise (+) / fall (-) with respect to *bcc* and *fcc* sample.

6.2.2 Discussion

Results obtained can be discussed from different points of view: that are groups, combination of cells, configurations, and advantage with respect to classic *bcc* and *fcc* models.

Group I is the one presenting less relevant differences when it comes to find an advantageous configuration: all of them, also reinforced ones, present more or less same EA levels (fig. 149-150).

SEA graphs also move in this direction presenting more or less the same value for all configurations, that is $4*10^4$ mJ/g. A positive aspect of this group can be seen in table 17 though: MN combinations are more convenient than a full *bcc* sample, presenting a smaller mass (-9% circa) and higher EA (maximum +30% for HD configuration). The opposite happens when results are compared to a full *fcc* sample. While, for MZNZ combination the comparison is still good when it is done with *bcc*, having an irrelevant mass rise (+3%) but a valid EA rise (+100% circa). Again, less convenient is the comparison with full *fcc* sample, the compromise EA-mass is not as good as before.

Especially from EA graphs, it is possible to see that Group II starts making evident that some configurations seem to be more adequate for energy absorption: those are HD V2 and CA V2 (where V2 stands for second version). But separate considerations about configurations will be done later. In terms of SEA, best results are obtained by reinforced combinations, that are MZLZ and NZLZ, establishing once again that vertical struts are good for enforcing the relationship between EA and mass. Following table 17 data, trends are different: ML combination presents some advantage with respect to the full *bcc* sample especially for HD V2 configuration (+100% EA), but mass advantage are limited, going from +35% to +43% in mass; again, the confrontation with full *fcc* is not offering promising improvements, with a high mass increase in percent and limited EA rise (if not fall). MZLZ combinations offers extremely good results compared to the *bcc* sample (+180% EA circa for HD and CA V2), while good but bounded are the advantages when it is compared to *fcc*. Far better results are achieved from NL and NZLZ: +115% EA for NL with HD V2 and +190% EA for NZLZ with HD and CA V2. Mass rise is very limited with respect to energy absorption results.

Finally, Group III showed that the best pure energy absorber combination, among the ones meant to be formed by a cell and their reinforced version, is *fbcc + fbccz.* When looking at EA graphs, it is evident how, once again, HD and CA V2 are the best configurations. If instead, SEA diagrams are considered, best results are achieved in general by the NNZ combinations: it has to be stated that trends obtained by SEA analyses resembles the one obtained by static analyses, and not high speed ones, where best SEA is achieved by *bcc* and *bccz*. Motivation for this can be found in the fact that multi-morphology analyses have not been performed until densification, phenomenon that instead gave the possibility to explore *bcc* in a better way. Impressive are as well results that can be seen in table 17: of course, MMZ combination works better than a simple full M sample; slight mass increase makes EA rise more than 50%. Excellent are results of NNZ with respect to M, with mass decreasing (-11%) and EA rising. Not the same can be said with confrontation with N sample, for both this MMZ and NNZ combinations where advantages are limited or even absent. Instead, LLZ configuration

presents advantages in both confrontations: +76% circa in mass but +200% maximum in EA with regards to M sample, less convenient but still good is the comparison with N sample.

Motivation for HD V2 and CA V2 configurations always standing a foot above the others is different: It can be noted in fact that also HA V2 is always higher than HA V1. That is because cells with higher strength and stiffness are always on the top layer in HA/HD V2 (that happens in different natural lattices, where stronger layers are always the external ones). This is linked with the fact that only 30% crashing is performed, therefore bottom layers are not as important as top ones in these cases. A deeper investigation could be possible using a better homogenization method or using full topology, where densification could change initial results (as for static and dynamic results). CA V2 instead gained better results both thanks to the configuration itself (also CA V1 obtained notable results as well) and because CA V2 always presents a slightly higher percent volume of stronger cells. Results achieved in this sense are still good for non-complete crashing phenomenon and as benchmarking analyses.

7 Conclusions

It must be remembered that, as said in the introduction, the aim of this investigation is the definition of guidelines for designs making use of lattices selected and the establishment of a methodology for lattices analysis: therefore, results achieved are not affected from a main driver, since there are many points of view these need to be seen from. Also, different cells have been analyzed, therefore each one of these present different advantages and disadvantages.

First, a summary of main results obtained up to now is presented. In chapter 3, static analyses have been performed, and by looking at results it can be said that there are no differences in EA, SEA and force reaction trends between linear and bilinear models. This is a proof that linear model is also able to perform interesting results, at least for starting and benchmarking analyses where there are no large displacements and excessive overtaking of the yield point. Advantages that vertical reinforcement offers is already quite evident. By the way, *fbccz* and *fccz* obtained best EA (*bccz* true potential has been discovered only in the next chapter), while *fcc*/*fccz* present best SEA, because of their low mass. Force reaction at first was considered as the counterpart of peak stress for dynamic simulations: it ended up being the one of plateau stress that is actually comparable to EA itself.

Chapter 4 dealt with high speed crashing simulations, though it does not consider strain rate effects. First of all, this section shows there are different ways of modeling a RVE depending on the circumstances: here buckling, and in general cell behavior, is better respected using another version of the RVE rather than the classical one. What these tests unveiled was the true effectiveness of *bcc* and *bccz* in both EA and SEA; this is due to the fact that these cells perform a higher densification strain, resulting into an additional section in the stress-strain diagram devolved to energy absorption. Also, *bccz* together with *fccz* achieved good CLE thanks to their high plateau stress (that, as said, it is related to the force reaction from static analyses) and low peak stress. Once again, vertical reinforcement results as a very good improvement from all points of view.

The homogenization method developed in chapter 5 obtained good results in the strain field that is limited to 30% crashing because of the excessive errors evaluated beyond that threshold. Main advantage of this method, besides being simple and effective, is the time that has been saved when it has been used for multi-morphology design in chapter 6: these analyses, if performed modeling the whole topology of the cells, would have taken days, if not weeks. Instead, they lasted about 2 minutes and gave back valid results. HD V2 and CA V2 has been selected as best candidate for energy absorption application, being the best option for both EA and SEA. These results need of course to be validated for higher strains. Also, though *fbccz* did not perform best results (exception made for

pure energy absorption in static analyses), this cell is very effective when it comes to combinations: best ones were in fact LLZ (*fbcc* + *fbccz*), NZLZ (*fccz* + *fbccz*) and MZLZ (*bccz* + *fbccz*), those obtained best results when compared to classic lattices (*bcc* and *fcc*).

General guidelines about the cells that have been analyzed can be stated. First, vertical reinforcement is always efficacious: this basically depends on the fact that a slightly addition to the mass is always paid back with energy absorption improvements and these effects are always evident when looking at SEA. Cells work in different ways: *bccz* is extremely good for total crashing, because of its high densification point. A high CLE is also performed, showing a stable and efficient crushing process, with a low peak resulting into less problems from the inertial reaction of the structure these lattices will be part of. Instead, *fbccz*, though not performing best SEA, is the lightest reinforced cell that has been analyzed. From bilinear static simulations resulted to be the best choice and in fact it presents a stiffer linear region than *bccz*. Therefore, this cell can be employed for non-total crashing phenomenon, and it gained the highest CLE resulting as the cell performing the most efficient load path when it comes to crashing as well. Finally, *fbccz* performs high EA, though SEA is limited because of its mass. Best results are achieved from this cell when it comes to be combined with others: low mass of other cells combined with the excellent performances of *fbccz* result in fact into good SEA.

Besides results achieved from the point of view of mere performances, this thesis also wants to be a contribution in the direction of defining a methodology for lattices analyses, at least from the numerical simulations viewpoint. The way this investigation has been carried out resulted into a quite accurate description of the selected lattices behavior, obviously directed in the energy absorption properties, that are the main topic; a parallel path can be followed in the case investigated properties are different. First, static analyses, though missing some important aspects of the cells behavior and characteristics, have been extremely important in giving a specific direction to the research, being useful as benchmarking analysis and for starting results. Apart from being able to catch cell properties at a prototypal level, these simulations are also extremely fast and practical in order to become acquainted with topologies (that in the world of lattices can be extremely complex). Next step is in direct contact with the topic of impact and crashworthiness: high speed crashing simulations gave the possibility to get deeper into the topic, offering results statics could not process: new (and better) properties have been unveiled. A homogenization method has also been employed and that has been necessary because, for bigger samples or components, computational power required might be excessive (depending in the processor used of course). Once properties of single lattices employed are obtained, they can be used to develop many different designs: the one chosen for this investigation

is the multi-morphology one, but many others can be found in literature, including of course components.

This thesis stops at improvements on energy absorption investigating different cell topologies and combinations of them, but steps forwards can of course be made: first of all, these results can be validated via experimentation for manufactured samples, but also the topic can be extended to different cell sizes, aspect ratios (of both struts and RVE) as well to different topologies. Multi-morphology design has been here introduced, but the development and design of components can of course enforce the results presented.

Bibliography

[1] Gibson L.J., Ashby M.F., Cellular Solids: Structure and Properties – Second Edition, Cambridge University Press (1997).
[2] Ashby M.F., The Mechanical Properties of Cellular solids, The 1983 Institute of Metals Lecture, The Metallurgical Society of AIME.
[3] Ha N.S., Lu G., A review of recent research on bio-inspired structures and materials for energy absorption applications, Composites Part B 181 (2020).
[4] Seharing A., Azman A.H., Abdullah S., A review on integration of lightweight gradient lattice structures in additive manufacturing parts, Advances in Mechanical Engineering 12 (2020).
[5] Yang X., Sun Y., Yang J., Pan Q., Out-of-plane crashworthiness analysis of bio-inspired aluminum honeycomb patterned with horseshoe mesostructured, Thin-Walled Structures 125 (2018).
[6] Sun G., Jiang H., Fang J., Li G., Li Q., Crashworthiness of vertex based hierarchical honeycombs in out-of-plane impact, Materials and Design 110 (2016).
[7] He Q., Feng J., Chen Y., Zhou H., Mechanical properties of spider-web hierarchical honeycombs subjected to out-of-plane impact loading, Journal of Sandwich Structures & Materials 0 (2018).
[8] Wen Z., Sha Y., Yu T.X., Jun X., Crushing resistance and energy absorption of pomelo peel inspired hierarchical honeycomb, International Journal of Impact Engineering 125 (2019).
[9] An X., Fan H., Hybrid design and energy absorption of luffa-sponge-like hierarchical cellular structures, Materials and Design 106 (2016).
[10] Li W., Xu K., Li H., Jia H., Liu X., Xie J., Energy Absorption and Deformation Mechanism of Lotus-type Porous Coppers in Perpendicular Direction, Journal of Materials Science & Technology 33 (2017).
[11] Olsson A., Naarttijärvi M., Design optimization for 3D printed energy absorbing structures inspired by nature, Master's thesis in Material and Computational Mechanics, Chalmers University of Technology (2017).
[12] du Plessis A., Broeckhoven C., Yadroitsev I., Yadroitsava I., le Roux S.G., Analyzing nature's protective design: The glyptodont body armor, Journal of the Mechanical Behavior of Biomedical Materials 82 (2018).
[13] Wang H., Gu D., Lin K., Xi L., Yuan L., Compressive Properties of Bio-Inspired Reticulated Shell Structures Processed by Selective Laser Melting, Advanced Engineering Materials 21 (2019).
[14] Han S.C., Kang D.S., Kang K., Two nature-mimicking auxetic materials with potential for high energy absorption, Materials Today 26 (2019).
[15] Souza J., Großmann A., Mittelstedt C., Micromechanical analysis of the effective properties of lattice structures in additive manufacturing, Additive Manufacturing 23 (2018).
[16] De Pasquale G., Luceri F., Riccio M., Experimental evaluation of selective laser melting process for optimized lattice structures, Journal of Process Mechanical Engineering 0 (2018).
[17] De Pasquale G., Luceri F., Riccio M., Experimental Characterization of SLM and EBM Cubic Lattice Structures for Lightweight Applications, Experimental Mechanics 59 (2019).
[18] De Pasquale G., Luceri F., Experimental validation of Ti6Al4V bio-inspired cellular structures from additive manufacturing processes, Materials Today: Proceedings 7 (2019).

[19] De Pasquale G., Sibona S., Hybrid materials based on polymers-filled AM steel lattices with energy absorption capabilities, Mechanics of Advanced Materials and Structures (2021).
[20] Ki Moon S., Tan Y.E., Hwang J., Yoon Y.J., Application of 3D Printing Technology for Designing Light-weight Unmanned Aerial Vehicle Wing Structures, International Journal of Precision Engineering and Manufacturing-Green Technology 1 (2014).
[21] De Pasquale G., Tagliaferri A., Modeling and characterization of mechanical and energetic elastoplastic behavior of lattice structures for aircrafts anti-icing systems, Journal of Mechanical Engineering Science (2019).
[22] Yin S., Chen H., Wu Y., Li Y., Xu J., Introducing composite lattice core sandwich structure as an alternative proposal for engine hood, Composite Structures 201 (2018).
[23] De Pasquale G., Bertuccio E., Catapano A., Montemurro M., Modeling of cellular structures under static and fatigue loads, II International Conference on Simulation for Additive Manufacturing - Sim-AM (2019).
[24] Maloney K.J., Fink K.D., Schaedler T.A., Kolodziejska J.A., Jacobsen A.J., Roper C.S., Multifunctional heat exchangers derived from three-dimensional micro-lattice structures, International Journal of Heat and Mass Transfer 55 (2012).
[25] Wang Y., Arabnejad S., Tanzer M., Pasini D., Hip Implant Design With Three-Dimensional Porous Architecture of Optimized Graded Density, Journal of Mechanical Design 140 (2018).
[26] Leary M., Mazur M., Williams H., Yang E., Alghamdi A., Lozanovski B., Zhang X., Shidid D., Farahbod-Sternahl L., Witt G., Kelbassa I., Choong P., Quian M., Brandt M., Inconel 625 lattice structures manufactured by selective laser melting (SLM): Mechanical properties, deformation and failure modes, Materials and Design 157 (2018).
[27] Smith M., Guan Z., Cantwell W.J., Finite element modelling of the compressive response of lattice structures manufactured using the selective laser melting technique, International Journal of Mechanical Sciences 67 (2013).
[28] McKown S., Shen Y., Brookes W.K., Sutcliffe C.J., Cantwell W.J., Langdon G.S., Nurick G.N., Theobald M.D., The quasi-static and blast loading response of lattice structures, International Journal of Impact Engineering 35 (2008).
[29] Ullah I., Brandt M., Feih S., Failure and energy absorption characteristics of advanced 3D truss core structures, Materials and Design 92 (2016).
[30] Al-Saedi D.S.J., Masood S.H., Faizan-Ur-Rab M., Alomarah A., Ponnusamy P., Mechanical properties and energy absorption capability of functionally graded F2BCC lattice fabricated by SLM, Materials and Design 144 (2018).
[31] Fila T., Zlamal P., Jirousek O., Falta J., Koudelka P., Kytyr D., Doktor T., Valach J., Impact Testing of Polymer-filled Auxetics Using Split Hopkinson Pressure Bar, Advanced Engineering Materials 10 (2017).
[32] Ozdemir Z., Tyas A., Goodall R., Askes H., Energy absorption in lattice structures in dynamics: Nonlinear FE simulations, International Journal of Impact Engineering 102 (2017).
[33] Naiafi M., Ahmadi H., Liaghat G., Experimental investigation on energy absorption of auxetic structures, Materials Today: Proceedings 34 (2021).
[34] Cao X., Duan S., Liang J., Wen W., Fang D., Mechanical properties of an improved 3D-printed rhombic dodecahedron stainless steel lattice structure of variable cross section, International Journal of Mechanical Sciences 145 (2018).

[35] Xiao L., Song W., Wang C., Liu H., Tang H., Wang J., Mechanical behaviour of open-cell rhombic dodecahedron Ti–6Al–4V lattice structure, Materials Science & Engineering A 640 (2015).
[36] Cao X., Xiao D., Li Y., Wen W., Zhao T., Chen Z., Jiang Y., Fang D., Dynamic compressive behaviour of a modified additively manufactured rhombic dodecahedron 316L stainless steel lattice structure, Thin–Walled Structures 148 (2020).
[37] Aboulkhair N.T., Maskery I., Tuck C., Ashcroft I., Everitt N.M., The microstructure and mechanical properties of selectively laser melted AlSi10Mg: The effect of a conventional T6-like heat treatment, Materials Science & Engineering A 667 (2016).
[38] Zhuo L., Wang Z., Zhang H., Yin E., Wang Y., Xu T., Li C., Effect of post-process heat treatment on microstructure and properties of selective laser melted AlSi10Mg alloy, Materials Letters 234 (2019).
[39] Martin J.H., Yahata B.D., Hundley J.M., Mayer J.A., Schaedler T.A., Pollock T.M., 3D printing of high-strength aluminium alloys, Springer Nature 549 (2017).
[40] Uzan N.E., Shneck R., Yeheskel O., Frage N., High-temperature mechanical properties of AlSi10Mg specimens fabricated by additive manufacturing using selective laser melting technologies (AM-SLM), Additive Manufacturing 24 (2018).
[41] Kempen K., Thijs L., Van Humbeeck J., Kruth J.P., Mechanical properties of AlSi10Mg produced by Selective Laser Melting, Physics Procedia 39 (2012).
[42] Cao Y., Lin X., Wang Q.Z., Shi S.Q., Ma L., Kang N., Huang W.D., Microstructure evolution and mechanical properties at high temperature of selective laser melted AlSi10Mg, Journal of Materials Science & Technology 62 (2021).
[43] matweb site:
http://www.matweb.com/search/DataSheet.aspx?MatGUID=4501b3b8259e4767ad9248ed98e70fb6&ckck=1
[44] Xing X., Duan X., Sun X., Gong H., Wang L., Jiang F., Modification of Residual Stresses in Laser Additive Manufactured AlSi10Mg Specimens Using an Ultrasonic Peening Technique, Materials 12 (2019).
[45] Bai L., Gong C., Chen X., Sun Y., Xin L., Pu L., Peng Y., Luo J., Mechanical properties and energy absorption capabilities of functionally graded lattice structures: Experiments and simulations, International Journal of Mechanical Sciences 182 (2020).
[46] Baykasoglu A., Baykasoglu C., Cetin E., Multi-objective crashworthiness optimization of lattice structure filled thin-walled tubes, Thin–Walled Structures 149 (2020).
[47] Lei H., Li C., Meng J., Zhou H., Liu Y., Zhang X., Wang P., Fang D., Evaluation of compressive properties of SLM-fabricated multi-layer lattice structures by experimental test and μ-CT-based finite element analysis, Materials and Design 169 (2019).
[48] Li Q.M., Magkiriadis I., Harrigan J.J., Compressive Strain at the Onset of Densification of Cellular Solids, Journal of Cellular Plastics 42 (2006).
[49] E.J. Barbero, Finite Element Analysis of Composite Material using Ansys - Second Edition, CRC press – Taylor & Francis Group (2014).
[50] Alberdi R., Dingreville R., Robbins J., Walsh T., White B.C., Jared B., Boyce B.L., Multi-morphology lattices lead to improved plastic energy absorption, Materials and Design 194 (2020).
[51] Bertolino G., Montemurro M., De Pasquale G., Multi-scale shape optimisation of lattice structures: an evolutionary-based approach, Journal on Interactive Design and Manufacturing (2019).

[52] Nakshatrala P.B., Tortorelli D.A., Nakshatrala K.B., Nonlinear structural design using multiscale topology optimization, Part I: Static formulation, Comput. Methods Appl. Mech. Engrg. 261–262 (2013).
[53] Cheng L., Bai J., To A.C., Functionally graded lattice structure topology optimization for the design of additive manufactured components with stress constraints, Computer Methods in Applied Mechanics and Engineering 344 (2019).
[54] Panesar A., Abdi M., Hickman D., Ashcroft I., Strategies for functionally graded lattice structures derived using topology optimization for Additive Manufacturing, Additive Manufacturing 19 (2018).
[55] Wang Y., Zhang L., Daynes S., Zhang H., Feih S., Wang M.Y., Design of graded lattice structure with optimized mesostructures for additive manufacturing, Materials and Design 142 (2018).
[56] Lei H., Li C., Zhang X., Wang P., Zhou H., Zhao Z., Fang D., Deformation behavior of heterogeneous multi-morphology lattice core hybrid structures, Additive Manufacturing 37 (2021).